Journal of Healthcare Engineering

Unobtrusive Sensing Technologies for the Lifecare Solution

Lead Guest Editor: Hyun J. Baek
Guest Editors: Ahyoung Choi, Jilong Kuang, and Heenam Yoon

Unobtrusive Sensing Technologies for the Lifecare Solution

Journal of Healthcare Engineering

Unobtrusive Sensing Technologies for the Lifecare Solution

Lead Guest Editor: Hyun J. Baek
Guest Editors: Ahyoung Choi, Jilong Kuang, and Heenam Yoon

Contents

Hindawi
Journal of Healthcare Engineering
Volume 2019, Article ID 7597190, 2 pages
https://doi.org/10.1155/2019/7597190

Editorial

Unobtrusive Sensing Technologies for the Lifecare Solution

Hyun Jae Baek[1] **Ahyoung Choi,**[2] **Jilong Kuang,**[3] **and Heenam Yoon**[4]

[1] *Department of Medical and Mechatronics Engineering, Soonchunhyang University, Asan, Republic of Korea*
[2] *Department of Software, Gachon University, Seongnam, Republic of Korea*
[3] *Samsung Research America (SRA), Mountain View, CA, USA*
[4] *Artificial Intelligence Laboratory, Software Center, LG Electronics, Seoul, Republic of Korea*

Correspondence should be addressed to Hyun Jae Baek; hjbaek@sch.ac.kr

Received 20 June 2019; Accepted 24 June 2019; Published 9 July 2019

The paradigm for healthcare is not only transforming from hospital-oriented treatments to individually centered prevention but also extending its scope from disease-oriented to wellness-centered. One of the key requirements for care of entire life is to detect health and wellness status accurately and sustainably in various life scenarios [1].

A variety of technologies are currently used to track a person's health and wellness status. They include electrodes, optical sensors, strain gauges, ultrasound devices, etc., each of which has some drawbacks in terms of user experiences such as comfort and convenience or its performance, more specifically, accuracy. The objective of emerging unobtrusive sensing technology is to enable sustainable tracking of physical activities and behaviors, as well as physiological and biochemical parameters during daily life, while ensuring accuracy. This may also include estimating health-related indexes that are difficult to measure unobtrusively by using a combination of various physiological signals measured in a noninvasive and unobtrusive manner.

The person being monitored would not even notice the existence of the sensing device or procedure [2]. Unobtrusive sensing technologies, which can be implemented in the form of wearables and IoT devices, may be a good solution for the future lifecare, but there is a difficulty in deriving useful information from low-quality signals [3, 4].

The goal of this special issue is to share cutting-edge research and applications on unobtrusive sensing solutions such as sensors, devices, and signal processing algorithms. For this, the editorial team focused on the core technologies that could contribute to the implementation of possible future unobtrusive lifecare devices and identified the seven representative manuscripts submitted to the special issue.

This special issue includes 1 review paper and 6 research papers on state-of-the-art health sensing technologies that are being studied and developed for lifecare. In the review article entitled "Current Status and Prospects of Health-Related Sensing Technology in Wearable Devices," J. Cho investigated the healthcare-sensing functions of current commercially available wrist-wearable devices and their technological limitations and prospects. In the article entitled "Noise-Robust Heart Rate Estimation Algorithm from Photoplethysmography Signal with Low Computational Complexity," J. Shin and J. Cho applied noise robust oscillator-based adaptive notch filter algorithm to trace the heart rate frequency in low signal-to-noise ratio PPG signal. In the article entitled "Quantitative Assessment of Autonomic Regulation of the Cardiac System," J. K. Wu et al. described a systematic method for the quantitative assessment of autonomic cardiac system regulation based on homeostasis and probabilistic graphic model using physiological parameters. In the article entitled "An Efficient Deep Learning Approach to Pneumonia Classification in Healthcare," O. Stephen et al. proposed a convolutional neural network model to extract features from a given chest X-ray image and classify it to determine the presence of pneumonia. In the article entitled "Using Kinect v2 to Control a Laser Visual Cue System to Improve the Mobility during Freezing of Gait in Parkinson's Disease," A. Amini et al. proposed a new indoor method for casting dynamic and automatic visual cue for improving mobility of people with Parkinson's disease based on skeletal information acquired in real time from a Kinect v2. In the article entitled "Estimation of Breathing Rate with Confidence Interval Using Single-Channel CW Radar," I. Nejadgholi et al. proposed an algorithm for breathing rate estimation from single-channel continuous wave radar using time-frequency analysis to extract Doppler frequency of the radar signal over time. In the article entitled "Development of a Wireless Health Monitoring System for Measuring Core Body Temperature from the Back of the Body," Q. Wei et al. explored a wireless semiconductor sensor to measure core body temperature at the skin surface of the back under the neck.

Conflicts of Interest

The editors declare that there are no conflicts of interest regarding the publication of this issue.

Hyun Jae Baek
Ahyoung Choi
Jilong Kuang
Heenam Yoon

References

[1] M. Flores, G. Glusman, K. Brogaard, N. D. Price, and L. Hood, "P4 medicine: how systems medicine will transform the healthcare sector and society," *Personalized Medicine*, vol. 10, no. 6, pp. 565–576, 2013.

[2] Y. G. Lim, K. H. Hong, K. K. Kim et al., "Monitoring physiological signals using nonintrusive sensors installed in daily life equipment," *Biomedical Engineering Letters*, vol. 1, no. 1, pp. 11–20, 2011.

[3] H. J. Baek, G. S. Chung, K. K. Kim, and K. S. Park, "A smart health monitoring chair for nonintrusive measurement of biological signals," *IEEE Transactions on Information Technology in Biomedicine*, vol. 16, no. 1, pp. 150–158, 2011.

[4] U. Satija, B. Ramkumar, and M. S. Manikandan, "Real-time signal quality-aware ECG telemetry system for IoT-based health care monitoring," *IEEE Internet of Things Journal*, vol. 4, no. 3, pp. 815–823, 2017.

Hindawi
Journal of Healthcare Engineering
Volume 2019, Article ID 3924508, 8 pages
https://doi.org/10.1155/2019/3924508

Review Article

Current Status and Prospects of Health-Related Sensing Technology in Wearable Devices

Jaegeol Cho

Department of Medical and Mechatronics Engineering, Soonchunhyang University, Asan, Chungnam 31538, Republic of Korea

Correspondence should be addressed to Jaegeol Cho; jaegeolcho@sch.ac.kr

Received 15 February 2019; Revised 22 May 2019; Accepted 29 May 2019; Published 16 June 2019

Guest Editor: Jilong Kuang

The healthcare-related functions of wearable devices are very useful for continuous monitoring of biological information. Wearable devices equipped with communication function can be used for additional healthcare services. Among the wearable devices, the wristband type is most suitable for acquiring biological signals, and the wear preference of the user is high, so it is highly likely to be used more in the future. In this paper, the health-related functions of wristband were investigated and the technical limitations and prospects were also reviewed. Most current wristband-type devices are equipped with the combination of accelerometer, optical sensor, and electrodes for their health functions, and continuously measured data are expanding the possibility of discovering new medical meanings. The blood pressure measurement function without using cuff is the most useful and expected function among the health-related functions expected to be mounted on the wrist wearable device, in spite of its technical limits and difficulties.

1. Introduction

It is a common human desire to live long and healthy regardless of age or area. Recently, as the development of genetic analysis technology has enabled us to recognize and prevent the risk of genetic diseases in advance, this hope has become more realistic. With the development of continuous medical technology and new drug development, diseases that were previously regarded as incurable diseases can now be seen as chronic diseases that can be managed through continuous management. In addition, as the ongoing research and achievement of stem cell technology continues, there is growing hope that human tissue can be regenerated, and thus the possibility of extending the life span of human beings, which is considered to be about the limit of around 100 years, is getting stronger.

So, if we cope with these diseases properly, can anyone live long and healthy? The answer should be considered in two respects. If the best unlimited healthcare services are offered to an individual, the chances of a long and healthy life are high, but considering the high costs involved, it is difficult to imagine that the social medical system will be established where the best medical services are provided to every individual. In other words, if it is not possible to provide unlimited medical services to all members of society, it is imperative to have a sustainable healthcare system that will keep the population as healthy as possible at a minimum cost, in parallel with the development of effective medical technology for treating the disease. Especially as aging has accelerated, the increase in the number of chronic illnesses and consequent increase in the cost of disease management, the increase in waiting time due to lack of medical personnel, and the decrease in actual hours of treatment further strengthen the demand for a new medical system.

In this respect, according to a previous study [1], health is influenced by genetic causes, social environment, environmental factors, behavioral patterns, and medical care. Among these five factors, the most common cause of premature death (death except natural causes caused by aging) is wrong behavioral patterns, accounting for 40% of the total, and medical care contributes only 10%. Therefore, in terms of population health, even if a large amount of money is provided to provide the best medical service, the effect of improvement is considerably weak, and it is the most effective prescription for the members of society to maintain a clean environment with healthy lifestyle.

Environmental factors can be controlled and quantitatively measured and monitored by national and governmental regulations and efforts; however, the individual's lifestyle and behavior will need to be reviewed to determine what to measure and monitor. In order to measure health-related habits in daily life rather than patients in a hospital, a wearable device capable of measuring a biosignal attached to an individual's body is required. Recently, wrist-type smart devices have been widely used, and the healthcare-related technologies that utilize them are increasing. Therefore, not only wellness services that help individuals to manage their own health but also services for remotely managing chronic diseases using measured data are being tried by governments and insurance companies. An example is the use of a wristband to monitor exercise and heart rate after coaching appropriate levels of exercise in patients treated with heart failure, thereby preventing readmission and reducing medical costs accordingly.

In this review, healthcare-related technologies applied to personal wearable devices have been examined which are widely used in recent years, and the sensing technology and related technical issues required for health management in the future are discussed.

2. Methods

In this review, health-related functions included in wearable devices are surveyed and summarized. Technical problems related to the cuffless blood pressure measurement function which is not mounted on wrist wearable devices up to now are discussed.

First, the functions of patient monitoring system in hospitals and biosignal measurement items that can be measured in daily life were compared to predict the technology status and development direction of wearable devices. It was also examined that which of the various wearable devices are suitable for biosignal measurement, and the measurable functions were listed accordingly. The biomedical measurement items using sensors included in a wristband, which is a typical wearable device, are summarized.

Secondly, an overview diagram of blood pressure measurement methods has been made to review the possibility and current status of cuffless blood pressure measurement techniques, and the technical limitations of the pulse wave velocity (PWV) method, which has been widely tried, were investigated.

3. Discussion

3.1. Healthcare Sensing Technology Applied to Wearable Devices. The current development of medical devices shows that it is a big trend to monitor and monitor at any time in home and everyday life, not in a specific place of hospital. In accordance with this trend, medical technology is moving from the field of doctors and specialists to the general public, from the hospital to the home, and also to the mobile environment, and wearable devices and related services will play an increasingly important role. For example, biomedical measurements such as electrocardiograms and oxygen saturation that have been measured using equipment in hospitals can now be easily measured by wearable devices that are small and inexpensive. As a result, new healthcare services using the measurement data can also be introduced. In Figure 1, a typical screen of patient monitoring system used in hospital is shown and its measurement functions are listed up. Recording and analysis of ECG signals and measurements of heart rate, SpO_2, respiration rate, and body temperature are now all possible with small-size handheld devices or wearable devices as shown in the figure. However, the miniaturization of blood pressure measurement function is still ongoing, which will be discussed later.

In addition to technological advances, expectations and requirements of consumers who purchase and use wearable devices are also meeting new remote healthcare services. According to a recent report [2], the widespread use of wearable devices is expected to prolong consumers' life span, lower healthcare costs, and reduce obesity issues, and these trends are becoming clearer over time. There are various types of wearable devices currently available, such as wristband-type devices [3–6], glasses [7], shoes [8], patches [9–12], socks [13], clothes [14], earphones [15–17], rings [18], and clips [3]; however, the most suitable form to measure various biosignals and to manage health through it is thought to be the wrist-type device. As shown in Figure 2, the location where the electrocardiogram, photoplethysmography, and electrodermal activity can be easily measured is the wrist, and the experience of wearing a wristwatch is expected to eliminate the feeling of wearing a wearable wristband device. This can be seen in a previous survey [19] of the most preferred locations for wearing wearable devices on the body. The most preferred location was the wrist (65%), and most of the positions replacing the worn accessories such as glasses (55%) and armband (40%) were highly preferred.

From Fitbit's product portfolio (Figure 3), which is one of the representative companies developing and selling wearable devices, it can be seen that there are various functions by product type and price. In addition, the higher the price, the more various the healthcare-sensing functions included, and the wrist-type device has the most various functions among the company's other products. Representative sensors and related functions applied to wrist wearable devices of major companies such as Fitbit, Apple, Garmin, and Samsung can be roughly classified into three categories as Table 1.

The wristband-type devices currently available are almost all combinations of the above three sensors and functions. In particular, in the case of the optical sensor for measuring the heart rate [20–29], the function of measuring the pulse continuously for 24 hours is spreading using low power architecture, like the case of the accelerometer which is used to measure the movement of the user at all times for 24 hours at very low power. These always-on functions extend the possibility of discovering new medical meanings because the user's biosignals can be continuously measured over several days.

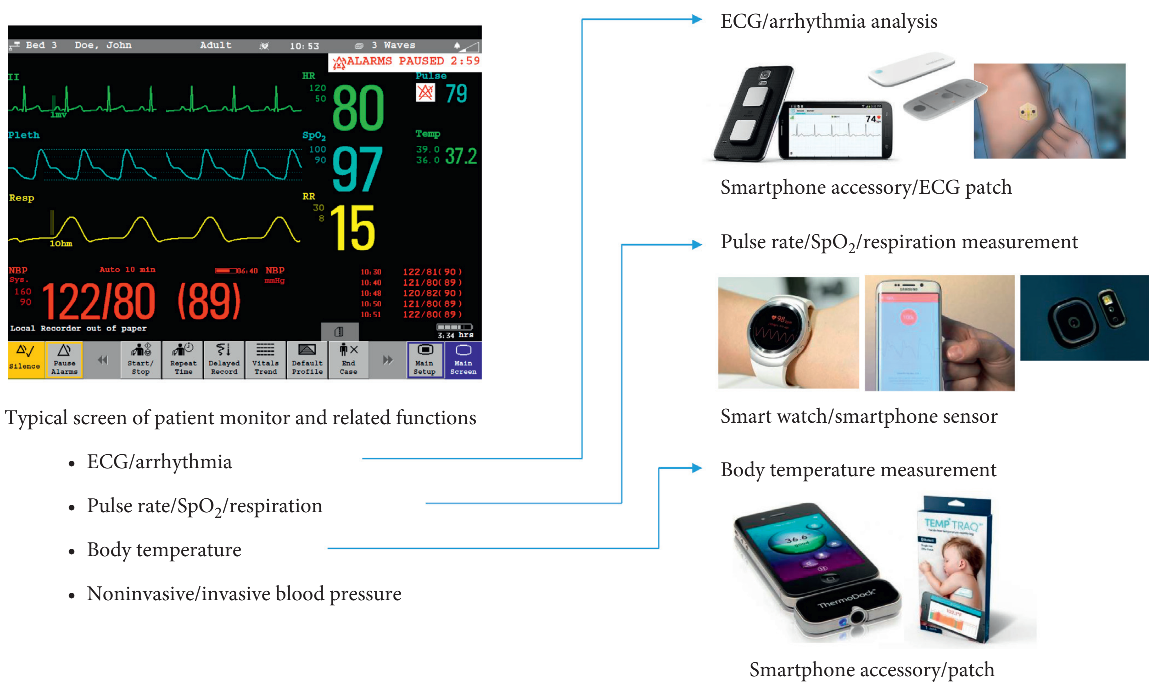

FIGURE 1: Evolution of patient monitoring system for wearable devices and daily life.

Bio-signal	Wristwear	Clothing	Eyewear	Earwear	Ring	Patch
Electrocardiography	√	√	√			√
Photoplethysmography	√	√	√	√	√	√
Electrodermal activity	√	√			√	
Body impedance	√	√				
Electrooculography			√			
Electromyography	√	√				
Electroencephalography			√	√		
Acceleration	√	√	√	√	√	√
Illuminance	√	√	√	√	√	

FIGURE 2: Comparison of biosignal measurement items according to wearable device type and wearing position.

3.2. Wearable Blood Pressure Sensing Technology Outlook. Blood pressure is one of the fundamental and important vital signs (pulse, blood pressure, body temperature, respiration) and is closely related to arterial health, which is considered to be an important indicator of health. Therefore, blood pressure is a kind of health indicator that needs to be managed with great importance. In particular, in the case of hypertension, the blood pressure trend for 24 hours is more important than the blood pressure value measured from time to time. Therefore, it is necessary to continuously monitor and manage it. Because hypertension is the most common cause of death among developed and developing countries [30], the need for blood pressure management using wearable devices has long been emphasized, and among the health-related functions, it is expected to be the most useful and expected function to be mounted on the wrist wearable device in the future.

The methods of blood pressure measurement are classified and summarized in Figure 4. The technologies which have not been clinically proved enough are surrounded with dashed lines. The auscultatory method using a brachial cuff and a stethoscope has been considered as a gold standard of blood pressure measurement [31]; however, the oscillometric blood pressure monitor using cuff is the most widely used method due to convenience and proven accuracy [32]. Since the oscillometric blood pressure monitor uses an upper arm or wrist cuff, it is not suitable for measuring blood pressure from time to time during daily life; nonocclusive

	Ace	Alta	Alta HR	Charge 3	Versa	Ionic
Steps and activity	√	√	√	√	√	√
Calories burned		√	√	√	√	√
Floors climbed				√	√	√
Sleep tracking	√	√	√	√	√	√
Sleep stages (light/deep/REM)			√	√	√	√
Auto exercise recognition		√	√	√	√	√
Hourly activity	√	√	√	√	√	√
Swim tracking				√	√	√
24/7 heart rate monitoring			√	√	√	√
Cardio fitness level			√	√	√	√

Figure 3: Fitbit's wearable device types and functions (Feb. 2019).

Table 1: Sensors and their health-related functions in wearable devices.

Sensor	Functions
Accelerometer	Step count/calories/pace and distance/active time Sleep efficiency/sleep time/sleep stages (light, deep, REM) Exercise recognition (walking, running, rowing, swimming, etc.)
Optical sensor	Heart rate (at rest, during exercise) from photoplethysmogram (PPG) 24 h continuous heart rate Respiration Oxygen saturation (SpO_2) Heart rate variability (HRV) Light intensity (illuminance)
Electrodes	Electrocardiogram (ECG) Bioimpedance analysis (body fat, muscle, etc.) Heart rate (impedance plethysmography) Perspiration

techniques which do not occlude the arteries to measure blood pressure are generally considered as the candidates of blood pressure measurement technology for wearable devices. To make blood pressure measurement easy and convenient, Omron Healthcare (Japan) has recently developed a wrist monitor called "HeartGuide," an oscillometric blood pressure monitor with a relatively small wrist cuff [33]. Although it is necessary to press the finger manually to apply the oscillometric principle, recent studies have shown potential to use smartphones as blood pressure monitors [34, 35]. Among the nonocclusive techniques, tonometry [36–38], pulse wave velocity (PWV) [39–50], and photoplethysmography (PPG) [51, 52] have been extensively studied and developed for ambulatory blood pressure monitoring (ABPM).

Figure 5 shows representative blood pressure measurement devices that do not use a cuff. The T-Line system (Tensys Medical Inc., USA), Finometer (Finapres Medical Systems, Netherlands), and the Vasotrac (Medwave, USA) are typical devices which have been used for noninvasive arterial line monitoring in hospitals. In the T-Line system using radial artery applanation tonometry, the contact pressure between the radial artery and the bone should be optimized and continuously adjusted automatically, and its clinical accuracy has been tested under various conditions [53–55]. The Finometer measures the arterial pressure waveform at the finger using volume-clamp method, also known as the Finapres (FINger Arterial PRESsure) method. The volume of finger artery is measured with optical sensors and is automatically maintained constant with the finger cuff connected to pneumatic control system. The volume-clamp method showed good agreements with intra-arterial monitoring [56] and auscultatory method [57]; however, when measuring blood pressure waveforms under abnormal conditions such as finger oedema or insufficient blood perfusion, the volume-clamp method is inaccurate or even impossible [58, 59]. The Vasotrac device measures the radial blood pressure using pressure sensing module located over the radial artery with a length-adjustable wrist strap. The wrist strap automatically repeats compression and release to record the radial blood pressure waveform and estimate the blood pressure every 12~15 pulse beats using proprietary algorithms. Previous studies showed that the accuracy of Vasotrac is controversial [60, 61].

There also have been numerous attempts to develop ABPM devices; however, personal blood pressure monitors without cuffs have not yet been proven to be accurate. Although the BPro device (Healthstats, Singapore) showed good accuracy in previous studies [36–38], the tonometry method is highly sensitive to motion and needs precise positioning of the sensor, which makes it difficult to be commonly used in daily life [62]. As is shown in the figure, all the previous studies and products without using cuffs have attempted to measure blood pressure in the wrist or finger for a variety of reasons, such as the location of the artery, easiness for ECG measurement, and so on.

The most popular method among the various methods shown in Figure 5 is the method using pulse wave velocity

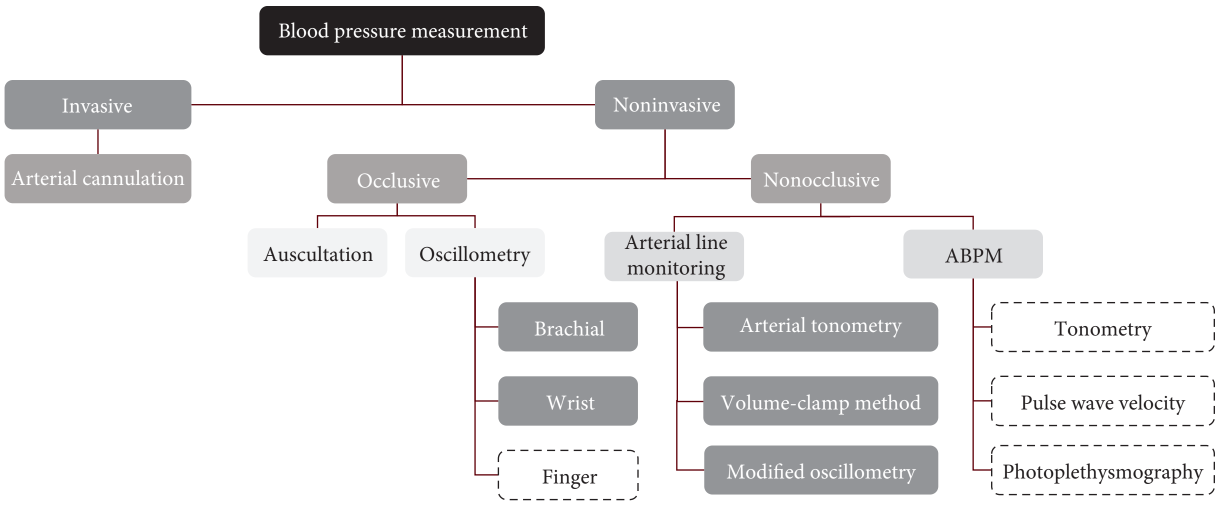

Figure 4: Blood pressure measurement technology classification (the technology in boxes with dashed lines has not been clinically validated).

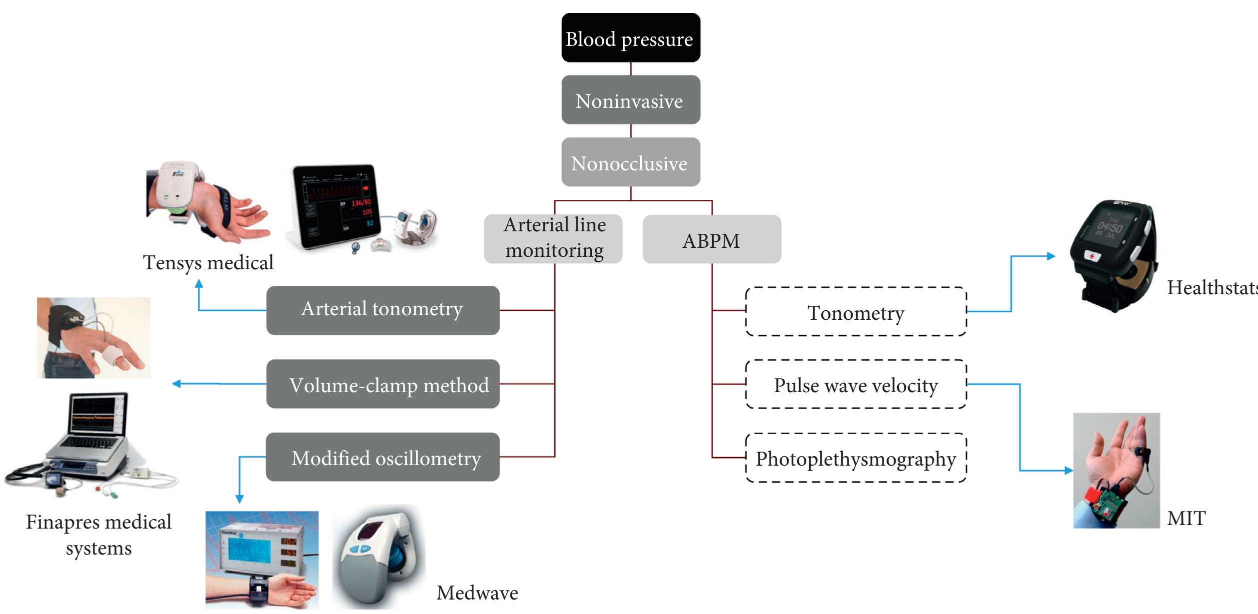

Figure 5: Cuffless blood pressure measurement technologies and products.

(PWV), which is a method of estimating the blood pressure using the phenomenon that the pressure inside the artery (that is, blood pressure) changes the elasticity of the artery and changes the time of the pulse wave from the heart to the peripheral artery.

The PWV can be calculated by dividing the artery length with the pulse transit time (PTT) or pulse arrival time (PAT), which can be derived combining the feature points (peak, valley, peak of 1st derivative, etc.) of electrocardiogram (ECG), photoplethysmogram (PPG) [39–46], phonocardiogram (PCG) [47], seismocardiogram (SCG) [48], and ballistocardiogram (BCG) [49, 50]. Sometimes the PTT and PAT are used as the same; however, the strict meaning of the pulse arrival time is the sum of pulse transit time and preejection period (PEP) [63]. Figure 6 shows a typical example of PWV methodology, which uses the peaks of ECG and PPG. The PAT in Figure 6 includes the preejection time due to the use of the ECG. Detailed descriptions of PTT and PAT measurements can be found in previous studies [63].

The difficulties or problems of conventional blood pressure estimation techniques using PWV can be summarized as follows:

(1) Because the elasticity of an artery changes not only by blood pressure but also by other factors such as the environment, temperature, and emotion, it is difficult to estimate the accurate blood pressure when the arterial characteristics change with time. In addition, when the pulse arrival time including PEP is used for PWV calculation, the PEP fluctuation is expected to reduce the accuracy of the blood pressure estimation [63–66].

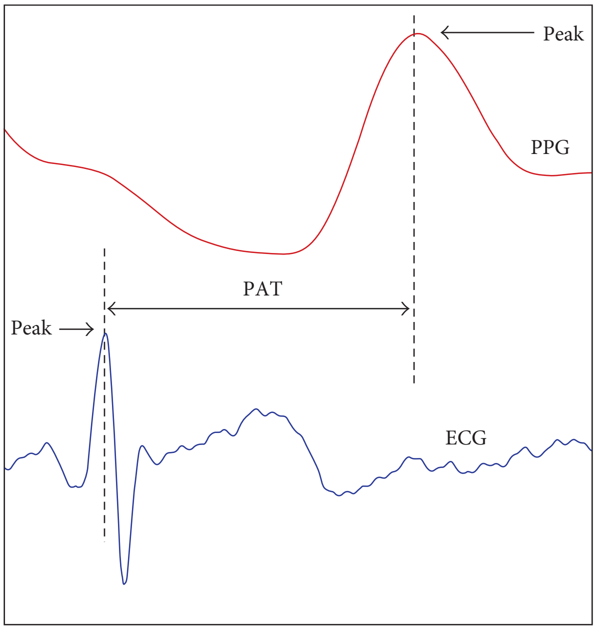

Figure 6: Measurement of pulse arrival time (PAT) using photoplethysmogram (PPG) and electrocardiogram (ECG).

(2) Calibration using a conventional sphygmomanometer with cuff is always necessary since the PWV method does not measure the blood pressure values directly.
(3) Since systolic and diastolic blood pressures are independent of each other, additional information other than the PWV measurement is needed to obtain the two blood pressure values (two equations are needed for two unknowns to be solved; however, only one PWV can be measured). Therefore, accurate estimation of systolic and diastolic blood pressure requires efforts to find new and effective features besides PWV, as shown in a recent work [50].

In conclusion, the cuffless blood pressure estimation technology using PWV for wearable devices should be designed and developed to overcome such shortcomings.

4. Conclusions

An increase in the cost of healthcare due to aging necessitates the establishment of a more effective healthcare system. The healthcare function of the wearable device can be very useful for efficient preventive/postmanagement services in that the user's body information can be monitored, and communication with healthcare professionals is always possible. Among various wearable devices, the wristband is most suitable for acquiring biomedical signals, so it is highly likely to be useful in a new medical system. The sensors of wristband for health-related functions are mainly composed of accelerometer, optical sensor, and electrodes. Using the combinations of these sensors, wristband measures most functions of the patient monitoring system in hospital except blood pressure measurement.

Therefore, the biggest leap in health-related functions of wristband-type devices is expected to be blood pressure measurement technology without cuff, and it is expected to have a ripple effect as the technical difficulty is very high. However, even if a new blood pressure sensing technology is not developed early, the 24-hour continuous biosignal measurement function of the wearable device, which has been developed so far, provides biosignals in daily life in various environments. Unlike patient data measured in hospitals, it will provide new medical implications and possibilities for healthcare services, and these efforts are expected to continue.

Conflicts of Interest

The author declares that there are no conflicts of interest regarding the publication of this paper.

Acknowledgments

This research was supported by the Basic Science Research Program through the National Research Foundation of Korea (NRF) funded by the Ministry of Education (NRF-2018R1D1A1B07050427) and Soonchunhyang University Research Fund (No. 20170476).

References

[1] S. A. Schroeder, "We can do better—improving the health of the American people," *New England Journal of Medicine*, vol. 357, no. 12, pp. 1221–1228, 2007.
[2] PWC, *The Wearable Life 2.0—Connected Living in a Wearable World*, PWC, London, UK, 2016.
[3] Fitbit, https://www.fitbit.com/store.
[4] Garmin, https://www.garmin.com/en-US/.
[5] Apple, https://www.apple.com/watch/.
[6] Samsung Electronics, https://www.samsung.com/us/mobile/wearables/smart-fitness-bands/.
[7] Enjoyvue, https://www.enjoyvue.com/.
[8] Digitsole, https://www.digitsole.com/.
[9] VitalConnect, https://vitalconnect.com/solutions/vitalpatch/.
[10] Bardy Diagnostics, https://www.bardydx.com/.
[11] iRhythm, https://www.irhythmtech.com/.
[12] VivaLNK, http://www.vivalnk.com/ecg-monitor.
[13] Owlet, https://owletcare.com/products/owlet-smart-sock.
[14] Hexoskin, https://www.hexoskin.com/collections/all.
[15] Sony Network Communications Inc., https://smartsports.sony.net/b-trainer/product/1G/WW/en/index.html.
[16] Jabra, https://www.jabra.com/sports-headphones.
[17] LG Electronics, https://www.lg.com/us/mobile-accessories/lg-FR74-heart-rate-monitor.
[18] Motiv, https://mymotiv.com/.
[19] SSI, *Wearable Technology Grows in Popularity*, SSI, Shelton, CT, USA, 2013.
[20] J. Song, D. Li, X. Ma, G. Teng, and J. Wei, "A robust dynamic heart-rate detection algorithm framework during intense physical activities using photoplethysmographic signals," *Sensors*, vol. 17, no. 11, p. 2450, 2017.
[21] D. Jarchi and A. J. Casson, "Towards photoplethysmography-based estimation of instantaneous heart rate during physical activity," *IEEE Transactions on Biomedical Engineering*, vol. 64, no. 9, pp. 2042–2053, 2017.

[22] Y. Zhang, B. Liu, and Z. Zhang, "Combining ensemble empirical mode decomposition with spectrum subtraction technique for heart rate monitoring using wrist-type photoplethysmography," *Biomedical Signal Processing and Control*, vol. 21, pp. 119–125, 2015.

[23] H. Yuan, S. Poeggel, T. Newe, E. Lewis, C. Viphavakit, and G. Leen, "An experimental study of the effects of external physiological parameters on the photoplethysmography signals in the context of local blood pressure (hydrostatic pressure changes)," *Sensors (Switzerland)*, vol. 17, no. 3, 2017.

[24] S. Mehrang, J. Pietilä, and I. Korhonen, "An activity recognition framework deploying the random forest classifier and a single optical heart rate monitoring and triaxial accelerometer wrist-band," *Sensors (Switzerland)*, vol. 18, no. 2, pp. 1–13, 2018.

[25] Z. Zhang, "Photoplethysmography-based heart rate monitoring in physical activities via joint sparse spectrum reconstruction," *IEEE Transactions on Biomedical Engineering*, vol. 62, no. 8, pp. 1902–1910, 2015.

[26] M. T. Islam, I. Zabir, S. T. Ahamed, M. T. Yasar, C. Shahnaz, and S. A. Fattah, "A time-frequency domain approach of heart rate estimation from photoplethysmographic (PPG) signal," *Biomedical Signal Processing and Control*, vol. 36, pp. 146–154, 2017.

[27] A. Temko, "Accurate heart rate monitoring during physical exercises using PPG," *IEEE Transactions on Biomedical Engineering*, vol. 64, no. 9, pp. 2016–2024, 2017.

[28] H. Park, S. Y. Dong, M. Lee, and I. Youn, "The role of heart-rate variability parameters in activity recognition and energy-expenditure estimation using wearable sensors," *Sensors (Switzerland)*, vol. 17, no. 7, 2017.

[29] A. KR and B. M, "Heart rate estimation from photoplethysmography signal for wearable health monitoring devices," *Biomedical Signal Processing and Control*, vol. 50, pp. 1–9, 2019.

[30] WHO, *Global Health Risks—Mortality and Burden of Disease Attributable to Selected Major Risks*, WHO, Geneva, Switzerland, 2009.

[31] T. G. Pickering, J. E. Hall, L. J. Appel et al., "Recommendations for blood pressure measurement in humans and experimental animals," *Circulation*, vol. 111, no. 5, pp. 697–716, 2005.

[32] E. O'brien, R. Asmar, L. Beilin et al., "European society of hypertension recommendations for conventional, ambulatory and home blood pressure measurement," *Journal of Hypertension*, vol. 21, pp. 821–848, 2003.

[33] T. Arakawa, "Recent research and developing trends of wearable sensors for detecting blood pressure," *Sensors*, vol. 18, no. 9, p. 2772, 2018.

[34] A. Chandrasekhar, C.-S. Kim, M. Naji, K. Natarajan, J.-O. Hahn, and R. Mukkamala, "Smartphone-based blood pressure monitoring via the oscillometric finger-pressing method," *Science Translational Medicine*, vol. 10, article eaap8674, 2018.

[35] A. Chandrasekhar, K. Natarajan, M. Yavarimanesh, and R. Mukkamala, "An iPhone application for blood pressure monitoring via the oscillometric finger pressing method," *Scientific Reports*, vol. 8, article 13136, 2018.

[36] D. Nair, S.-Y. Tan, H.-W. Gan et al., "The use of ambulatory tonometric radial arterial wave capture to measure ambulatory blood pressure: the validation of a novel wrist-bound device in adults," *Journal of Human Hypertension*, vol. 22, no. 3, pp. 220–222, 2008.

[37] S. Theilade, C. Joergensen, F. Persson, M. Lajer, and P. Rossing, "Ambulatory tonometric blood pressure measurements in patients with diabetes," *Diabetes Technology & Therapeutics*, vol. 14, no. 6, pp. 453–456, 2012.

[38] C. Ott, S. Haetinger, M. P. Schneider, M. Pauschinger, and R. E. Schmieder, "Comparison of two noninvasive devices for measurement of central systolic blood pressure with invasive measurement during cardiac catheterization," *Journal of Clinical Hypertension*, vol. 14, no. 9, pp. 575–579, 2012.

[39] M. Gao, N. B. Olivier, and R. Mukkamala, "Comparison of noninvasive pulse transit time estimates as markers of blood pressure using invasive pulse transit time measurements as a reference," *Physiological Reports*, vol. 4, no. 10, article e12768, 2016.

[40] J.-J. Huang, H.-Y. Syu, Z.-L. Cai, and A. R. See, "Development of a long term dynamic blood pressure monitoring system using cuff-less method and pulse transit time," *Measurement*, vol. 124, pp. 309–317, 2018.

[41] Y. See, Q. Zhang, and S. Ko, "Noninvasive cuffless blood pressure estimation using pulse transit time and Hilbert-Huang transform," *Computers & Electrical Engineering*, vol. 39, no. 1, pp. 103–111, 2013.

[42] I. Sharifi, S. Goudarzi, and M. B. Khodabakhshi, "A novel dynamical approach in continuous cuffless blood pressure estimation based on ECG and PPG signals," *Artificial Intelligence in Medicine*, 2018.

[43] Q. Liu, C. C. Y. Poon, and Y. T. Zhang, "Time-frequency analysis of variabilities of heart rate, systolic blood pressure and pulse transit time before and after exercise using the recursive autoregressive model," *Biomedical Signal Processing and Control*, vol. 6, no. 4, pp. 364–369, 2011.

[44] A. Attarpour, A. Mahnam, A. Aminitabar, and H. Samani, "Cuff-less continuous measurement of blood pressure using wrist and fingertip photo-plethysmograms: evaluation and feature analysis," *Biomedical Signal Processing and Control*, vol. 49, pp. 212–220, 2019.

[45] Q. Liu, B. P. Yan, C. Yu, Y. Zhang, and C. C. Y. Poon, "Attenuation of systolic blood pressure and pulse transit time hysteresis during exercise and recovery in cardiovascular patients," *IEEE Transactions on Biomedical Engineering*, vol. 61, no. 2, pp. 346–352, 2014.

[46] A. Esmaili, M. Kachuee, and M. Shabany, "Nonlinear cuffless blood pressure estimation of healthy subjects using pulse transit time and arrival time," *IEEE Transactions on Instrumentation and Measurement*, vol. 66, no. 12, pp. 3299–3308, 2017.

[47] A. D. Junior, S. Murali, F. Rincon, and D. Atienza, "Methods for reliable estimation of pulse transit time and blood pressure variations using smartphone sensors," *Microprocessors and Microsystems*, vol. 46, pp. 84–95, 2016.

[48] A. M. Carek, J. Conant, A. Joshi, H. Kang, and O. T. Inan, "SeismoWatch," *Proceedings of the ACM on Interactive, Mobile, Wearable and Ubiquitous Technologies*, vol. 1, no. 3, pp. 1–16, 2017.

[49] P. Yousefian, S. Shin, A. Mousavi et al., "Data mining investigation of the association between a limb ballistocardiogram and blood pressure," *Physiological Measurement*, vol. 39, no. 7, article 075009, 2018.

[50] C.-S. Kim, A. M. Carek, O. T. Inan, R. Mukkamala, and J.-O. Hahn, "Ballistocardiogram-based approach to cuffless blood pressure monitoring: proof of concept and potential challenges," *IEEE Transactions on Biomedical Engineering*, vol. 65, no. 11, pp. 2384–2391, 2018.

[51] S. G. Khalid, J. Zhang, F. Chen, and D. Zheng, "Blood pressure estimation using photoplethysmography only: comparison between different machine learning approaches," *Journal of Healthcare Engineering*, vol. 2018, Article ID 1548647, 13 pages, 2018.
[52] G. Martínez, N. Howard, D. Abbott, K. Lim, R. Ward, and M. Elgendi, "Can photoplethysmography replace arterial blood pressure in the assessment of blood pressure?," *Journal of Clinical Medicine*, vol. 7, no. 10, p. 316, 2018.
[53] P. Szmuk, E. Pivalizza, R. D. Warters, T. Ezri, and R. Gebhard, "An evaluation of the T-line tensymeter continuous non-invasive blood pressure device during induced hypotension," *Anaesthesia*, vol. 63, no. 3, pp. 307–312, 2008.
[54] B. Saugel, A. S. Meidert, A. Hapfelmeier, F. Eyer, R. M. Schmid, and W. Huber, "Non-invasive continuous arterial pressure measurement based on radial artery tonometry in the intensive care unit: a method comparison study using the T-line TL-200pro device," *British Journal of Anaesthesia*, vol. 111, no. 2, pp. 185–190, 2013.
[55] B. Saugel, R. Dueck, and J. Y. Wagner, "Measurement of blood pressure," *Best Practice & Research Clinical Anaesthesiology*, vol. 28, no. 4, pp. 309–322, 2014.
[56] G. Parati, R. Casadei, A. Groppelli, M. Di Rienzo, and G. Mancia, "Comparison of finger and intra-arterial blood pressure monitoring at rest and during laboratory testing," *Hypertension*, vol. 13, pp. 647–655, 1989.
[57] A. E. Schutte, H. W. Huisman, J. M. van Rooyen, N. T. Malan, and R. Schutte, "Validation of the finometer device for measurement of blood pressure in black women," *Journal of Human Hypertension*, vol. 18, no. 2, pp. 79–84, 2004.
[58] X. Monnet, M. Dres, A. Ferré et al., "Prediction of fluid responsiveness by a continuous non-invasive assessment of arterial pressure in critically ill patients: comparison with four other dynamic indices," *British Journal of Anaesthesia*, vol. 109, no. 3, pp. 330–338, 2012.
[59] J. R. Martina, B. E. Westerhof, J. van Goudoever et al., "Noninvasive continuous arterial blood pressure monitoring with Nexfin," *Anesthesiology*, vol. 116, no. 5, pp. 1092–1103, 2012.
[60] K. G. Belani, J. J. Buckley, and M. O. Poliac, "Accuracy of radial artery blood pressure determination with the Vasotrac," *Canadian Journal of Anesthesia*, vol. 46, no. 5, pp. 488–496, 1999.
[61] J. Findlay, B. Gali, M. Keegan, C. Burkle, and D. Plevak, "Vasotrac arterial blood pressure and direct arterial blood pressure monitoring during liver transplantation," *Anesthesia & Analgesia*, vol. 102, no. 3, pp. 690–693, 2006.
[62] L. Peter, N. Noury, and M. Cerny, "A review of methods for non-invasive and continuous blood pressure monitoring: pulse transit time method is promising?," *Innovation and Research in BioMedical Engineering*, vol. 35, pp. 271–282, 2014.
[63] R. Mukkamala, J.-O. Hahn, O. T. Inan et al., "Toward ubiquitous blood pressure monitoring via pulse transit time: theory and practice," *IEEE Transactions on Biomedical Engineering*, vol. 62, no. 8, pp. 1879–1901, 2015.
[64] R. A. Payne, C. N. Symeonides, D. J. Webb, and S. R. J. Maxwell, "Pulse transit time measured from the ECG: an unreliable marker of beat-to-beat blood pressure," *Journal of Applied Physiology*, vol. 100, pp. 136–141, 2006.
[65] G. Zhang, M. Gao, D. Xu, N. B. Olivier, and R. Mukkamala, "Pulse arrival time is not an adequate surrogate for pulse transit time as a marker of blood pressure," *Journal of Applied Physiology*, vol. 111, pp. 1681–1686, 2011.
[66] S. L.-O. Martin, A. M. Carek, C.-S. Kim et al., "Weighing scale-based pulse transit time is a superior marker of blood pressure than conventional pulse arrival time," *Scientific Reports*, vol. 6, article 39273, 2016.

Hindawi
Journal of Healthcare Engineering
Volume 2019, Article ID 6283279, 7 pages
https://doi.org/10.1155/2019/6283279

Research Article

Noise-Robust Heart Rate Estimation Algorithm from Photoplethysmography Signal with Low Computational Complexity

JaeWook Shin and Jaegeol Cho

Department of Medical and Mechatronics Engineering, Soonchunhyang University, Asan, Republic of Korea

Correspondence should be addressed to Jaegeol Cho; jaegeolcho@sch.ac.kr

Received 15 February 2019; Accepted 20 March 2019; Published 21 May 2019

Academic Editor: Patrick Boissy

This paper introduces a noise-robust HR estimation algorithm using wrist-type PPG signals that consist of preprocessing block, motion artifact reduction block, and frequency tracking block. The proposed algorithm has not only robustness for motion noise but also low computational complexity. The proposed algorithm was tested on a data set of 12 subjects and recorded during treadmill exercise in order to verify and compare with other existing algorithms.

1. Introduction

Recently, as interest in health increases, there is a growing demand for users to continuously diagnose diseases or to manage disease by measuring biosignals. In order to meet the needs of users, wearable pace measurement devices based on photoplethysmography (PPG) sensors have been commercialized in many companies [1].

The PPG is a sensor that measures changes in blood vessel contraction and expansion using LEDs and photodiodes. It can be used to measure the heart rate and oxygen saturation in a noninvasive manner and is widely used in wearable devices. However, in case of PPG sensor signals in wearable devices, the heart noise estimation error may be caused by motion artifact (MA) due to body movements. Various algorithms have been developed to overcome this problem. Conventional algorithms mainly use PPG sensor signals of different wavelengths to remove motion noise from the PPG sensor signals or effectively remove motion noise using acceleration sensor signals and measure heartbeat [2–8].

However, the existing algorithms use various signals and use complex algorithms. Therefore, the existing algorithms are difficult to use in wearable devices with constraints of price, power, and system size. To overcome these drawbacks, this paper proposes a PPG sensor with low complexity and an algorithm based on a 3-axis acceleration sensor to estimate the heart rate. To evaluate the performance of the proposed algorithm, we compared the performance of the proposed algorithm with that of the existing algorithms.

2. Methods

In this paper, the algorithm consists of three stages in order to estimate the heart rate during exercise in the wearable device based on the PPG sensor. The first stage is preprocessing the input PPG sensor data and 3-axis acceleration data. The second stage is to remove the MA noise from the PPG sensor signal. The last stage is the frequency tracking to estimate the heart rate in the motion-free signal. The flowchart of the proposed algorithm is shown in Figure 1.

2.1. Data Set. In this paper, we tested the proposed heart rate estimation algorithm using 12 data sets in the IEEE Signal Processing Cup 2015 database [2]. We compared the heart rate with the output of the ECG signals based on the data set.

2.2. Normalized Least Mean Squares Algorithm. The normalized least mean squares (NLMS) algorithm is widely used

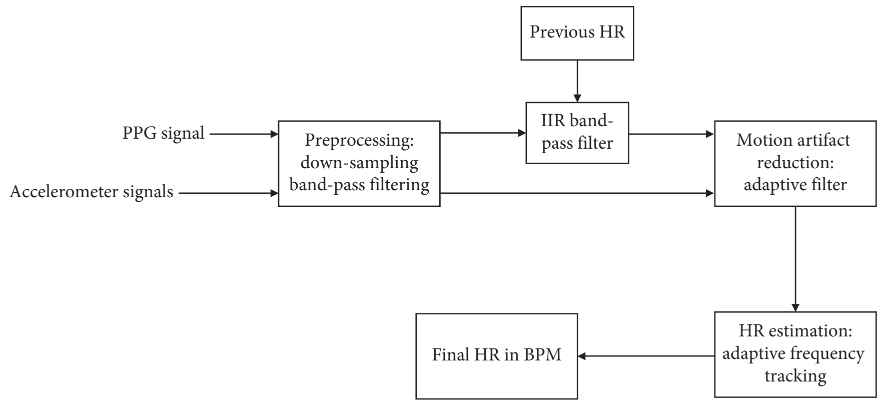

Figure 1: Block diagram of the proposed algorithm.

because it has a simple calculation among various adaptive filters and ease of implementation [9, 10]. We consider data $d(n)$ derived from an unknown system:

$$d(n) = \mathbf{u}^{\mathrm{T}}(n)\mathbf{w} + v(n), \tag{1}$$

where $\mathbf{w}$ is an unknown system that we expect to estimate, $\mathbf{u}$ denote the input vector, v accounts for the measurement noise, and n is the iteration number. Assume that the unknown system order is M, $\mathbf{w}$ and $\mathbf{u}$ are the M-dimensional column vectors. The coefficient $\widehat{\mathbf{w}}(n)$ of the adaptive filter is updated using the difference $e(n)$ between the adaptive filter output signal $y(n)$ and the desired signal $d(n)$ for the input signal $u(n)$ so that the square mean error is minimized. The NLMS algorithm can be expressed as

$$\begin{aligned} \widehat{\mathbf{w}}(n) &= \widehat{\mathbf{w}}(n-1) + \mu\frac{\mathbf{u}(n)}{\mathbf{u}^{\mathrm{T}}(n)\mathbf{u}(n)}e(n), \\ e(n) &= d(n) - y(n) = d(n) - \mathbf{u}^{\mathrm{T}}(n)\widehat{\mathbf{w}}(n-1), \end{aligned} \tag{2}$$

where μ is the step size, $0 < \mu \le 1$.

2.3. Low Computational Complexity MA Reduction Algorithm. The PPG signal includes noise-free signals and the MA that is generated due to the movement of the body. Because MA is highly correlated with the acceleration sensor signals, a clean PPG Signal can be obtained to remove a signal having a high correlation with the acceleration sensor from the PPG signal. Therefore, the corrupted PPG signals are used as desired signal $d(n)$ and 3-axis accelerometer signals are used as input signal $u(n)$ to reduce the MA as shown in Figure 2.

The conventional NLMS algorithm requires $3M+1$ multiplication when the order of the adaptive filter is M. Despite the small computational complexity of the NLMS, an algorithm with a small computational complexity is required for wearable systems due to price, power, and system size limitations. In order to overcome this drawback, we propose an adaptive noise cancellation algorithm which can have similar performance with low computational complexity as follows:

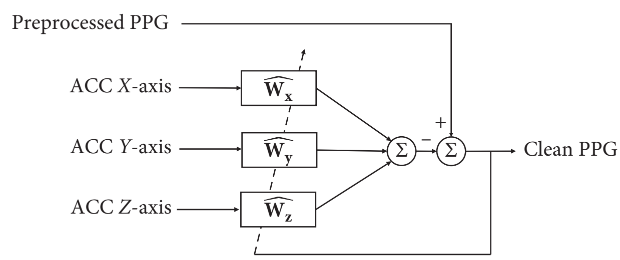

Figure 2: Adaptive filter for motion artifact reduction.

$$\widehat{\mathbf{w}_{\mathrm{x}}}(n) = \widehat{\mathbf{w}_{\mathrm{x}}}(n-1) + \mu\frac{\operatorname{sign}(\mathbf{u}_{\mathrm{x}}(n))}{\operatorname{sign}(\mathbf{u}_{\mathrm{x}}^{\mathrm{T}}(n))\operatorname{sign}(\mathbf{u}_{\mathrm{x}}(n))}\operatorname{sign}(e(n)), \tag{3}$$

$$\widehat{\mathbf{w}_{\mathrm{y}}}(n) = \widehat{\mathbf{w}_{\mathrm{y}}}(n-1) + \mu\frac{\operatorname{sign}(\mathbf{u}_{\mathrm{y}}(n))}{\operatorname{sign}(\mathbf{u}_{\mathrm{y}}^{\mathrm{T}}(n))\operatorname{sign}(\mathbf{u}_{\mathrm{y}}(n))}\operatorname{sign}(e(n)), \tag{4}$$

$$\widehat{\mathbf{w}_{\mathrm{z}}}(n) = \widehat{\mathbf{w}_{\mathrm{z}}}(n-1) + \mu\frac{\operatorname{sign}(\mathbf{u}_{\mathrm{z}}(n))}{\operatorname{sign}(\mathbf{u}_{\mathrm{z}}^{\mathrm{T}}(n))\operatorname{sign}(\mathbf{u}_{\mathrm{z}}(n))}\operatorname{sign}(e(n)), \tag{5}$$

$$e(n) = d(n) - y(n), \tag{6}$$

$$\begin{aligned} y(n) = {} & \operatorname{sign}\left(\mathbf{u}_{\mathrm{x}}^{\mathrm{T}}(n)\right)\widehat{\mathbf{w}_{\mathrm{x}}}(n-1) + \operatorname{sign}\left(\mathbf{u}_{\mathrm{y}}^{\mathrm{T}}(n)\right)\widehat{\mathbf{w}_{\mathrm{y}}}(n-1) \\ & + \operatorname{sign}\left(\mathbf{u}_{\mathrm{z}}^{\mathrm{T}}(n)\right)\widehat{\mathbf{w}_{\mathrm{z}}}(n-1), \end{aligned} \tag{7}$$

where $\operatorname{sign}(\cdot)$ denotes the sign function and $\mathbf{u}_{\mathrm{x}}$, $\mathbf{u}_{\mathrm{y}}$, and $\mathbf{u}_{\mathrm{z}}$ denote x-axis, y-axis, and z-axis accelerometer signal, respectively.

Due to use of only the sign of the input signal vector and the error, the proposed algorithm requires only M multiplications because the multiplication required in Equations (3)–(5) and (7) can be calculated by adding. Therefore, the algorithm can be implemented with a small amount of computation compared to the existing NLMS algorithm. In particular, calculation time can be further shortened for using a CPU without a floating point unit.

2.4. Adaptive Frequency Tracking. We used an oscillator-based adaptive notch filter (OSC-ANF) algorithm [11] to estimate the heart rate using the PPG signal that passed through the MA reduction stage. The OSC-ANF algorithm is based on a second-order IIR band-pass filter and traces the strongest frequency of the signal. The OSC-ANF algorithm operates as follows:

$$\begin{aligned} x(n) &= \widehat{\alpha}(n)(1+\beta)x(n-1) - \beta x(n-2) \\ &\quad + 0.5(1-\beta)(\operatorname{sign}(e(n)) - \operatorname{sign}(e(n-2))), \\ e_\alpha(n) &= x(n) - 2\widehat{\alpha}(n)x(n-1) + x(n-2), \\ P_x(n) &= (1-\mu_a)P_x(n-1) + \mu_a x^2(n-1), \\ \widehat{\alpha}(n+1) &= \widehat{\alpha}(n) + \mu_a \frac{x(n-1)}{2P_x(n)} e_\alpha(n), \\ \omega(n+1) &= \cos^{-1}(\widehat{\alpha}(n+1)), \\ HR_{\text{est}}(n+1) &= \omega(n+1) \times \frac{f_s}{2\pi} \times 60, \end{aligned} \tag{8}$$

where $\omega(n+1)$ is the estimated frequency, $HR_{\text{est}}(n+1)$ is the estimated HR in BPM, f_s is the sampling rate, μ_a is the step size, and β controls the 3 dB bandwidth of the 2^{nd} order IIR band-pass filter.

2.5. Noise-Robust Adaptive Frequency Tracking. To improve the tracking performance of the OSC-ANF algorithm under highly noisy environments, we propose the noise-robust OSC-ANF (NR-OSC-ANF) algorithm that is derived by noise-robust adaptive filter concept [12, 13] as follows:

$$\begin{aligned} \overline{\alpha}(n) &= \frac{1}{L}\sum_{l=0}^{L-1} \widehat{\alpha}(n-l), \\ e_\alpha(n) &= x(n) - 2\overline{\alpha}(n)x(n-1) + x(n-2), \\ P_x(n) &= (1-\mu_a)P_x(n-1) + \mu_a x^2(n-1), \\ \widehat{\alpha}(n+1) &= \overline{\alpha}(n) + \mu_a \frac{x(n-1)}{2P_x(n)} e_\alpha(n). \end{aligned} \tag{9}$$

By using the average of the past estimated frequencies, the NR-OSC-ANF algorithm makes improved frequency tracking performance in low signal-to-noise ratio (SNR) environments.

In addition, to improve MA reduction performance, we further use IIR band-pass filter, the preprocessed PPG signal by estimated $\widehat{\alpha}(n+1)$, as follows:

$$\begin{aligned} d_{\text{hr}}(n) &= \widehat{\alpha}(n)(1+\beta_{\text{hr}})d(n-1) - \beta_{\text{hr}} d(n-2) \\ &\quad + 0.5(1-\beta_{\text{hr}})(d(n) - d(n-2)). \end{aligned} \tag{10}$$

The output of IIR band-pass filter $d_{\text{hr}}(n)$ is used as the desired signal for adaptive filter instead of $d(n)$ in the MA reduction step.

2.6. Performance Measurement. To verify the performance of the proposed algorithm, 12 data sets of IEEE Signal Processing Cup 2015 database were used. The data set used provides the reference heart rate measured from the electrocardiogram as well as the PPG sensor signal and the acceleration sensor signal. To compare the performance of the algorithm, we used the two methods that average absolute error and average absolute error percentage as follows:

$$\begin{aligned} \text{Error1} &= \frac{1}{N}\sum_{n=1}^{N} \left| HR_{\text{est}}(n) - HR_{\text{true}}(n) \right|, \\ \text{Error2} &= \frac{1}{N}\sum_{n=1}^{N} \frac{\left| HR_{\text{est}}(n) - HR_{\text{true}}(n) \right|}{HR_{\text{true}}(n)}. \end{aligned} \tag{11}$$

3. Results and Discussion

3.1. Parameter Settings. In order to reduce the computational complexity, we use down-sampled PPG and accelerometer signal that are resampled 125 Hz to 25 Hz. Figure 3 shows the average absolute error of the proposed algorithm with various filter tap lengths which used MA reduction step. As can be seen, the proposed algorithm has best performance when the adaptive filter order is 21 ($M = 21$). Parameter setting of the proposed algorithm is summarized in Table 1.

3.2. Performance of the Proposed Algorithm. In this paper, we verified the performance of the proposed heart rate estimation algorithm using 12 data sets in the IEEE Signal Processing Cup 2015 database. Error1 and Error2 were obtained for each set and compared with other algorithms by comparing the heart rate output through the three-stage algorithm and the ECG signal-based heart rate provided by the data set. Figure 4 shows that the proposed algorithm can sufficiently remove motion artifacts even with low computational complexity. Figure 5 is the HR tracking results plot on test data set 08 and set 09 with ECG-based HR. The estimated HR form PPG signal matches with ECG-based HR satisfactorily.

Tables 2 and 3 show that the performances of other existing algorithms and the proposed algorithm do not differ greatly. Although the proposed algorithm does not have best performance compared with other algorithms, it is considered to be worthy of an algorithm for use in a wearable device because of its low computational complexity. The proposed algorithm requires only few multiplication for preprocessing and NR-OSC-ANF.

Figure 6 shows Bland–Altman plot for the training data set. In this case, the limits of agreement were [−3.97, 5.04] BPM. Figure 7 indicates the scatter plot between the ground

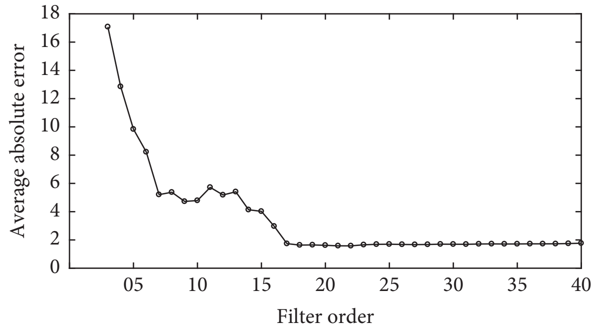

Figure 3: Filter order selection.

Table 1: Parameter setting.

Algorithm	Parameters
MA reduction algorithm	$M = 21$, $\mu = 0.0001$
NR-OSC-ANF	$L = 5$, $\beta = 0.95$, $\mu_a = 0.025$
IIR band-pass filter	$\beta_{hr} = 0.8$

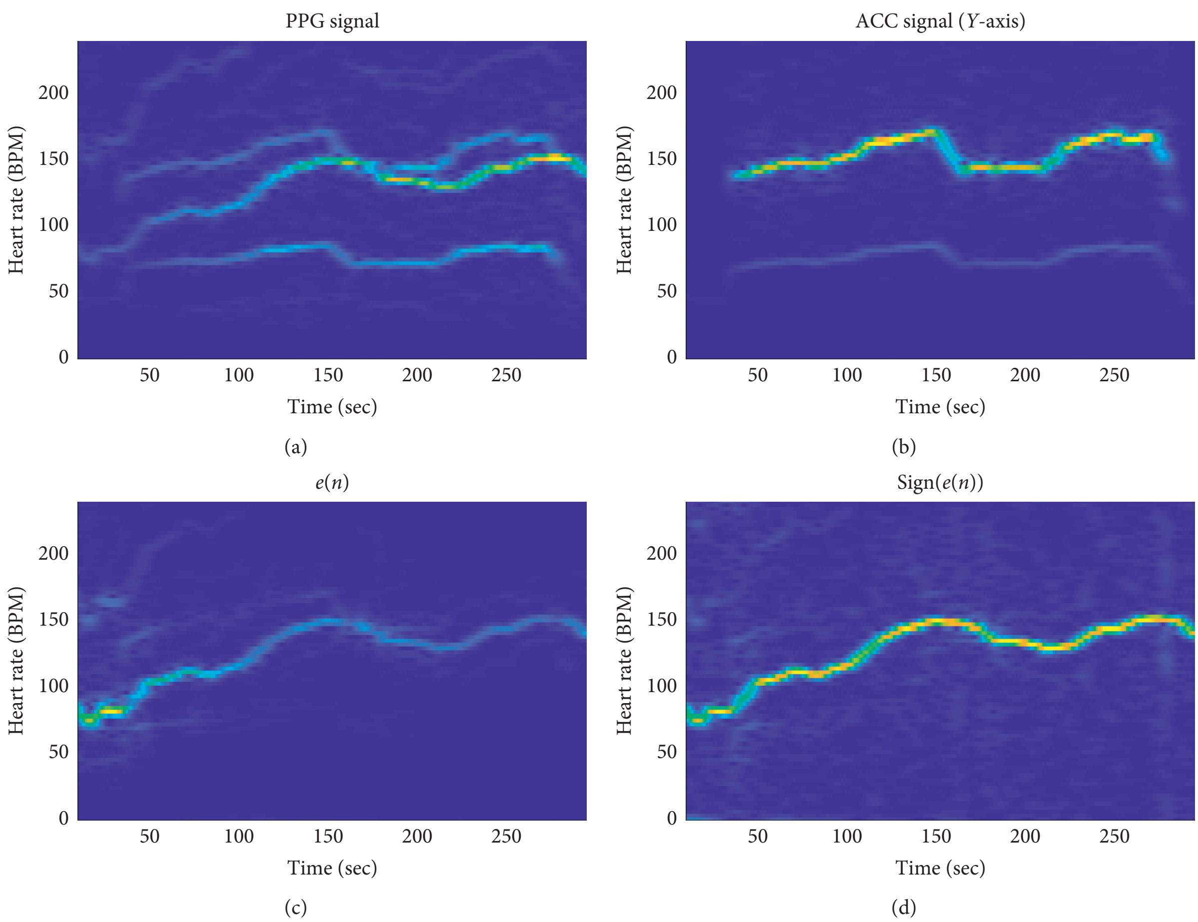

Figure 4: Continued.

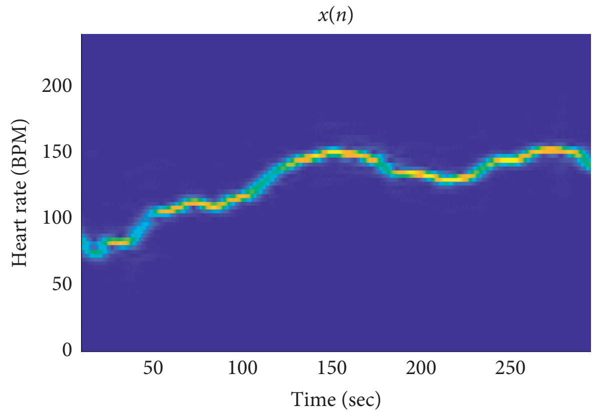

(e)

Figure 4: Frequency spectrogram of various signals.

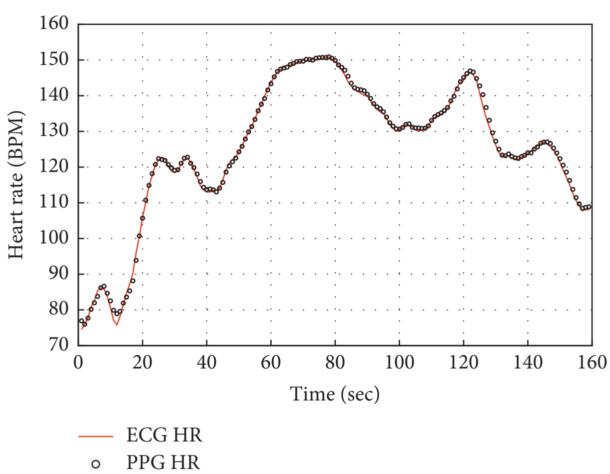

(a)

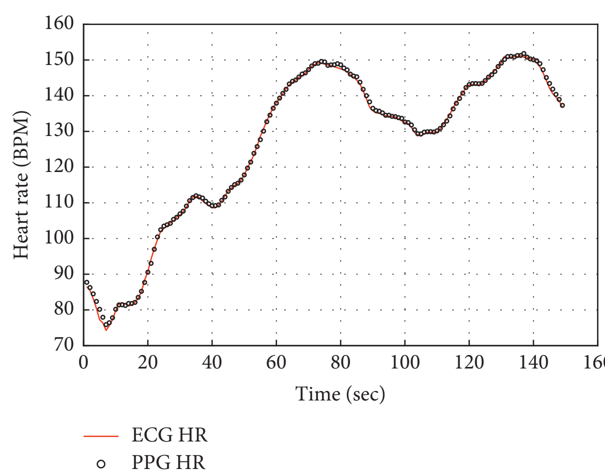

(b)

Figure 5: HR estimation results for (a) set 08 and (b) set 09.

Table 2: Error1 results of the proposed algorithm and the existing algorithms.

Data set	TROIKA [2]	JOSS [3]	NLMS + OSC-ANFc [7]	Combination of adaptive filters [8]	Proposed algorithm
1	2.29	1.33	1.75	1.34	1.33
2	2.19	1.75	1.94	0.70	1.92
3	2.00	1.47	1.17	0.66	0.83
4	2.15	1.48	1.67	0.70	1.03
5	2.01	0.69	0.95	0.63	0.54
6	2.76	1.32	1.22	0.86	1.44
7	1.67	0.71	0.91	0.66	0.65
8	1.93	0.56	1.17	0.58	0.56
9	1.86	0.49	0.87	0.52	0.43
10	4.70	3.81	2.95	2.46	2.51
11	1.72	0.78	1.15	1.21	0.83
12	2.84	1.04	1.00	0.74	1.79
Av. ± std	2.34 ± 0.79	1.29 ± 0.86	1.40 ± 0.58	0.92 ± 0.52	1.16 ± 0.62

Table 3: Error2 results of the proposed algorithm and the existing algorithms.

Data set	TROIKA [2]	NLMS + OSC-ANFc [7]	Combination of adaptive filters [8]	Proposed algorithm
1	1.90	1.59	1.17	1.06
2	1.87	1.99	0.70	2.18
3	1.66	1.02	0.57	0.72
4	1.82	1.51	0.63	0.97
5	1.49	0.75	0.49	0.41
6	2.25	1.05	0.67	1.23
7	1.26	0.72	0.50	0.50
8	1.62	1.04	0.50	0.50
9	1.59	0.76	0.46	0.38
10	2.93	0.93	1.56	1.59
11	1.15	0.79	0.80	0.57
12	1.99	0.79	0.55	1.21

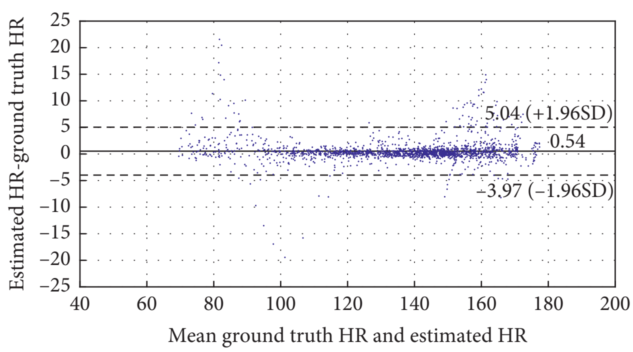

Figure 6: Bland–Altman plot.

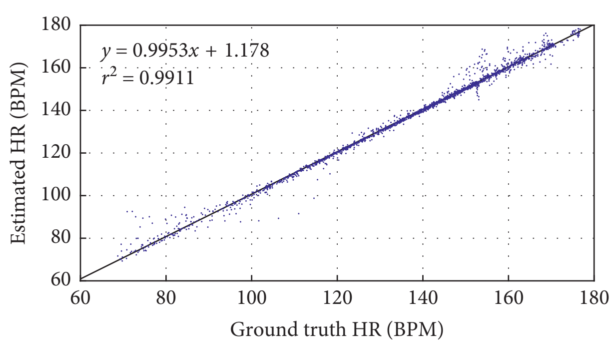

Figure 7: Scatter plot.

truth HR and estimated HR. The fitted line was $y = 0.9953x + 1.178$, where x is the ground truth HR and y is the estimated HR.

4. Conclusions

This paper presents a noise-robust HR estimation algorithm using PPG signals that have not only robustness for motion noise but also low computational complexity. In order to verify the performance of the proposed heart rate estimation algorithm, we compared with other existing algorithms using the IEEE Signal Processing Cup 2015 database.

Data Availability

The data used to support the findings of this study are available from the corresponding author upon request.

Conflicts of Interest

The authors declare that there are no conflicts of interest regarding the publication of this paper.

Acknowledgments

This work was supported by the Soonchunhyang University Research Fund (No. 20170809). This research was also supported by Basic Science Research Program through the National Research Foundation of Korea (NRF) funded by the Ministry of Education (NRF-2018R1D1A1B07050427).

References

[1] D. J. Terbizan, B. A. Dolezal, and C. Albano, "Validity of seven commercially available heart rate monitors," *Measurement in Physical Education and Exercise Science*, vol. 6, no. 4, pp. 243–247, 2002.

[2] Z. Zhang, Z. Pi, and B. Liu, "TROIKA: a general framework for heart rate monitoring using wrist-type photoplethysmographic signals during intensive physical exercise," *IEEE Transactions on Biomedical Engineering*, vol. 62, no. 2, pp. 522–531, 2015.

[3] Z. Zhang, "Photoplethysmography-based heart rate monitoring in physical activities via joint sparse spectrum reconstruction," *IEEE Transactions on Biomedical Engineering*, vol. 62, no. 8, pp. 1902–1910, 2015.

[4] D. Dao, S. M. A. Salehizadeh, Y. Noh et al., "A robust motion artifact detection algorithm for accurate detection of heart rates from photoplethysmographic signals using time-frequency spectral features," *IEEE Journal of Biomedical and Health Informatics*, vol. 21, no. 5, p. 1, 2017.

[5] Y. Fujita, M. Hiromoto, and T. Sato, "PARHELIA: particle filter-based heart rate estimation from photoplethysmographic signals during physical exercise," *IEEE Transactions on Biomedical Engineering*, vol. 65, no. 1, p. 1, 2018.

[6] D. Zhao, Y. Sun, S. Wan, and F. Wang, "SFST: a robust framework for heart rate monitoring from photoplethysmography signals during physical activities," *Biomedical Signal Processing and Control*, vol. 33, pp. 316–324, 2017.

[7] S. Fallet and J.-M. Vesin, "Robust heart rate estimation using wrist-type photoplethysmographic signals during physical exercise: an approach based on adaptive filtering," *Physiological Measurement*, vol. 38, no. 2, pp. 155–170, 2017.

[8] K. R. Arunkumar and M. Bhaskar, "Heart rate estimation from photoplethysmography signal for wearable health monitoring devices," *Biomedical Signal Processing and Control*, vol. 50, pp. 1–9, 2019.
[9] A. Sayed, *Fundamentals of Adaptive Filtering*, Wiley, New York, NY, USA, 2003.
[10] S. Haykin, *Adaptive Filter Theory*, Prentice-Hall, Upper Saddle River, NJ, USA, 4th edition, 2002.
[11] H. Liao, "Two discrete oscillator based adaptive notch filters (OSC ANFs) for noisy sinusoids," *IEEE Transactions on Signal Processing*, vol. 53, no. 2, pp. 528–538, 2005.
[12] Y. S. Choi, S. E. Kim, and W. J. Song, "Noise-robust normalised subband adaptive filtering," *Electronics Letters*, vol. 48, no. 8, pp. 11-12, 2012.
[13] H. Zhao, Z. Zheng, Z. Wang, and B. Chen, "Improved affine projection subband adaptive filter for high background noise environments," *Signal Processing*, vol. 137, pp. 356–362, 2017.

Hindawi
Journal of Healthcare Engineering
Volume 2019, Article ID 4501502, 8 pages
https://doi.org/10.1155/2019/4501502

Research Article

Quantitative Assessment of Autonomic Regulation of the Cardiac System

Jian Kang Wu,[1,2] **Zhipei Huang**,[1] **Zhiqiang Zhang**,[3] **Wendong Xiao**,[4] **and Hong Jiang**[5]

[1]*The University of Chinese Academy of Sciences, Beijing, China*
[2]*Institute of Healthcare Technologies, Chinese Academy of Sciences, Nanjing, China*
[3]*University of Leeds, West Yorkshire, UK*
[4]*Beijing University of Science and Technology, Beijing, China*
[5]*China-Japan Friendship Hospital, Beijing, China*

Correspondence should be addressed to Jian Kang Wu; jkwu@ucas.ac.cn and Zhipei Huang; zhphuang@ucas.ac.cn

Received 8 January 2019; Accepted 27 March 2019; Published 21 April 2019

Guest Editor: Jilong Kuang

Autonomic neural system (ANS) regulates the circulation to provide optimal perfusion of every organ in accordance with its metabolic needs, and the quantitative assessment of autonomic regulation is crucial for personalized medicine in cardiovascular diseases. In this paper, we propose the Dystatis to quantitatively evaluate autonomic regulation of the human cardiac system, based on homeostatis and probabilistic graphic model, where homeostatis explains ANS regulation while the probability graphic model systematically defines the regulation process for quantitative assessment. The indices and measurement methods for three well-designed scenarios are also illustrated to evaluate the proposed Dystatis: (1) heart rate variability (HRV), blood pressure variability (BPV), and respiration synchronization (Synch) in resting situation; (2) chronotropic competence indices (CCI) in graded exercise testing; and (3) baroreflex sensitivity (BRS), sympathetic nerve activity (SNA), and parasympathetic nerve activity (PNA) in orthostatic testing. The previous clinical results have shown that the proposed method and indices for autonomic cardiac system regulation have great potential in prediction, diagnosis, and rehabilitation of cardiovascular diseases, hypertension, and diabetes.

1. Introduction

Autonomic neural system (ANS) regulates the circulation to provide optimal perfusion of every organ in accordance with its metabolic needs. Together with the endocrine and immunological systems, it adjusts the internal environment of the organism to respond the changes in the external environment [1]. Therefore, understanding the ANS and the way it regulates body circulation is crucial for personalized medicine in cardiovascular diseases. The understanding of the ANS regulation in the cardiac system can be traced back to the findings of two Nobel Prize winners: (1) Corneille Heymans in 1938 identified the carotid sinus nerves [2], which are tiny baroreceptor and chemoreceptor nerves and can sense changes in hemodynamic pressure and humoral factors and send output to the sympathetic and parasympathetic nerves, and (2) Axelrod [3], Von Euler [4], and Del and Katz [5] identified acetylcholine (ACh) as a transmitter for the parasympathetic nerves, norepinephrine (NE), and sympathetic nerves. However, the ANS regulation of the cardiac system can be viewed as a complex dynamic system, and it can be well described by "Homeostasis" [6], which is now regarded as one of the core competencies by the American Association of Medical Colleges and Howard Hughes Medical Institute and a core concept necessary for future physicians [7].

In clinical settings, autonomic dysfunction has been linked to direct detrimental effects towards heart failure and chronic kidney disease [8]; thus, quantitative methods to evaluate the ANS regulation has great potential to generate innovative diagnostic and treatment approaches that limit hypertension and target end-organ damage. Recent research has shown that the autonomic neurohumoral system can dramatically influence morbidity and mortality from cardiovascular disease through influences on the innate and adaptive immune systems [9]. Due to the high metabolic rate of brain tissue, the precise regulation of cerebral blood flow (CBF) is critical for maintenance of constant nutrient and oxygen supply to the brain [10]. The metabolic syndrome is characterized by the clustering of various common metabolic abnormalities in an individual, which is also associated with increased risk for the development of type 2 diabetes and cardiovascular diseases. The augmented sympathetic activity in individuals with metabolic syndrome worsens prognosis of this high-risk population [11]. Experimental and clinical investigations have validated the hypothesis: the origin, progression, and outcome of human hypertension are related to dysfunctional autonomic cardiovascular control, which is particularly true for abnormal activation of the sympathetic division [12].

Since the quantitative assessment of the autonomic regulation is tremendously important for clinical and healthcare applications, there is urgent need to quantitatively evaluate the ANS regulation status. Unfortunately, there are only two invasive methods to measure certain aspects of the ANS thus far: (1) microneurography to assess muscle sympathetic nerve activity and (2) the norepinephrine isotope dilution to determine noradrenalin in the blood to evaluate spillover of the sympathetic nervous system [13]. Although HRV is an indirect biomarker of the cardiac autonomic nervous system activity [14], ANS regulation of the cardiac system is complex in nature and existing HRV assessment is rather ad hoc without any theoretical model. Therefore, HRV indices obtained in different settings and by different persons are often inconsistent, resulting in difficulties for clinical interpretation.

In summary, ANS regulation of the cardiac system plays a central role in both research and clinical practices, and we will focus on the quantitative assessment of autonomic regulation of the cardiac system in this paper. The main contributions are as follows:

(i) We propose the Dystatis to quantitatively evaluate autonomic regulation of the human cardiac system, based on homeostatis and the probabilistic graphic model, where homeostatis explains ANS regulation while the probability graphic model systematically defines the regulation process for quantitative assessment.

(ii) The Dystatis is elaborated in three well-designed scenarios, where indices and measurement methods for each scenario are also proposed and illustrated by clinical applications:

(1) HRV, BRV, and Synch in resting situation: Dystatis provides theoretical model and guidelines for the test design and data processing and interpretations, in order to solve existing inconsistence problems.

(2) CCI in graded exercise testing: Dystatis metabolic requirement is enlarged by graded exercise so that CCI can be obtained without considering effects from other internal and external interactions. These are minor compared to graded exercises.

(3) BRS, SNA, and PNA in orthostatic testing: based on Dystatis, orthostatic testing creates a large blood pressure drop and then a large BRS output to sympathetic and parasympathetic nerves. As such, the mathematical model for solution of BRS, SNA, and PNA can be greatly simplified by neglecting other internal and external interactions in the ANS regulation.

2. Dystasis: Systematic Quantitative Assessment Methodology for ANS Regulation of the Cardiac System

Human body is a complex biological system, of which homeostasis is a crucial property in maintaining the life. It is the self-regulating process by which biological systems maintain stability in order to adjust to conditions that are optimal for survival. The stability attained is a dynamic equilibrium, in which continuous change occurs yet relatively uniform conditions prevail.

Dystasis is built up on homeostasis and defined as follows: ANS regulation of the cardiac system is a part of body's complex biological system. Through ANS self-regulating process, the cardiac system tends to reach and maintain a dynamic equilibrium state, in order to supply cells and organs with their metabolic needs, e.g., oxygen, nutrients, and removal of waste, survive in various internal and external environments, and support various physical and mental activities. The characteristics of Dystasis are (1) equilibrium: the ANS self-regulating process of the cardiac system reaches and maintains an "equilibrium" state in a relative steady internal and external environment, with no or minor changes in terms of physical and mental activities. The property and its numerical measures of the state of this equilibrium of the individual's ANS self-regulating process shall provide quantitative performance evaluation of how well one's ANS regulation system works; (2) dynamic: the ANS self-regulating process of cardiac system should be "dynamic" enough, being able to work in dynamic environment, support various physical and mental activities of the body, and defend virus invasions. In other words, it should be able to reach new equilibrium state as soon as possible when there is a change of internal/external environment or physical/mental activities. For instance, ANS regulation interacts with the immune system to control inflammation [15] and ANS regulation of the cardiac system increases oxygen supply and reaches a new equilibrium when the intensity of physical activity increases to a new level. The capability of ANS regulation to accommodate changes of internal and external environment, as well as activity needs, is another important measure.

In order to quantitatively evaluate the state and capability of ANS regulation of the cardiac system, one feasible approach is the probabilistic graphic model-based approach [16], as shown in Figure 1. Principally, the interactions of

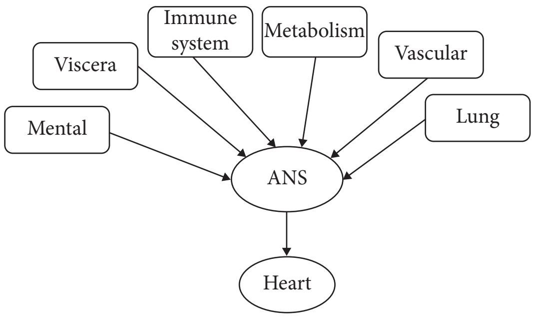

Figure 1: Probabilistic graphic model of autonomic regulation of the cardiac system with internal and external influences.

ANS with cardiac, respiration, vascular, metabolic, immune, viscera, and mental systems are bidirectional [17]. Here, in Figure 1, the objective is to estimate ANS state through all possible observations, in case of ANS regulation of the heart rate with major internal and external influences; i.e., RSA is a terminology for heart rate modulation by respiration; blood pressure formed in the vascular system and sensed by baroreflex which then affects the heartbeat; physical activities stimulate metabolic needs and increase the heart rate; inflammation in the immune system breaks the stability of ANS regulation and then heart rate variations; the dorsal vagal complex is responsible for the interaction between viscera organs and ANS; and the ventral vagal complex is responsible for mental activities [17]. The observation of ANS regulation here is variations of the heart rate, blood pressure, and respiration. The sympathetic innervation of the heart and blood vessels is excitatory. It stimulates vasoconstriction and increases the heart rate and cardiac contraction. On contrary, the parasympathetic vagal innervation is inhibitory, which decreases the heart rate and cardiac contraction. The balance of the two appears as variations of the heart rate and blood pressure and can be characterized by indices which represent properties and rules of those variations caused by regulation: The sympathetic activity increases during the flight-or-fight response, whereas parasympathetic activity increases to calm the heart when there appears emotionally driven high blood pressure.

For the estimation purpose and from Figure 1, we can obtain the following formula, via probabilistic graphic model:

$$\begin{aligned} P = {} & p(\text{heart}/A)\ p(A/\text{mental})\ p(A/\text{viscera}) \\ & \cdot p(A/\text{immune})\ p(A/\text{metabolic})\ p(A/\text{vascular}) \\ & \cdot p(A/\text{lung}), \end{aligned} \tag{1}$$

where A is the state of ANS to be estimated through observations connected with ANS in the graph of Figure 1. However, not all nodes connected with the ANS node are observable or measurable. For the quantitative assessment purpose, it is the best to intentionally create assessment scenario where the influences of the measurable nodes are maximized whilst minimizing those of the unmeasurable nodes. Therefore, we designed the following three assessment scenarios:

(1) Variability of the heart rate and blood pressure (HRV and BPV) while the subject is in resting or other steady state: the ideal measurement scenario is zero or known steady physical activity, minimal mental activity, and minimal viscera disturbance. The variability indices are used to characterize the state of equilibrium of individual's ANS self-regulating process, which directly reflects states of immune system, linking with inflammation biomarkers.

(2) CCI in graded exercise testing: the effect of physical activity on ANS is maximized so that the influences from the rest sources can be neglected. CCI provide numerical measures to characterize the capability of ANS regulation to accommodate changes of exercise intensity.

(3) BRS, SNA, and PNA are obtained by model-based analysis of blood pressure (BP) and heart rate (HR) pairs acquired in orthostatic testing: Via orthostatic test, large blood pressure drops around 30 mmh is obtained. The input from baroreflex to SNA and PNA becomes the major effect, and the rest can be neglected. As such, the mathematical model for the solution can be simplified as a subgraph of the graphic model in Figure 1.

3. Variabilities in Resting or Steady Testing Scenario

The indices of HRV and BPV consist of time-domain second-order statistics, for example, standard deviation of ECG normal-to-normal intervals (SDNN) and standard deviation of differences of neighboring normal-to-normal intervals (SDSD). Frequency-domain indices are calculated at very low frequency band (VLF, 0.004–0.04 Hz), low frequency band (LF, 0.04–0.15 Hz), and high frequency band (0.15–0.4 Hz). The problem is then to quantitatively evaluate the state of ANS and infer the physiological and psychological implications, given measured variabilities of the heart rate, blood pressure, respiration, and assessment scenario that the physical activity is zero or constant. Based on Dystasis framework, according to equation (1) and graphic model in Figure 1, there are still three nodes: mental activities and the states of viscera organs are not known or unmeasurable and inflammations in the immune system are the ones to be inferred. Now, in this assessment scenario, in order to obtain the stable and consistent quantitative measures, we have to minimize the influences of mental activities and viscera organs. To fulfill this requirement, variabilities are best to be measured when the subject is in deep sleep or in a coherence state between respiration and heart rate where mental activities and viscera influences are purposely minimized.

HRV has been studied for a long time to reflect the states of ANS regulation [14, 18]. In clinical practice, HRV is usually evaluated using Holter device and software, without consideration of physical activities and other influences. This has resulted in inconsistences in various studies and limited the clinical applications of HRV. To quantitatively evaluate the physical activities and define the testing scenario, in case of using Holter device, a three-dimensional accelerometer sensor is used to detect and classify posture and activity into laying, sitting or standing, walking, or running. HRV indices are then calculated when any of those postures and activities keeps for more than 10 minutes [19].

The interaction between heartbeat and respiration is the well-known respiratory sinus arrhythmia (RSA). The wisdom of the body to maintain the homeostasis is achieved by synchronizing heartbeats with breathing and consequently to maximize the efficiency of the cardiopulmonary system in metabolic and circulation process. This equilibrium state is the result of resonance of the cardiopulmonary system. There are indices proposed to evaluate the degree of the resonance of the cardiopulmonary system. The most common used one is coherence measure (Coh), the cross power spectral density of the heart rate and respiration signals [20].

The resonance of the cardiopulmonary system represents the equilibrium of ANS regulation, where one reaches both physiological and psychological healthy state. Therefore, Coh can be used to compose numerical measures to visually represent one's health state, especially psychological health state, and then, variability-biofeedback training is used to help one to gain resonance state. A clinic trial was conducted in the University of Chinese Academy of Sciences (UCAS) Hospital to test the effectiveness of HRV biofeedback (HRVB) for pregnant women in managing anxiety and depression [21]. 20 pregnant women at last trimester (28–32$^{\text{th}}$ week) without pregnancy-induced hypertension and diabetes were randomly assigned to the HRVB group and the control group. Participants in the HRVB group practiced HRVB for 30 minutes per day, while participants in the control group did not. Following checks are conducted for all participants every two weeks: blood pressure (BP), fasting blood glucose (FBG), HRV of pregnant women (PHRV) and their fetuses (FRHV), and subjective assessment on pressure using Pregnancy Pressure Scale (PPS), depression using Edinburgh Postnatal Depression Scale (EPDS), and sleep quality using Pittsburgh Sleep Quality Index (PSQI). The clinical trial continued for subjects until they are in hospital for delivery. In the trial, the HRVB group has shown significant improvement over the control group with respect to blood pressure stability ($p > 0.05$), depression reduction ($p = 0.013$), and sleep quality improvement, while fetuses in the HRVB group has shown significant improvement with respect to HRV SDNN ($p < 0.01$) and LF spectrum power ($p < 0.01$).

HRV and BPV can be used as a noninvasive assessment tool for autonomic nervous system function, and reduced and/or abnormal HRV and BPV are associated with increased risk of mortality in cardiac patients. For both adults and children, increased blood pressure variability (BPV) appears to be directly related to sympathetic overactivity with increased risk of end-organ damage and cardiovascular events. Decreased HRV has been observed in adults and children with chronic kidney disease and is an independent predictor of mortality [22].

Autonomic dysfunctions are the most common non-motor symptoms of Parkinson's disease (PD) and often precede the motor symptoms of the disease. Clinical study has shown that HRV and BPV can be used as markers to indicate the treatment progress and stages of the disease [23].

A review of research literature [24] tells that affected central nervous system structures and implicated autonomic nervous system regulation coexist in Alzheimer's disease. Assessment of autonomic dysfunction can be used as an early marker of Alzheimer's disease and used for differential diagnosis among dementia subtypes.

4. Chronotropic Competence Indices in Graded Exercise Testing Scenario

Graded exercise tests, such as cardiopulmonary exercise test (CPX), have been used in clinical practice to test the exercise capability in terms of maximum oxygen metabolism [25]. In Dystasis family, CCI are designed to evaluate the capability of the ANS regulation of the cardiac system in response to exercise, where the subject does not necessarily reach the maximum exercise intensity.

Chronotropic incompetence (CI) is a terminology describing the status of attenuated heart rate response to exercises. CI has been studied for the last 50 years [26]. Typical CI-related measurements include the maximum heart rate and heart rate recovery after exercise. There have been a lot of research efforts to explore the usefulness of CI parameters in clinical applications, i.e., their diagnosis value of coronary artery [27], prognosis and management of heart failure [28, 29], diabetes [30, 31], and hypertension [32, 33]. Although CI is an independent predictor of major adverse cardiovascular events and overall mortality, the importance of CI is underestimated [34]; this may be in part due to multiple definitions, the confounding effects of aging and medications, and the need for formal exercise testing for definitive diagnosis.

We have formally defined CCI as part of Dystasis in a systematic way and in terms of ANS regulation capabilities and endowed CCI with clear physiological and clinical implications. CCI are defined as follows:

(1) Resting heart rate (HRrest) and resting blood pressure (BPrest): The resting heart rate and resting blood pressure are defined as the heart rate and blood pressure when a person is awake, in a neutrally temperate environment, and has not been subject to any recent exertion or stimulation, such as stress or surprise.

(2) Chronotropic rate (CR_{HR} and CR_{BP}): chronotropic rate represents the rate at which the heart rate and blood pressure increase as exercise intensity increases. It is measured as the amount of heart rate or blood pressure increase in response to every unit of metabolic equivalent (MET) exercise intensity increase. In practice, it can be measured and calculated as

$$\begin{aligned} CR_{HR} &= \frac{\left(HR_{stage} - HR_{rest}\right)}{\left(MET_{stage} - 1\right)}, \\ CR_{BP} &= \frac{\left(BP_{stage} - BP_{rest}\right)}{\left(MET_{stage} - 1\right)}. \end{aligned} \tag{2}$$

CR_{HR} is similar with the "Exercise HR" in EACPR/AHA Joint Scientific Statement [25]. It directly relates to sympathetic nerves activation and provides insight into chronotropic competence and cardiac response to exercise. It normally increases ~10 beats per MET. The chronotropic rate is an important parameter to provide personalized quantitative relation between HR and exercise intensity so that the target heart rate (THR) can be used to prescribe exercise intensity in exercise training. However, the chronotropic rate of a person may vary due to medication or rehab progress; it is recommended to measure the chronotropic rate promptly or monitor chronotropic rate changes in order to keep exercise prescription updated [35].

(3) Chronotropic limit (CL): chronotropic limit represents the maximal heart rate an individual can achieve without severe problems through exercise stress, as well as the blood pressure measured at the same time. It is measured as heart rate reserve and calculated as

$$CL = HRR = \frac{(HR_{max} - HR_{rest})}{(HR_{PredM} - HR_{rest})}, \tag{3}$$

where HR_{max} is the maximal heart rate one achieves during the exercise test and HR_{PredM} is the predicted maximal heart rate, usually calculated as $220 - age$. The maximal heart rate is usually obtained when reaching peak exercise, which can be identified during CPX testing. In this case, the normal value of CL is 0.8–1.3. However, when CPX testing or peak exercise is not achievable, then CL normal values are different for types of exercises. For example, in a 6-minute walking test, $CL = 0.4$ for a 60-year-old person should be considered normal. With a resting heart rate of 75 bpm, CR would be 10 beats per MET and the maximal heart rate would be 109 bpm with an exercise intensity of 4.4 MET.

(4) Chronotropic acceleration (CA): ANS requires certain time to adjust the heart rate and blood pressure to reach a new stable state or equilibrium when the exercise intensity increases to a new level in the graded exercise test. CA is defined as the time taken to reach new equilibrium after exercise intensity increases. CA is measured in seconds and represents the ability of the ANS regulation of the cardiac system in fulfilling metabolic needs.

(5) Chronotropic recovery at 1 minute after exercise ($HR_{recovery1}$ and $BP_{recovery1}$): it is defined as the reduction in the heart rate and blood pressure 1 minute after stopping exercise. The measurement of $HR_{recovery1}$ and $BP_{recovery1}$ requires the testee to try his best in the exercise, but not necessarily to reach one's maximum capacity. EACPR/AHA Joint Scientific Statement [25] considers that $HR_{recovery1}$ provides insight into speed of parasympathetic reactivation and that the normal value of $HR_{recovery1}$ should be > 12 beats. There have been a number of clinical studies on prognosis value of $HR_{recovery1}$. For example, Dhoble et al. [36] examined conventional cardiovascular risk factors and exercise test parameters in 6546 individuals (mean age 49 years, 58% men) between 1993 and 2003. A total of 285 patients died during the follow-up period. $HR_{recovery1} < 12$ beats were found independently associated with mortality ($P < 0.001$).

A clinical trial in cardiac rehabilitation was conducted in Jiangsu Provincial Hospital to evaluate the usability of CCI [37], which are measured by Cardiac Chronotropic Competence Testing (3CT), a device produced by SmartHealth Electronics Ltd. 61 participants were recruited, including patients of unilateral ischemic or hemorrhagic stroke within the previous 6 months with some voluntary movement and preserved cognitive function. Participates are randomly assigned to the rehab group (30) and control group (31). Each patient from both groups was evaluated at the beginning and after 3 months using both subjective/qualitative and objective/quantitative measures, namely, the International Classification of Functioning, Disability and Health (ICF), and chronotropic competence indices (CCI) and 6 minute walking test (6MWT). Patients in the control group were given personalized rehab advices after the baseline test. Patients in the rehab group were equipped with a Microsens rehab assistant for regular rehab exercise at home. Personalized exercise prescription based on CCI is downloaded into MicroSens rehab assistant, which consists of rehab app on a smartphone and a wearable device.

Comparison between control and rehab groups after 3 months of rehab training using the t-test shows that, through out the rehab training, all the four ICF measurements, namely, walking, doing house-hold work, interpersonal interactions, and muscle power, have significant improvement (p = 0.0070, 0.0209, 0.0089, and 0.0000, respectively). Consistently, after 3 months of rehab training, the rehab group is significantly better over the control group with respect to all three 3CT objective measures: 6-minute walking distance, chronotropic rate, and 1-minute heart rate recovery (p = 0.0445, 0.0121, and 0.0414, respectively).

5. BRS, SNA, and PNA in Orthostatic Testing Scenario

Estimation of BRS, SNA, and PNA is carried out in orthostatic testing scenario where the subject is requested to suddenly stand up from a sitting position. As a result, blood pools in the vessels of the legs for a longer period and less is returned to the heart, thereby leading to a reduced cardiac output and fall in blood pressure. In order to counteract these changes, the frequency of afferent impulses in the aortic and carotid sinus nerves is reduced, which leads to parasympathetic withdrawal and sympathetic activation. Here, the nerve activity will be referred to as the baroreflex firing rate or simply the firing rate. Sympathetic activation leads to a growing release of norepinephrine which contributes to restoration of BP by increasing HR, cardiac contractility, and vasoconstrictor tone. In addition, parasympathetic withdrawal leads to decreased

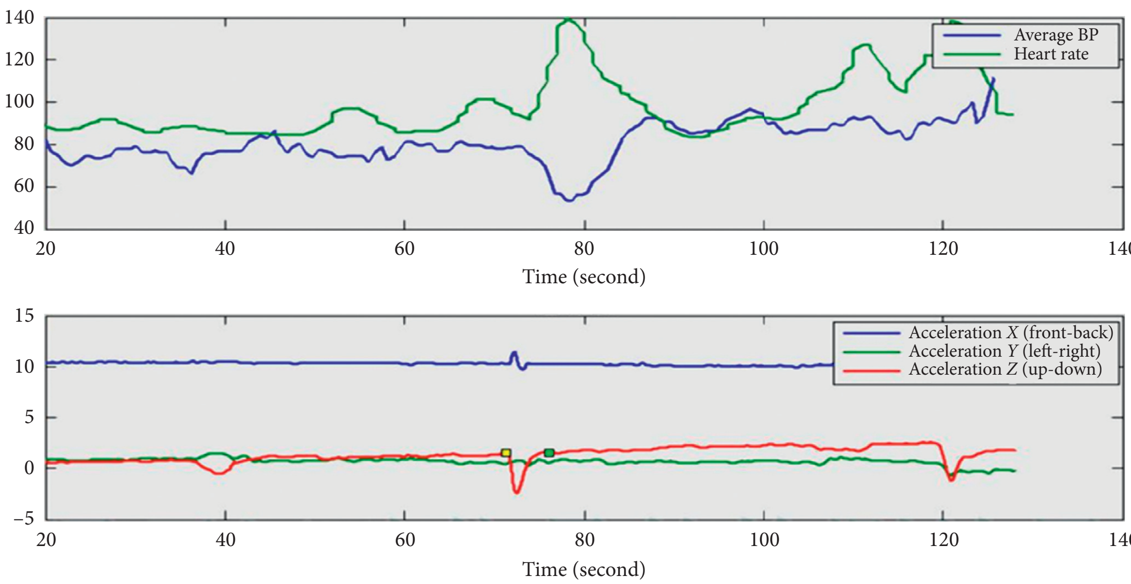

Figure 2: Curves of measured acceleration data (low), average blood pressure (up, blue), and heart rate (up, green). The stands up at the 47th second, when acceleration Z component (red) has a sudden drop, followed by average blood pressure fall and recovery and heart rate increase and recovery.

release of acetylcholine which also causes the increase of HR. This whole ANS regulation process can be described by a mathematical model [29, 38].

In the measurement, the subject wears a device which measures ECG, radial artery pulse wave and branchial artery pulse wave, and acceleration data to locate phases of the orthostatic posture. The orthostatic testing protocol is as follows:

(1) The subject wears the device and sits on a chair, with the upper body straight up until reaching a stable state of heart rate

(2) The subject stands up and keeps standing for 40 seconds

(3) The above process is repeated for three times

The device records all the data and sends the data to the computer wirelessly. The heart rate is calculated from ECG signal. The average blood pressure is estimated via pulse transmission time from radial artery pulse wave and branchial artery pulse wave with assumption that the physical properties of the blood vessel and the blood do not change within the measurement time. Figure 2 shows a sample of the measurement data.

The blood pressure change in the orthostatic test is maximized, and the mathematical model defining the ANS regulation of heart rate due to blood pressure changes can then be simplified as a small subgraph of the probability graphic model in Figure 1. Based on the mathematical model, using a series of blood pressure and heart rate data pairs obtained in the orthostatic testing, we can perform the following.

(i) For each BP and HR pair, the following is performed:

(a) BP is used to calculate the baroreflex firing rate

(b) With baroreflex firing rate, sympathetic and parasympathetic outflows are predicted

(c) Concentrations of noradrenaline and acetylcholine are computed as functions of the sympathetic and parasympathetic outflows

(d) Heart rate is computed as a function of these two chemical concentrations

(e) Computed HR is compared with the measured HR

(ii) For all BP and HR pairs, optimization for the minimizing error is performed between computed HR and measured HR to get curves of baroreflex firing rate and sympathetic and parasympathetic outflows. Figure 3 shows these curves for a healthy young person and a 50^{th} hypertension person. Other parameters, such as baroreflex sensitivity, can be derived from those curves and BP and HR data.

Noninvasive measurement of BRS, SNA, and PNA provides useful meanings to discover mechanisms that act to keep cerebral blood flow (CBF) constant, to understand immune system, for better management of metabolic syndrome and hypertension. The quantitative estimation of baroreflex sensitivity has been regarded as a synthetic index of neural regulation at the sinus atrial node, which has been shown to provide clinical and prognostic information in a variety of cardiovascular diseases, including myocardial infarction and heart failure [39]. Chronic hyperglycemia is the primary risk factor for the development of complications in diabetes mellitus (DM). Postprandial spikes in blood glucose, as well as hypoglycemic events, are blamed for increased cardiovascular events in DM. Glycemic variability (GV) includes both of these events. However, defining GV remains a challenge primarily due to the difficulty of measuring it [40]. A multicenter, prospective, open-label clinical trial including a total of 102 patients with type 2 diabetes [41] has found that GV was inversely related to BRS

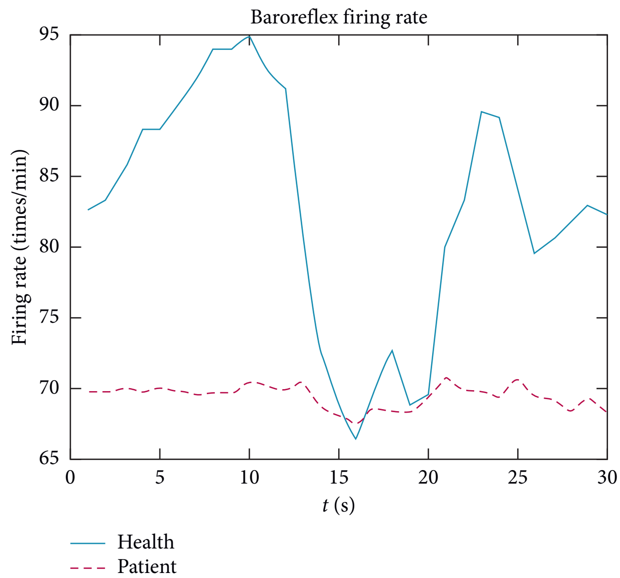

Figure 3: Baroreflex firing rate as a function of time. Results are shown from a healthy person (solid) and a hypertensive patient (dash).

independent of blood glucose levels in type 2 diabetic patients and that measurement of BRS may have the potential to predict CV events in consideration of GV.

6. Conclusion and Remarks

We have described a systematic method for the quantitative assessment of autonomic cardiac system regulation, named Dystatis. The fundamental part of Dystatis is a quantitative assessment methodology based on homeostatis and the probabilistic graphic model, where homeostatis explains ANS regulation while the probability graphic model formally defines the regulation process and provides quantitative assessment basis. As instances of Dystatis, indices and measurement methods for three well-designed scenarios are also described together with clinical applications: (1) HRV, BPV, and Synch in resting situation, (2) CCI in graded exercise testing, and (3) BRS, SNA, and PNA in orthostatic testing.

Numerous clinical research results have shown that the proposed method and indices for autonomic cardiac system regulation have great application potential in the prediction, prognosis, and rehabilitation of cardiovascular diseases, hypertension, diabetes, and other autonomic nerves-related areas. Further researches are being carried out to work with various research institutions and hospitals to conduct multicenter clinical research to investigate potential applications of the proposed methods in the prediction, prognosis, and rehabilitation of cardiovascular diseases, hypertension, diabetes, and other autonomic nerves-related problems.

Data Availability

The data used to support the findings of this study are available from the corresponding author upon request.

Conflicts of Interest

The authors declare that they have no conflicts of interest.

References

[1] A. Zygmunt and J. Stanczyk, “Methods of evaluation of autonomic nervous system function,” *Archives of Medical Science*, vol. 1, pp. 11–18, 2010.

[2] C. Heymans, “Reflexogenic areas of the cardiovascular system,” *Perspectives in Biology and Medicine*, vol. 3, no. 3, pp. 409–417, 1960.

[3] J. Axelrod, “Studies on sympathomimetic amines. II. The biotransformation and physiological disposition of d-amphetamine, d-p-hydroxyamphetamine and d-methamphetamine,” *Journal of Pharmacology and Experimental Therapeutics*, vol. 110, pp. 315–326, 1954.

[4] U.S. Von Euler, “Sympathin in adrenergic nerve fibres,” *Journal of Physiology*, vol. 105, p. 26, 1946.

[5] C. J. Del and B. Katz, “Quantal components of the end-plate potential,” *Journal of Physiology*, vol. 124, pp. 560–573, 1954.

[6] F. M. Abboud, “In search of autonomic balance: the good, the bad, and the ugly,” *American Journal of Physiology-Regulatory, Integrative and Comparative Physiology*, vol. 298, no. 6, pp. R1449–R1467, 2010.

[7] H. Modell, W. Cliff, J. Michael, J. Mcfarland, M. P. Wenderoth, and A. Wright, “A physiologist’s view of homeostasis,” *Advances in Physiology Education*, vol. 39, no. 4, pp. 259–266, 2015.

[8] J. K. Phillips, “Autonomic dysfunction in heart failure and renal disease,” *Frontiers in Physiology*, vol. 3, p. 219, 2012.

[9] F. M. Abboud and M. V. Singh, “Autonomic regulation of the immune system in cardiovascular diseases,” *Advances in Physiology Education*, vol. 41, no. 4, pp. 578–593, 2017.

[10] C. K. Willie, Y.-C. Tzeng, J. A. Fisher, and P. N. Ainslie, “Integrative regulation of human brain blood flow,” *Journal of Physiology*, vol. 592, no. 5, pp. 841–859, 2014.

[11] N. Tentolouris, G. Argyrakopoulou, and N. Katsilambros, “Perturbed autonomic nervous system function in metabolic syndrome,” *Neuromolecular Medicine*, vol. 10, no. 3, pp. 169–178, 2008.

[12] G. Mancia and G. Grassi, “The autonomic nervous system and hypertension,” *Circulation Research*, vol. 114, no. 11, pp. 1804–1814, 2014.

[13] G. Grassi and M. Esler, “How to assess sympathetic activity in humans,” *Journal of Hypertension*, vol. 17, no. 6, pp. 719–734, 1999.

[14] G. Ernst, “Heart-rate variability-more than heart beats?,” *Frontiers in Public Health*, vol. 5, p. 240, 2017.

[15] W. Jänig, “Sympathetic nervous system and inflammation: a conceptual view,” *Autonomic Neuroscience*, vol. 182, pp. 4–14, 2014.

[16] D. Koller and N. Friedman, *Probabilistic Graphical Models: Principles and Techniques - Adaptive Computation and Machine Learning*, MIT Press, Cambridge, MA, USA, 2009.

[17] S. W. Porges, “The polyvagal theory: new insights into adaptive reactions of the autonomic nervous system,” *Cleveland Clinic Journal of Medicine*, vol. 76, no. 2, pp. S86–S90, 2009.

[18] M. C. Rollin and S. Fred, “Heart rate variability: new perspectives on physiological mechanisms, assessment of self-regulatory capacity, and health risk,” *Global Advances in Health & Medicine*, vol. 4, pp. 46–61, 2015.

[19] L. Ji, J. Wu, Y. Yang, S. Wang, and A. Li, “Activity-aware HRV analysis,” in *Proceedings of the IEEE International Conference*

on Systems, Man, and Cybernetics, pp. 1151–1156, Anchorage, AK, USA, October 2011.

[20] Z. Chen, E. N. Brown, and R. Barbieri, "Assessment of autonomic control and respiratory sinus arrhythmia using point process models of human heart beat dynamics," *IEEE Transactions on Biomedical Engineering*, vol. 56, pp. 1791–1802, 2009.

[21] D. J. Z. H. S. Zhao, "An exploratory pilot study on the effects of HRV biofeedback on pregnant women and fetuses," in *Proceedings of the International Symposium on Computer, Electronics, Electrical and Communication Engineering (CEECE 2018), Thaliand*, 2018.

[22] G.-M. Barletta, J. Flynn, M. Mitsnefes et al., "Heart rate and blood pressure variability in children with chronic kidney disease: a report from the CKiD study," *Pediatric Nephrology*, vol. 29, no. 6, pp. 1059–1065, 2014.

[23] A. Furgała, A. Górecka-Mazur, U. Fiszer et al., "[Evaluation of heart rate and blood pressure variability in Parkinson's disease patients after bilateral subthalamic deep brain stimulation]," *Przegląd Lekarski*, vol. 72, p. 246, 2015.

[24] G. D. Femminella, G. Rengo, K. Komici et al., "Autonomic dysfunction in Alzheimer's disease: tools for assessment and review of the literature," *Journal of Alzheimer's Disease*, vol. 42, no. 2, pp. 369–377, 2014.

[25] M. Guazzi, V. Adams, V. Conraads et al., "Clinical recommendations for cardiopulmonary exercise testing data assessment in specific patient populations," *Circulation*, vol. 126, no. 18, pp. 2261–2274, 2012.

[26] P. M. Okin, M. S. Lauer, and P. Kligfield, "Chronotropic response to exercise," *Circulation*, vol. 94, no. 12, pp. 3226–3231, 1996.

[27] L. Luo, S. P. Zhao, Y. Cao, H. J. Ye, and Q. H. Li, "[Diagnostic value of chronotropic incompetence in coronary heart disease]," *Journal of Central South University*, vol. 32, p. 309, 2007.

[28] D. A. Klein, D. H. Katz, L. Beussink-Nelson, C. L. Sanchez, T. A. Strzelczyk, and S. J. Shah, "Association of chronic kidney disease with chronotropic incompetence in heart failure with preserved ejection fraction," *American Journal of Cardiology*, vol. 116, no. 7, pp. 1093–1100, 2015.

[29] A. Pandey, A. Parashar, D. J. Kumbhani et al., "Exercise training in patients with heart failure and preserved ejection fraction," *Circulation: Heart Failure*, vol. 8, no. 1, pp. 33–40, 2015.

[30] T. Yamada, T. Yoshitama, K. Makino, T. Lee, and F. Saeki, "Heart rate recovery after exercise is a predictor of silent myocardial ischemia in patients with type 2 diabetes," *Diabetes Care*, vol. 34, no. 3, pp. 724–726, 2011.

[31] S. Y. Jae, S. Kurl, J. A. Laukkanen et al., "Exercise heart rate reserve and recovery as predictors of incident type 2 diabetes," *American Journal of Medicine*, vol. 129, pp. 536.e7–536.e12, 2016.

[32] K. Shin, K. Shin, and S. Hong, "Heart rate recovery and chronotropic incompetence in patients with pre-hypertension," *Minerva Medica*, vol. 106, pp. 87–94, 2015.

[33] E. Aneni, L. L. Roberson, S. Shaharyar et al., "Delayed heart rate recovery is strongly associated with early and late-stage prehypertension during exercise stress testing," *American Journal of Hypertension*, vol. 27, no. 4, pp. 514–521, 2014.

[34] P. H. Brubaker and D. W. Kitzman, "Chronotropic incompetence," *Circulation*, vol. 123, no. 9, pp. 1010–1020, 2011.

[35] B. Ferguson, "ACSM's guidelines for exercise testing and prescription," *Journal of the Canadian Chiropractic Association*, vol. 58, p. 328, 2014.

[36] A. Dhoble, B. D. Lahr, T. G. Allison, and S. L. Kopecky, "Cardiopulmonary fitness and heart rate recovery as predictors of mortality in a referral population," *Journal of the American Heart Association*, vol. 3, no. 2, article e000559, 2014.

[37] J. Wu, J. Li, A. Seely et al., "Chronotropic competence indices extracted from wearable sensors for cardiovascular diseases management," *Sensors*, vol. 17, no. 11, p. 2441, 2017.

[38] L. Wang, Z. Huang, J. Wu, Y. Meng, and R. Ding, "A model-based method to evaluate autonomic regulation of cardiovascular system," in *Proceedings of the IEEE International Conference on Wearable and Implantable Body Sensor Networks*, pp. 1–6, USA, 2015.

[39] M. T. La Rovere, G. D. Pinna, R. Maestri, and P. Sleight, "Clinical value of baroreflex sensitivity," *Netherlands Heart Journal*, vol. 21, no. 2, pp. 61–63, 2013.

[40] S. Suh and J. H. Kim, "Glycemic variability: how do we measure it and why is it important?," *Diabetes & Metabolism Journal*, vol. 39, no. 4, p. 273, 2015.

[41] D. Matsutani, M. Sakamoto, H. Iuchi et al., "Glycemic variability in continuous glucose monitoring is inversely associated with baroreflex sensitivity in type 2 diabetes: a preliminary report," *Cardiovascular Diabetology*, vol. 17, p. 36, 2018.

Hindawi
Journal of Healthcare Engineering
Volume 2019, Article ID 2658675, 14 pages
https://doi.org/10.1155/2019/2658675

Research Article

Estimation of Breathing Rate with Confidence Interval Using Single-Channel CW Radar

I. Nejadgholi,[1] H. Sadreazami ,[1] Z. Baird,[2] S. Rajan,[2] and M. Bolic[1]

[1]*School of Electrical Engineering and Computer Science, University of Ottawa, Ottawa, ON, Canada*
[2]*Department of Systems and Computer Engineering, Carleton University, Ottawa, ON, Canada*

Correspondence should be addressed to H. Sadreazami; hsadreaz@uottawa.ca

Received 16 November 2018; Revised 6 February 2019; Accepted 5 March 2019; Published 28 March 2019

Guest Editor: Jilong Kuang

Breathing rate monitoring using continuous wave (CW) radar has gained much attention due to its contact-less nature and privacy-friendly characteristic. In this work, using a single-channel CW radar, a breathing rate estimation method is proposed that deals with system nonlinearity of a single-channel CW radar and realizes a reliable breathing rate estimate by including confidence intervals. To this end, time-varying dominant Doppler frequency of radar signal, in the range of breathing rate, is extracted in time-frequency domain. It is shown through simulation and mathematical modeling that the average of the dominant Doppler frequencies over time provides an estimation of breathing rate. However, this frequency is affected by noise components and random body movements over time. To address this issue, the sum of these unwanted components is extracted in time-frequency domain, and from their surrogate versions, bootstrap resamples of the measured signal are obtained. Accordingly, a 95% confidence interval is calculated for breathing rate estimation using the bootstrap approach. The proposed method is validated in three different postures including lying down, sitting, and standing, with or without random body movements. The results show that using the proposed algorithm, estimation of breathing rate is feasible using single-channel CW radar. It is also shown that even in presence of random body movements, average of absolute error of estimation for all three postures is 1.88 breath per minute, which represents 66% improvement as compared to the Fourier transform-based approach.

1. Introduction

Breathing rate is one of the four vital signs. Breathing rates may increase with fever, stress, or some medical conditions. Prolonged increased breathing rate is a cause of concern; hence, it is important to measure breathing rate. Normal breathing rates for an adult person at rest ranges from 12 to 16 breaths per minute.

In order to measure breathing rate, one may use contact-based method such as respiratory inductive plethysmography (RIP) bands. Such bands are used for sleep tests despite the discomfort to the subjects. There are several instances where such a band cannot be used. For instance, in the case of burn victims, it is not possible to use a band. In emergency departments, when patients arrive, it may not be possible to use a band to estimate breathing rate. Remote measurements are preferred in such cases. In senior's home, it is preferable to monitor breathing without the need to wear devices. In addition, correctional institutions are looking to adopt a non-obtrusive method for monitoring the vital signs of inmates, especially because it is a privacy-friendly technology compared to cameras. In addition, depending on the frequencies used for radars, it is possible to obtain both heart rate and breathing rate using a single sensor which may not be possible with RIP.

Radar has recently attracted much attention as a promising device for breathing rate monitoring, mainly because of its contact-less, privacy-friendly, and relatively safe properties [1–3]. Video cameras, as an alternative choice, have been used for contact-less monitoring of vital signs. However, cameras invade privacy and their performance is highly affected by the amount of light in the monitored space [4, 5] and pose of the subjects.

Continuous wave (CW) radar systems have widely been used for vital sign monitoring due to their low power consumption and simple radio architecture [6, 7]. This radar has also been used to see through-wall a human skeletal figure [8] and localize a small number of colocated people [9]. In such radar systems, a single-frequency signal is transmitted and signals reflected off the subjects are received. The received signal is modulated by the movements of the chest based on the Doppler principle. Most of these works have focused on the two-channel CW radar for vital sign monitoring with less attention to the effect of random body movements. In the proposed method, we employ a single-channel CW radar to estimate the vital signs, where the subjects are moving their body parts randomly.

When CW radar is used, the information of micro-movements of chest and abdomen are concealed in the phase of the received signal. For small movements, i.e., the amplitude of displacement is much smaller than the wavelength of transmitted signal, the signal can be approximated by its phase, referred to as linear approximation [10]. On the other hand, in the case of larger displacements of chest and abdomen which depend on the anatomy of the subject and the type of breathing and posture, the linear approximation does not hold anymore especially when the wavelength of radar is small (<2 cm). In this case, multiple harmonics of breathing as well as intermodulations between heart rate and breathing rate are produced [11], which affect the accuracy of breathing rate estimation obtained through Fourier analysis. One possible solution to address the nonlinearity of a single-channel Doppler radar is by using a quadrature radar architecture. Since the vital sign signal is a low-frequency signal, the two output channels of the quadrature radar can be used for either complex signal demodulation [12] or arctangent demodulation [13] to calculate the total Doppler phase shift. It is known that the Doppler phase shift is directly proportional to the displacements of chest. Besides dealing with nonlinearity of the signal, integration of two channels in the architecture of CW radar can offer solutions to several challenges of vital sign monitoring such as null point effect and effect of random body movements [14–17].

In this work, breathing rate is estimated by using a single-channel CW radar and applying time-frequency analysis instead of Fourier transform. The proposed method is evaluated in a real situation, where nonlinearity, null point effect, and random body movements are considered. Multiple subjects are monitored in different postures, namely, lying, sitting, and standing, at different distances from the radar with or without random movements of body. There have been few works on cancellation of random movements of body. In [18], an antiphase signal generator was used to reduce the effect of random body movements. In [13], a phase-diversity Doppler radar was introduced that utilized three antennas, one for transmitting and the other two for receiving. The receiving antennas were isolated by half of a wavelength. In [19], the center estimation algorithm was proposed to resolve the issue of random body movements. Self-injection-locked radar was proposed in [20] to cancel body movements. In [21], empirical mode decomposition was applied to cancel only the sensor movement and not the random body movements. However, all these works used both in-phase and quadrature channels and their solutions generally resulted in an increase in system complexity, cost, and power consumption. It should be noted that so far, the estimation of vital signs, where the subject is moving their body parts randomly, has not been considered with simple-structured single-channel CW radar.

Velocity of movements of chest and abdomen changes periodically over time due to breathing. This time-varying velocity translates into time-varying Doppler frequency of reflections received by the single-channel CW radar. However, other movements of the subject can contribute to frequency modulations around the main Doppler shift that are commonly referred as micro-Doppler modulations [22]. These micro-Doppler signatures in time-frequency domain have already been used to perform classification [23, 24]. This idea has also been used to estimate vital signs during walking [25].

To estimate the breathing rate, in this work, a sequence of dominant frequencies of the signal over time in the range of breathing is extracted and used to estimate the breathing rate. The bootstrap resampling method is used to support the estimation with a confidence interval, since we are dealing with a single-channel CW radar signal in which extracted micro-Doppler shifts may be affected by movements of body and null point effect.

The paper is organized as follows. Section 2 presents the model of reflected radar signal from a human subject using a single-channel CW radar and presents the challenges of estimating breathing rate using Fourier transform. Section 3 presents the proposed estimation method and also discusses the bootstrap resampling method used to estimate confidence interval of breathing rate. Section 4 presents the experimental setup and the data collection procedure. Section 5 presents a discussion of the results. Finally, Section 6 concludes the paper.

2. Modeling and Simulation of Single-Channel Radar Signal

During our experiment, in order to have the entire room covered, the radar is mounted on the wall. Figure 1 shows a scenario in which a stationary person is in front of the radar. The transmitting and receiving antennas are colocated. The transmitter transmits a radar signal that is a continuous wave which is intercepted by the subject. Movements of chest, abdomen, and heart cause Doppler shift in the frequency of the returned radar signal. At the receiver, the transmitted signal is delayed and correlated with the received signal. A low-pass filter is then applied to demodulate and filter out the carrier frequency of transmitted continuous wave. The baseband radar signal, $s(t)$, can be written as [10]

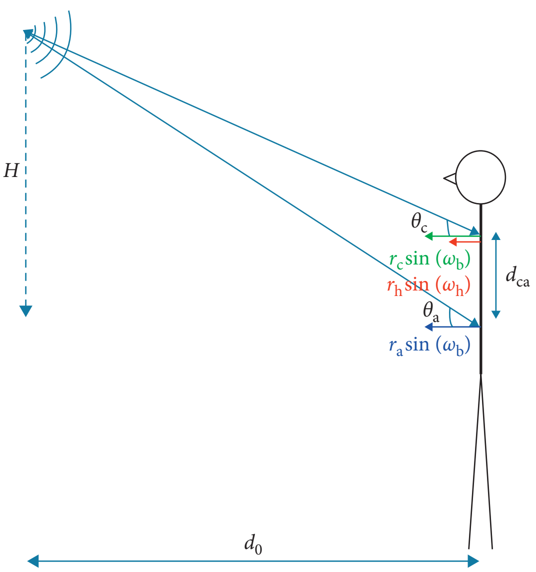

Figure 1: A subject is placed in front of the radar. Chest, abdomen, and heart move periodically.

$$\begin{aligned} s(t) &= V_0 + K\cos\left(\frac{4\pi}{\lambda}\left(d(t) + d_N(t)\right)\right) + w(t), \\ d(t) &= d_0\cos(\theta_c) + d_C(t) + d_0\cos(\theta_a) + d_A(t) + d_H(t), \\ d_C(t) + d_A(t) &= \left(r_c\cos(\theta_c) + r_a\cos(\theta_a)\right) \times \sin(\omega_b t + \phi_{0b}), \\ d_H(t) &= r_h\cos(\theta_c) \times \sin(\omega_h t + \phi_{0h}), \end{aligned} \tag{1}$$

where V_0 is the DC voltage, K is the gain of the radar, and $d(t)$ is the distance of the subject from the radar at time t. Wavelength of the CW radar is $\lambda = C/f_c$, where f_c is the frequency of transmitted signal and C is the speed of light. In (1), $d_C(t)$, $d_A(t)$, and $d_H(t)$ represent the periodic displacements of chest, abdomen, and heart, respectively. $d_N(t)$ denotes the random body movements that appear as phase noise in the received radar signal. r_c, r_a, and r_h are the amplitude of the displacement of chest, abdomen, and heart, ω_b and ω_h are the angular frequencies of breathing and heart beat, respectively. Also, ϕ_{0b} and ϕ_{0h} are the initial phase of periodic movements of breathing and heart at $t = 0$. For the sake of simplicity, it is assumed that abdomen and chest are moving with the same rate and initial phase as mentioned in [26]. In addition, the white noise, $w(t)$, is added to the received signal and (1) is written in terms of Bessel functions as described in the following equation:

$$\begin{aligned} s(t) = V_0 + K \times \mathrm{Re}\Bigg[& e^{(4\pi/\lambda)(d_0 + d_N(t))} \sum_{n=-\infty}^{\infty} J_n\left(\frac{4\pi}{\lambda}\left(r_c\cos(\theta_c)\right.\right. \\ & \left.\left. + r_a\cos(\theta_a)\right)\right) e^{in(\omega_b t + \phi_b)} \\ & \cdot \sum_{m=-\infty}^{\infty} J_m\left(\frac{4\pi}{\lambda}\left(r_h\cos(\theta_c)\right)\right) e^{in(\omega_h t + \phi_h)}\Bigg] + w(t), \end{aligned} \tag{2}$$

where $J_n(r)$ is a Bessel function of the first kind and $e^{ir\times\sin(\phi)} = \sum_{n=-\infty}^{\infty} J_n(r) e^{in\phi}$ with $J_n(r) = (-1)^n J_{-n}(r)$. From (2), it can be seen that the received radar signal is composed of multiple harmonics of breathing and heart rate as well as intermodulations of these harmonics with amplitude of $J_n(4\pi/\lambda(r_c\cos(\theta_c) + r_a\cos(\theta_a))) \times J_m(4\pi/\lambda r_h\cos(\theta_c))$ and angular frequencies of $(n\omega_b + m\omega_h)$. Depending on the sum of maximum displacements of chest and abdomen $r_c + r_a$, and the displacement of heart r_h, after some n and m, the terms in (2) will become negligible.

In order to estimate the breathing rate from the received radar signal, the frequency where the magnitude of spectrum is maximum is found within the range of normal breathing. According to (2), the amplitude of this harmonic is $J_1(4\pi/\lambda(r_c\cos(\theta_c) + r_a\cos(\theta_a))) \times J_0(4\pi/\lambda r_h\cos(\theta_c))$, when $n = 1$ and $m = 0$ for fundamental frequency. It is noted that the amount of displacement may change the amplitude of the Bessel coefficients and number of non-negligible coefficients.

According to [27], movements of chest and abdomen (r_a and r_c in (1)) can change in the range of a few millimeters in quiet breathing to a few centimeters in deep breathing, depending on the age, sex, and posture of the subject under study. Figure 2 shows how significant harmonics are affected by the amount of displacement of abdomen. The same effect can also be seen through different amount of movements of the chest. To depict Figure 2, (1) is used to simulate breathing movements, $d_C(t) + d_A(t)$, and radar signal, $s(t)$, where each row shows a different scenario. In all the cases, the operating frequency of the radar is $f_C = 24\,\mathrm{GHz}$, $r_h = 0.1\,\mathrm{mm}$, heart rate is 72 beats per minute and breathing rate is 18 bpm, the horizontal distance of the subject from the radar is $d_0 = 2.5\,\mathrm{m}$, the distance between chest and abdomen is $d_{ca} = 0.5\,\mathrm{m}$, and the height of radar receiver (in Figure 1) is $H = 2\,\mathrm{m}$. In addition, the maximum displacement of chest is $r_c = 1\,\mathrm{mm}$ and maximum displacement of abdomen is 1 mm, 5 mm, 20 mm, and 50 mm from top to the bottom, respectively. White noise is added to the received radar signal with signal-to-noise ratio (SNR) of 20 dB. As observed from the right column of this figure, the strength of breathing harmonic at breathing rate is $((\omega_b \times 60)/2\pi)$ bpm and also the other significant harmonics are affected as the displacement of abdomen changes. Further investigation shows that the estimation (rate of the strongest peak at the range of breathing) can significantly be impacted by the noise.

Figure 3 shows the results of a simulation when Fourier transform is used for estimation, the breathing rate estimation is sensitive to the distance of the subject from radar d_0 and the displacement of the chest. In this simulation, for two arbitrary distances, 100 noisy versions of the radar signal are generated using (1) and values given in Table 1. The frequency of strongest peak in the range of breathing (6 to 24 bpm) is taken as the estimate of breathing. For each distance (d_0), the average of estimations $\mu_{\mathrm{rate}_{\mathrm{est}}}$ and 95% standard interval of these estimations $[\mu_{\mathrm{rate}_{\mathrm{est}}} - Z_\alpha\sigma_{\mathrm{rate}_{\mathrm{est}}}, \mu_{\mathrm{rate}_{\mathrm{est}}} + Z_\alpha\sigma_{\mathrm{rate}_{\mathrm{est}}}]$ are shown in Figure 3 for a range of displacements of abdomen, where Z_α is the Z-score of

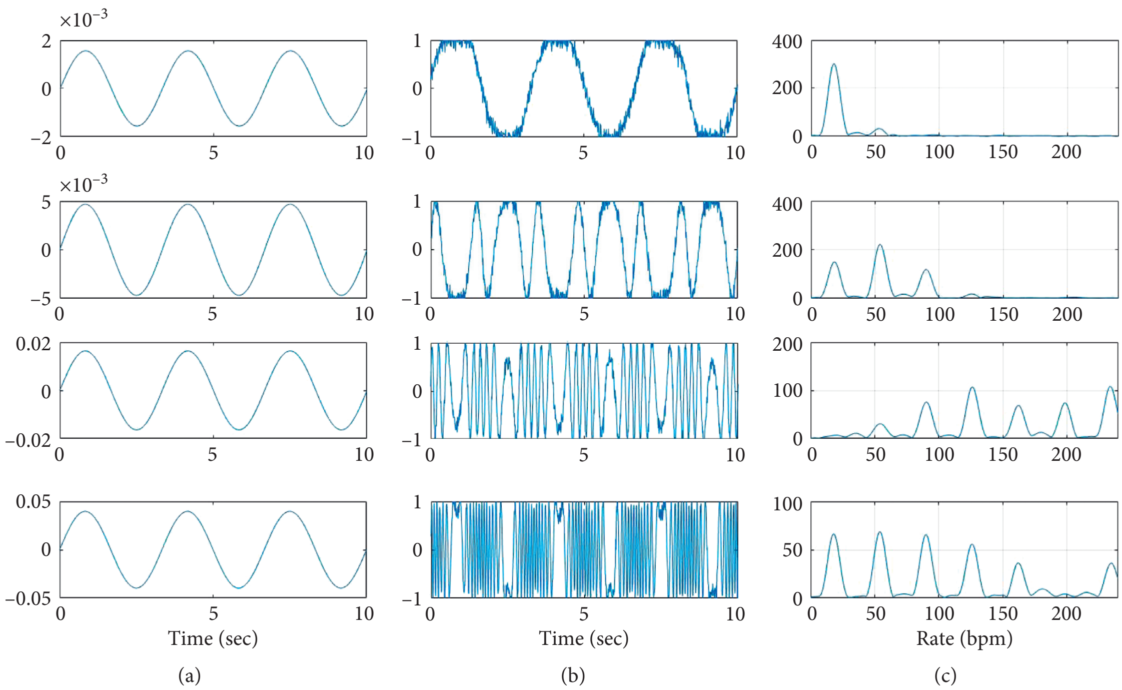

FIGURE 2: Effect of displacement of abdomen on the strength of the breathing harmonic and the other nonnegligible harmonics in simulated radar signal. Values used for simulation are shown in Table 1, r_a = 1 mm, 5 mm, 20 mm, 50 mm from top to the bottom, respectively. (a) Breathing signal. (b) Radar signal. (c) Chirp transform of radar.

$\alpha = 0.05$. It can be seen from the figure that the width of standard interval of estimation highly depends on the displacement of body due to breathing and the distance of the subject from the radar. This shows that these two examples are selected to show that the estimation of breathing frequency using Fourier transform with a single-channel CW radar may be problematic. It is also noted that in Figure 3, only additive noise is considered, yet random movements of body may affect this estimation, even more dramatically.

The most common approach used in estimating breathing rate is the Fourier transform, which is mostly suitable to analyze stationary signals having the same frequency content over time. Most of the literature focuses only on choosing the peak of the spectrum within the breathing frequency range using the standard discrete Fourier transform. However, when random movements are present, peaks due to breathing frequency may not be prominent, and hence estimation may either be biased or totally wrong. In this work, modifications to the Fourier transform such as windowed Fourier transform, chirp Fourier transform, and micro-Doppler series acquired from the radar return are employed to estimate the changing frequency of signal over time.

3. Methods and Materials

3.1. Estimation of Breathing Rate Using Time-Frequency Analysis. The signal model described in (1) represents a nonstationary signal that can be analyzed in time-frequency domain by applying Fourier transform in sufficiently narrow time windows, where the signal may be assumed stationary [28]. For a given $s(t)$, the windowed Fourier transform (WFT), $S(f,t)$ is constructed as follows:

$$S(f,t) = \frac{1}{2\pi}\int_0^{\infty} \hat{s}(u)\hat{g}(f-u)e^{iut}du, \tag{3}$$

where $\hat{s}(u)$ is Fourier transform of $s(t)$ and $\hat{g}(u)$ is Fourier transform of the Gaussian window defined as

$$g(t) = \frac{1}{\sqrt{2\pi}f_0} e^{\left(-(t/f_0)^2\right)/2}, \tag{4}$$

where f_0 is a resolution parameter that identifies the trade-off between time and frequency resolutions. In order to estimate the changing frequency of signal over time, for each time sample t_n, the frequency in which amplitude of $S(f,t_n)$ is maximum is found, i.e., dominant frequency at time t_n. In this work, the sequence of these frequencies $\nu(t)$ is extracted from the radar signal over time. It is noted that when $\nu(t)$ is extracted from the range of normal breathing, it represents micro-Doppler frequency of the signal over time and is related to time-varying velocity of chest and abdomen.

At this stage, the phase of $s(t)$ in the range of breathing frequency is calculated by setting $n = 1$ and $m = 0$ in (2) and is written as

$$\Phi_{\mathrm{s,Breathing}}(t) = \frac{4\pi}{\lambda}\left(d_0 + d_{\mathrm{N,Breathing}}(t)\right) + \omega_{\mathrm{b}}t + \phi_{0\mathrm{b}}, \tag{5}$$

where $d_{\mathrm{N,Breathing}}$ represents all random body movements having the same velocity unlike the breathing-related Doppler and thus is detected in the range of the breathing frequency. By definition, $\nu(t) = (\Phi'(t))/2\pi$ [28], where $\Phi'(t)$ is the phase derivative of $s(t)$ with respect to time t.

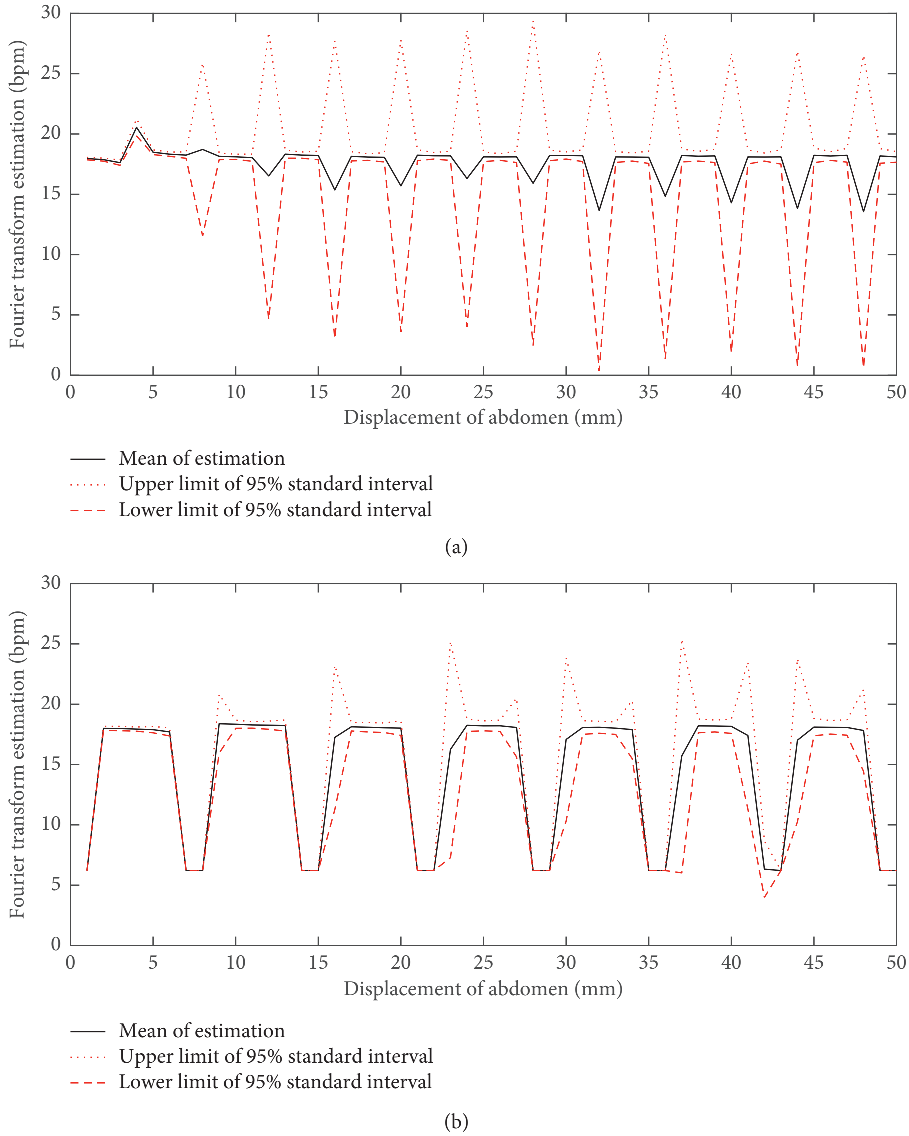

FIGURE 3: Estimated breathing rates vs displacement of the abdomen r_a. Sensitivity of the estimated breathing rates to displacement of abdomen and distance of the subject from radar is shown, when Fourier transform of the signal is used to estimate breathing rate from noisy simulated signals (parameters are given in Table 1). (a) $d_0 = 2.5$ (m). (b) $d_0 = 1$ m.

TABLE 1: Values used for simulation in Figures 2 and 3. It is noted that bpm stands for breath per minute.

Variable	H (m)	d_0 (m)	Breathing rate (bpm)	Heart rate (beat/minute)	r_c (mm)	r_h (mm)	r_a (mm)	d_{ac} (m)	λ (mm)
Value in Figure 2	2	2.5	18	72	1	0.1	(1, 5, 20, 50)	0.5	12.5
Value in Figure 3	2	2.5	18	72	1	0.1	(1–50)	0.5	12.5

The dominant frequency of $s(t)$ in the range of breathing can then be written as

$$\nu_{s,\text{Breathing}}(t) = \frac{4\pi}{\lambda} d'_{\text{N,Breathing}}(t) + f_b, \qquad (6)$$

where $d'_{\text{N,Breathing}}(t)$ denotes the speed at which the random body movements occur. Since $4\pi/\lambda$ is about 1000 for the radar in our experiments, very slow movements of body parts may give rise to high Doppler frequencies and thus may not be detected as a strong harmonic in the range of breathing. In view of this, $\nu(t)$ is assumed to be a linear combination of breathing rate and low-frequency harmonics of noise and random movements, and f_b can be estimated via calculating the mean of $\nu(t)$ over a specified time window of radar signal.

Figure 4 shows the micro-Doppler sequence extracted for the simulated radar signals shown in Figure 2. In simulations, d_N is not included assuming that random body movement is too slow to be detected at low frequencies of breathing range. Yet, additive noise $w(t)$ is considered.

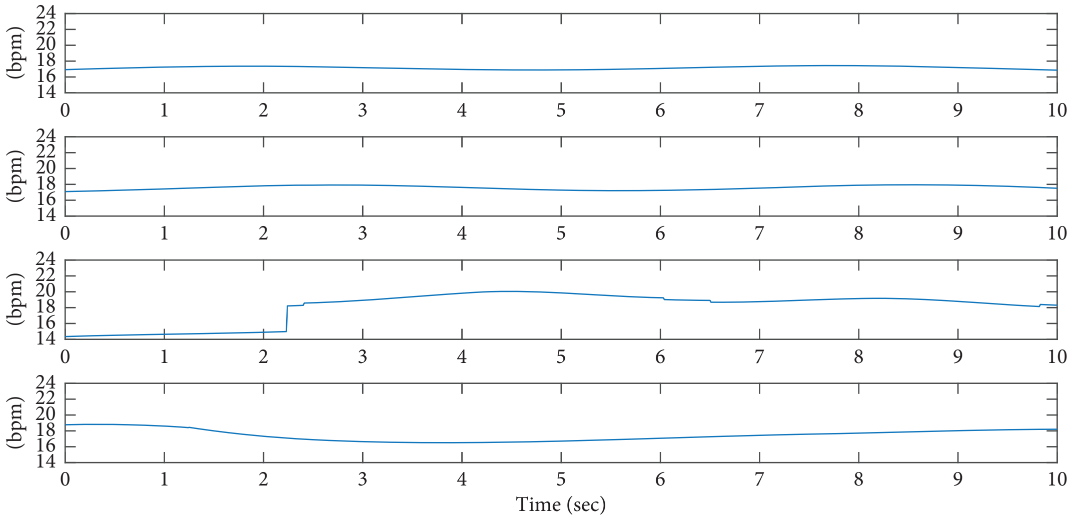

Figure 4: Micro-Doppler sequence extracted for simulated radar signal shown in Figure 2.

From this figure, the average and standard deviation of the extracted sequences are found to be 17.15 ± 0.16 bpm, 17.60 ± 0.26 bpm, 17.23 ± 2.39 bpm, and 17.41 ± 0.7 bpm, from top to bottom, respectively. However, the dominant frequencies in the range of breathing in frequency domain (calculated from right column of Figure 2) are 17.81 bpm, 18.28 bpm, 6.56 bpm, and 17.81 bpm, respectively. The actual breathing rate for all these simulated signals is 18 bpm. These estimations indicate that the average of micro-Doppler sequence is a more accurate way of breathing rate estimation using a single-channel CW radar. In addition, it is observed from this figure that for the third simulated signal, where $r_a + r_C = 21$ mm, the estimation in frequency domain is inaccurate since the harmonic of breathing is very weak. In this case, the standard deviation of the extracted micro-Doppler sequence is larger than the other cases. Thus, the standard deviation of the extracted micro-Doppler is used to calculate the confidence interval of estimation as a measure of confidence of the estimation in Section 3.3.

3.2. Constructing Bootstrap Resamples. It is noted that we are only interested in the dominant frequency at the range of breathing. However, estimation of this frequency is affected by random body movements and intermodulations amongst breathing frequency, heart rate and other frequencies related to body movements. The contributions due to body movements can be estimated via constructing the breathing signal based on the estimated breathing rate, subtracting it from the original radar signal and calculating the residual.

In order to examine how noise and intermodulations affect the estimation of micro-Doppler frequency, the bootstrap resampling method is employed. The bootstrap resampling was first introduced in [29] and has been modified and used in several applications since then. For instance, in [30], bootstrap has been used for confidence interval estimation using percentile-t method. It should be noted that the bootstrap method estimates the residuals and resamples it many times to build multiple noisy versions of the measured signal and calculates the confidence interval for each estimated parameter by assessing how noise distribution can affect the estimated parameter [31–33].

In our experiments, random body movements and intermodulations are hidden in the phase of the residuals. Thus, in order to make the bootstrap method resamples, the residuals are first calculated and the phase of the residuals is randomized to build multiple versions of possible random intermodulations and body movements. These noisy versions of residuals are referred as "surrogates" and have been introduced in order to build noisy versions of a signal with the same energy and frequency spectrum [34].

In order to calculate the residuals, for each time sample t, the frequency associated with maximum amplitude of $S(f, t)$ is found, i.e., micro-Doppler frequency $\nu(t)$ at time t. The average of $\nu(t)$ is taken as the estimate of breathing as described in Section 3.1. In order to reconstruct the breathing component in the time domain, the phase and amplitude of $S(\nu(t), t)$ are obtained. The reconstructed signal is subtracted from the original one, where the remainder (residual) is related to radar reflections from other parts of body or signals related to intermodulations of breathing and heart harmonics. Accordingly, a bootstrap resample of the radar signal is built through reconstructing the residuals with randomized phase and adding them to the breathing component extracted from the signal.

In order to estimate the bootstrap statistics from the constructed bootstrap samples, micro-Doppler frequency of each bootstrap resample is estimated and Student's t_{score} is calculated (described in Section 3.3), with respect to the estimation calculated from the original signal [33]. In order to calculate micro-Doppler frequencies, WFT uses multiple windows of signal similar to the block bootstrap method [35–37]. WFT uses overlapping blocks of the signal with the same length and is desired for block bootstrap for time series as it results in lower variance in estimators [38]. In view of this, in this work, a double-loop bootstrap method is used in order to generate bootstrap resamples and provide bootstrap statistics with higher accuracies [39].

3.3. Estimation of Confidence Interval. In the following, different steps for estimating the confidence interval of breathing rate are presented.

(1) A 15-second long radar signal $s(t)$ is taken and preprocessed using a Butter-worth filter with cut-off frequencies of 0.05 Hz and 5 Hz.

(2) Using the WFT method, time-frequency representation of $s_{\mathrm{F}}(t)$ of the preprocessed $s(t)$ is constructed. Micro-Doppler frequency over time $\nu(t)$ is extracted in the range of breathing [0.1–0.5] Hz. Breathing rate $\hat{f}_{\mathrm{b}}$, i.e., the average of $\nu(t)$, is estimated and standard deviation of $\nu(t)$, $\hat{\sigma}$, is calculated.

(3) Using phase and amplitude of $S_{\mathrm{F}}(\nu(t), t)$, the breathing model, $s_{\mathrm{F}}(t, \hat{f}_b)$ in the time domain is constructed and sum of the components related to random movements and intermodulations, $\hat{\varepsilon}(t)$, is calculated.

$$s_{\mathrm{F}}(t) = s_{\mathrm{F}}\left(t, \hat{f}_b\right) + \hat{\varepsilon}(t). \tag{7}$$

(4) A surrogate sample of $\hat{\varepsilon}^*(t)$ is obtained by randomizing the phase of $\hat{\varepsilon}(t)$ in the frequency domain and the residuals in time domain are reconstructed. A bootstrap sample of the radar signal is constructed as

$$s_{\mathrm{F}}^*(t) = s_{\mathrm{F}}\left(t, \hat{f}_{\mathrm{b}}\right) + \hat{\varepsilon}^*(t). \tag{8}$$

(5) The micro-Doppler frequency, $\nu^*(t)$ of $s_{\mathrm{F}}^*(t)$ in the range of breathing is extracted. The bootstrap statistics for this particular bootstrap sample can then be calculated as

$$T^* = \frac{\overline{f}_{\mathrm{b}}^* - \hat{f}_{\mathrm{b}}}{\sigma^*}, \tag{9}$$

where $\overline{f}_{\mathrm{b}}^*$ and σ^* are the mean and standard deviation of $\nu^*(t)$.

(6) Steps 4 and 5 are repeated B times.

(7) The bootstrap estimates are sorted as $T^{*1} < T^{*2} < \cdots < T^{*B}$, and $100(1-\alpha)\%$ confidence interval is computed as

$$\left(T^{*U}\hat{\sigma} + \hat{f}_{\mathrm{b}}, T^{*L}\hat{\sigma} + \hat{f}_{\mathrm{b}}\right), \tag{10}$$

where $U = B - [B\alpha/2] + 1$ and $L = B\alpha/2$.

4. Experiment Setup and Data Collection

The data in this experiment were collected in a simulated prison cell at Carleton University, Ottawa, Canada, after obtaining the appropriate ethics approval. The room measured $3.35 \times 3.15 \times 2.95$ m, and radar was mounted 2.70 m above floor level in one corner, a tripod mounted camera was kept in an adjacent corner, a bed was present along one of the walls opposite to the radar, and a prison-type stainless steel toilet and sink (one joint structure) was kept close to the wall that was opposite to the radar (Figure 5). The radar used in this experiment was a 24.125 GHz CW single-channel Doppler radar prototype model built by K&G Spectrum in Gatineau, Canada, equipped with four adjacent transmit/receive antenna pairs each with 20×70 degree beamwidth. It should be noted that all four transmitter antennas simultaneously transmitted the signal and only one receiver antenna received it at any point in time. A Bosch NE1368 vandal-proof wide angle camera was also used in the experiments for recording baseline activity and posture information. The bed was constructed of concrete support blocks and oriented strand board, and a cotton filled mattress was placed on top of the board. The door of the room was closed, and only the test subject was present in the room. A Braebon model number 0528 piezoelectric respiratory effort sensor was fitted to the subject's chest at sternum level for monitoring breathing activity and three Ambu Blue-T ECG sensors were adhered to the subject's left and right wrists and left ankle for monitoring the ECG signal. All data were streamed to two computers situated outside of the room for recording. Radar data and ECG/breathing belt data were streamed via USB and Bluetooth, respectively, to Computer 1, and camera data were streamed via Ethernet to Computer 2. Three subjects, one male (22 years old, 164 cm height, 60 kg weight) and two females (24, 155 cm, 50 kg and 36, 160 cm, 70 kg), participated in data collection. The following test protocol was followed by all subjects with breaks in between each test:

Figure 5: Experiment setup.

(1) Breathing normally and remaining still for 3 minutes:
   - (i) Standing in front of bed and facing radar
   - (ii) Sitting on the edge of the bed and facing radar with hands resting on knees
   - (iii) Lying on bed in left lateral recumbent position and facing radar

(2) Breathing normally and moving head shoulders and torso randomly for 3 minutes:
   - (i) Standing in front of bed and facing radar
   - (ii) Sitting on the edge of the bed and facing radar with hands resting on knees
   - (iii) Lying on bed in left lateral recumbent position facing radar

A total 18 minutes recording for each subject was collected.

5. Results

As mentioned in [27], posture of the subject may have a substantial effect on the amount of movement of chest and abdomen. In this Section, three postures are investigated, namely, lying down, sitting, and standing, and the results are presented. In addition, the proposed method discussed in Section 3.3 is compared to the other breathing rate estimation methods using CW radar in the literature. In the ubiquitous method of estimating breathing rate, the frequency with the maximum energy (dominant frequency) in the frequency spectrum of the signal in the range of breathing is considered. In order to estimate breathing frequency, the signal is first preprocessed according to Step 1 of the proposed procedure described in Section 3.3. A Hamming window is then applied to the signal, and the chirp transform of the signal is obtained in the range of (0–4) Hz. It has been shown that the chirp transform results in more accurate estimations than regular DFT, since it benefits from improved frequency resolution in the range of frequency of interest [40, 41].

5.1. Lying Down. In the case of a lying down subject, it is observed for most cases that the breathing frequency estimated from the received radar signal is close to that obtained from the RIP signal and the number of significant harmonics related to random body movements or intermodulations is minimum.

Figure 6 shows 15 seconds of the recorded signal when Subject 1 is lying down on the bed, relaxing and breathing normally. It is observed from the RIP signal the subject's breathing pattern is regular and almost periodic. In this example, the radar signal is similar to RIP signal, similar to the simulated signal in the first row of Figure 2.

Figure 7 shows WFT as well as frequency spectrum of the radar signal. It can be seen from this figure that both Fourier transform and WFT exhibit a single significant harmonic at the rate of breathing. Micro-Doppler frequency of radar signal is the dominant frequency in the range of breathing, as shown in Figure 6. The average of micro-Doppler frequencies is calculated as 15.97 bpm and considered to be the estimation of breathing rate. It is noted that the breathing rate calculated from the frequency spectrum (Figure 7(b)) is 16.6 bpm. The micro-Doppler frequencies are extracted from the time-frequency domain using WFT, as shown in Figure 7(a), and then, the signal is converted back to the time domain in order to obtain the breathing model shown in Figure 6. Finally, the residual signal is calculated by subtracting the radar signal from its reconstructed version.

As discussed in Section 3, 200 bootstrap resamples of the signal are constructed. Micro-Doppler frequency of each bootstrap sample as well as the bootstrap statistic T^* is calculated. Figure 8 shows the density function of the bootstrap statistics obtained from 200 resamples. In this figure, $T^{\text{est}} = 0$ is the T-score related to the original signal, whereas $T^{*L} = -0.44$ and $T^{*U} = 0.27$ specify the lower and upper limits of 95% confidence interval of this estimation, respectively. The confidence interval is estimated to be $(15.5, 16.1)$ bpm. The reference breathing rate calculated from RIP signal is 15.6 bpm, and this, such a narrow confidence interval, confirms that the estimation is accurate.

5.2. Posture: Sitting. Similarly for the case of a subject sitting on a bed, breathing is regular, and the radar signal contains harmonics other than the breathing frequency. The time-frequency representation and frequency content of the radar signal are obtained. The dominant peak in the frequency domain is found to be 18.5 bpm. The sequence of micro-Doppler frequencies is then extracted from WFT, and their average is found to be 16.77 bpm. The residuals are then calculated, and its phase is randomized to generate a noise time series with the same energy. Finally, bootstrap resamples are constructed. The upper and lower bootstrap statistics are calculated as $T^{*L} = -0.35$ and $T^{*U} = 0.90$, respectively, resulting in a 95% confidence interval of $(16.3, 18.0)$ bpm, while the reference estimation calculated from RIP signal is 15.68 bpm.

5.3. Standing. When the subject is standing, the abdomen moves without any restriction which may have an influence on the magnitude of periodic breathing movement seen by the radar. In addition, while standing, the body slightly moves back and forth in order to keep the balance. In this case, the radar recording is very different from RIP signal. WFT and chirp transform of the radar signal are obtained, showing that the frequency content of the signal changes dramatically over time, and thus, a strong dominant peak may not be found in the range of breathing rate in the frequency domain. The breathing rate is estimated by extracting the micro-Doppler frequencies to be 14.73 bpm, while the estimation from frequency domain is 24 bpm. It is noted that the energy of residuals is much higher than that of the breathing signal, since it contains intermodulations of large movements of abdomen and the other body movements. The bootstrap statistics are calculated and the upper and lower limits of T-score are found to be $T^{*U} = 0.86$ and $T^{*L} = -0.18$, respectively, resulting in a 95% confidence interval of $(14.32, 18.63)$ bpm. The reference estimation calculated from RIP signal is 16.03 bpm.

5.4. Random Body Movements. Random body movements with linear velocity of V translate into Doppler frequency of $2V/\lambda$ in the received radar signal. For instance, if a part of body moves with the velocity of 0.1 m/s, it leads to a Doppler frequency of 16 Hz. In view of this, these movements may be ignored when looking at WFT of the radar signal in the range of breathing and may not affect the extracted micro-Doppler series. Figure 9 shows the effect of random body movements in the radar signal. It is seen from this figure that the received radar signal is very different from the breathing signal, and random body movements are present as high frequency artifacts. Figure 10 shows WFT and chirp transform of the radar signal. The peak of the signal in the frequency domain occurs at 21.8 bpm, while the average of micro-Doppler series extracted from WFT is 17.8 bpm. From these

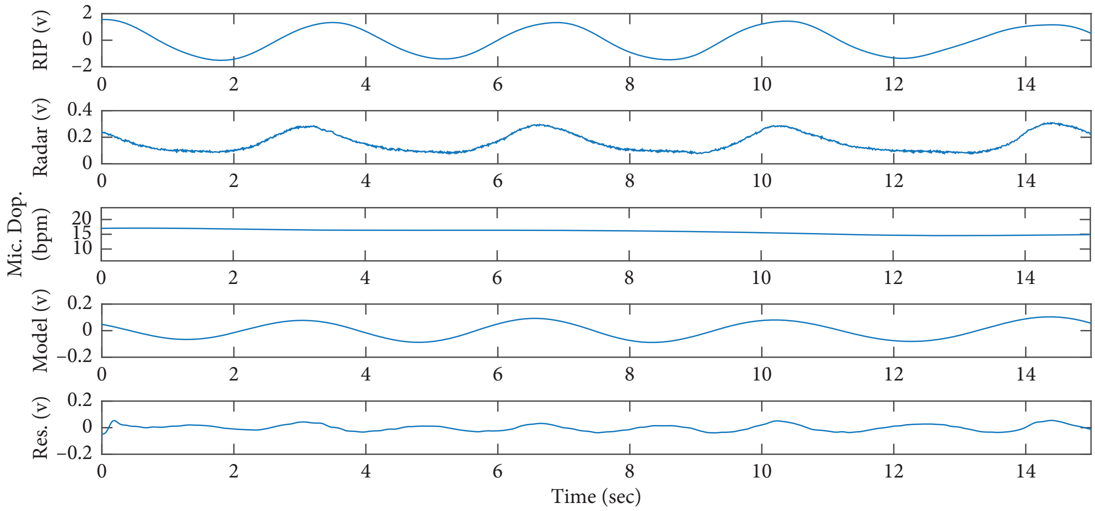

FIGURE 6: From top to bottom: RIP signal, received radar signal, micro-Doppler frequencies extracted from WFT, breathing model, and residuals, when Subject 1 is lying down.

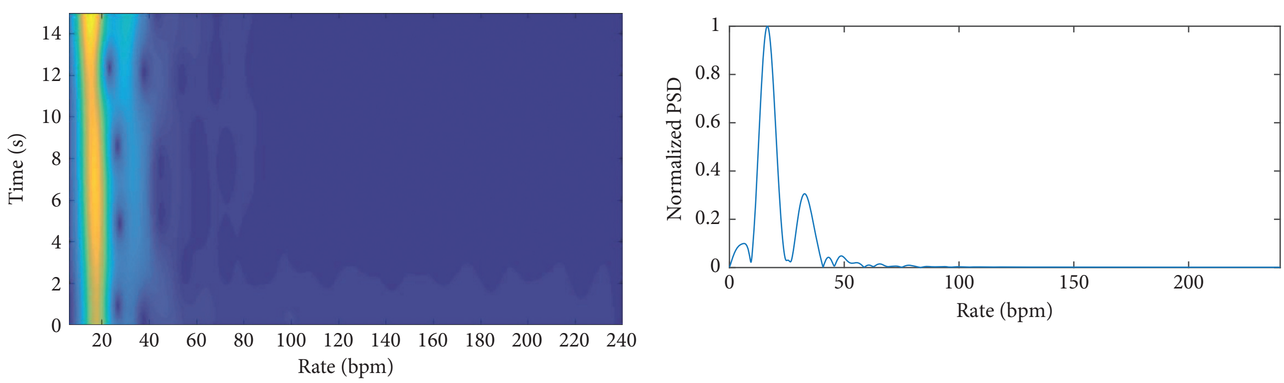

(a) (b)

FIGURE 7: WFT and chirp transform of the radar signal, shown in Figure 6, when the subject is lying down on a bed.

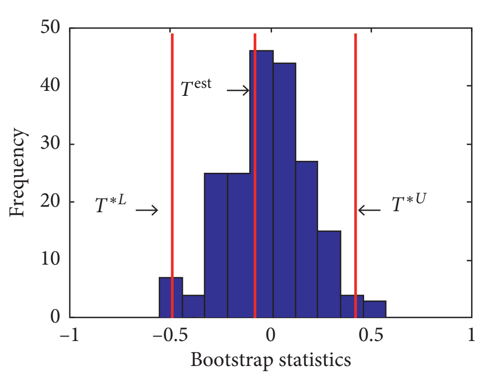

FIGURE 8: Bootstrap statistics for 200 bootstrap resamples constructed from the radar signal shown in Figure 6.

figures, it can be observed that random body movements give rise to very strong residuals. Phase of this residual signal is randomized to generate other possible random movements that could be added to the breathing signal. The bootstrap statistics are calculated and shown in Figure 11. The upper and lower T-score are calculated as $T^{*U} = 1.2$ and $T^{*L} = -1.3$, respectively, resulting in 95% confidence interval of $(14.40, 20.97)$ bpm. The reference breathing rate calculated from RIP is 16.03 bpm.

Breathing rate estimation results obtained using the proposed method as well as the reference value calculated from RIP and that obtained using the FFT-based method (estimated, actual, FFT) bpm, for three subject in three different postures, namely, lying down, sitting, and standing, are listed in Table 2.

It is known that breathing rate increases by age [42, 43]. From Table 2, the actual breathing rates for different postures show that the older subject have consistently higher breathing rate. It is also known that the breathing rate of overweight people is generally higher than the other people. Yet, the weight of all three subjects is considered normal and cannot be a discriminative feature in analyzing their breathing rate. In addition, women tend to breath faster than men [44, 45]. This is in accordance with the actual breathing rate of subjects. As seen from this table, the first two female subjects have higher breathing rates than the third (male)

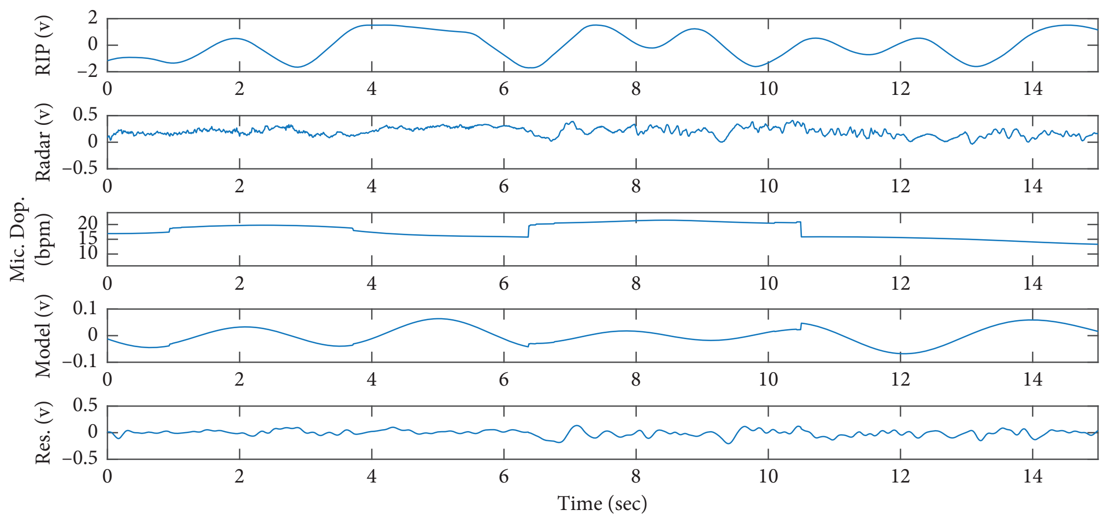

FIGURE 9: From top to bottom: RIP signal, received radar signal, micro-Doppler frequencies extracted from WFT, breathing model, and residuals, when Subject 1 is sitting on the bed and moves head, torso, and arms randomly.

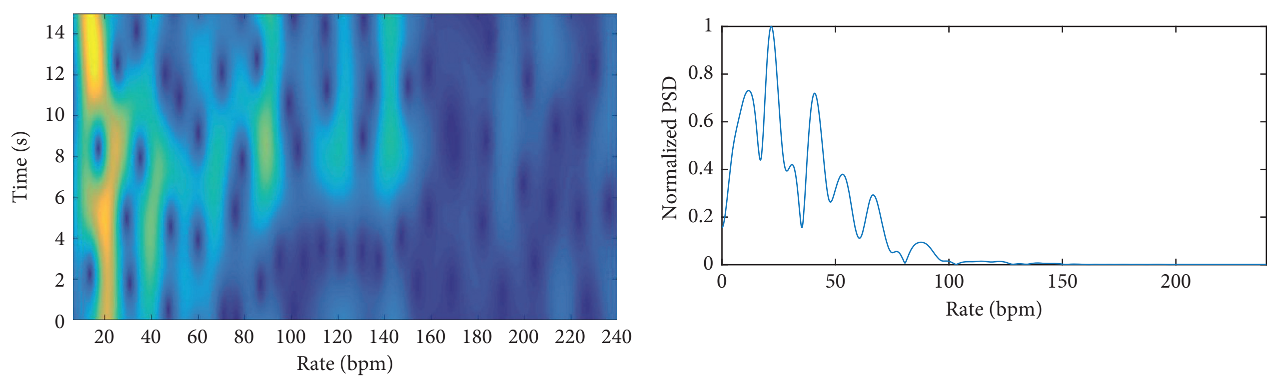

(a) (b)

FIGURE 10: WFT and chirp transform of the radar signal, shown in Figure 9.

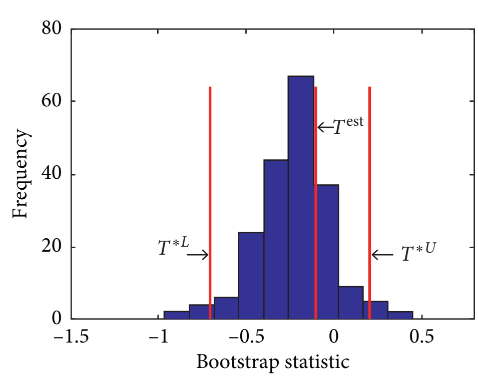

FIGURE 11: Bootstrap statistics corresponds to the radar signal in Figure 9.

one. Height of the subjects has no considerable influence on their breathing rates.

5.5. Overall Results. Figure 12 shows the estimated breathing rate and confidence interval as well as the reference breathing rate calculated from RIP signal for a 6-minute experiment. In this experiment, the subject is lying down on a bed and stays stationary for the first 3 minutes. In the last 3 minutes, the subject moves her arms, head, and shoulders randomly. It is observed from this figure that estimated breathing rate matches the estimation obtained from breathing belt. Table 3 summarizes all the estimation results. In this table, results are in the form of (mean ± standard deviation) of absolute errors between the estimated parameters and the reference estimation calculated from RIP signal. All the values are given in terms of breath per minute along with the number of outliers. It is noted that an element of a vector is called an outlier, if removing it decreases the mean of the vector by 5%.

In Table 3, breathing estimation obtained from chirp transform of the signal is compared with the average of micro-Doppler frequencies for different postures with or without random body movements. In all the cases, WFT is applied with $f_0 = 2$. It is seen from this table that the accuracy of estimation is improved when using the proposed method instead of chirp transform of the signal. In other words, unwanted harmonics of the signal which

Table 2: Breathing rate estimation using the proposed method as well as the reference value and that of the FFT-based method (estimated, actual, and FFT) bpm, for three subjects in three different postures, namely, lying down, sitting, and standing.

	Lying down	Sitting	Standing
Subject 1 (36, 160 cm, 70 kg)	(15.85, 15.60, 16.68)	(16.77, 15.68, 18.52)	(14.73, 16.03, 23.78)
Subject 2 (24, 155 cm, 50 kg)	(13.88, 14.42, 13.78)	(14.63, 15.01, 15.19)	(15.10, 15.23, 19.14)
Subject 3 (22, 164 cm, 60 kg)	(14.67, 13.67, 14.36)	(13.94, 14.15, 14.38)	(15.20, 14.26, 18.38)

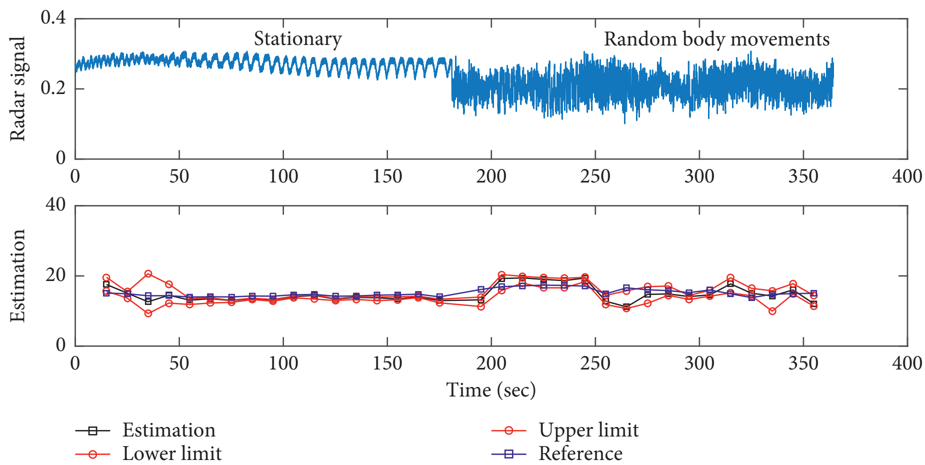

Figure 12: Estimation of breathing within a 95% confidence interval for a 6-minute experiment, where the subject is lying down and stationary for the first 3 minutes and moves shoulders, arms, and head randomly in the last 3 minutes.

Table 3: Summary of results for different postures with or without random body movements.

State of the subject	Number of samples	Absolute error with respect to reference in bpm (number of outliers)				Width of CI in bpm (number of outliers)
		Chirp transform	Average of micro-Doppler	Lower limit of CI	Higher limit of CI	
Lying down and stationary	50	1.32 ± 0.79 (1)	0.82 ± 0.54 (0)	0.88 ± 0.61 (2)	1 ± 0.67 (1)	0.96 ± 0.67 (3)
Sitting and stationary	51	2.8 ± 2.55 (0)	1.25 ± 0.87 (0)	1.52 ± 1.37 (2)	1.76 ± 1.52 (0)	3.05 ± 2.81 (0)
Standing and stationary	51	4.36 ± 2.78 (0)	2.24 ± 1.39 (0)	2.90 ± 2.07 (0)	3.73 ± 3.28 (1)	5.50 ± 4.92 (1)
Lying down with movements	51	3.87 ± 2.07 (0)	2.05 ± 1.22 (0)	2.61 ± 1.96 (0)	2.65 ± 1.96 (0)	3.86 ± 3.03 (0)
Sitting with movements	51	4.57 ± 2.60 (0)	1.76 ± 1.30 (0)	4.23 ± 2.93 (1)	2.89 ± 2.65 (2)	6.35 ± 4.99 (2)
Standing with movements	51	3.99 ± 2.41 (0)	1.84 ± 1.32 (0)	3.29 ± 2.54 (1)	1.97 ± 1.60 (3)	5.26 ± 4.22 (0)

are related to intermodulations between breathing and heart rate and also random body movements can affect estimation of breathing in frequency domain. However, when the signal is analyzed in time-frequency domain, harmonic of breathing can be separated from the other harmonics.

The most accurate estimation is obtained when the subject is stationary and lying down on a bed. In this case, even chirp transform results in an acceptable precision of measurement. Also, the estimated 95% confidence interval is very narrow (almost 1 bpm), indicating that we are quite confident about the estimated breathing rate and in 95% of cases, we would find the estimation in this range in presence of other sources of noise and body movements.

In the case of sitting, the estimation may be improved by using average of micro-Doppler frequencies instead of chirp transform. However, the 95% confidence interval is larger than that of the case, where the subject is lying down (3.05 bpm). In this case, slight movements of body due to balance may introduce uncertainty to the estimation. When the subject is standing, movements of body for balancing are larger and abdomen moves freely. In this case, chirp transform results in huge errors and, in some cases, the estimated breathing is twice that of the reference. Although the estimation improves to absolute error of 2.24 bpm using the proposed method, the width of confidence interval is 5.5 bpm, because of the significant energy of noise and unwanted harmonics with respect to the breathing harmonic.

When the subject starts moving head, shoulders, and torso, the accuracy of estimation using chirp transform drops severely. This estimation may be improved by using the proposed method. Yet, the confidence interval could be large indicating that these estimations are carried out in a noisy environment or in presence of random movements.

It is seen from the results that the proposed method is able to compensate for lack of quadrature channel and estimate breathing using single-channel CW radar with an average absolute error of estimation equal to 1.88 breaths per minute. Although this error seems high for monitoring patients, the error rate is satisfactory when the use of wearable devices or cameras is not allowed, such as continuous monitoring of breathing rate of inmates and elderly people, during sleep or rescue operations. It should be noted that breathing rate estimation is realized based on the detected motion, observed at a distance, and therefore is much more susceptible to noise, interference, and artifacts and is not expected to be as accurate at estimating breathing rate as the RIP band.

One of the limitations of the proposed method is that it is sensitive to the parameter f_0 in (4), which controls the trade-off between time and frequency resolution of WFT. This parameter has been set to $f_0 = 2$, which was found by trial and error and might need to be adjusted for other radar systems. In future works, ways of optimizing f_0 needs to be investigated. The proposed method will also be examined in other environments where interference from other moving objects is present in the room.

It is noted that the system complexity, cost, and power consumption of a two-channel radar are well known to be higher than those of a single-channel radar, because a single-channel radar requires only one receiver branch [46, 47] and does not require balancing I/Q data [48].

6. Conclusion

In this work, a method for estimating breathing rate using a single-channel CW radar has been proposed. It has been shown through several simulations that Fourier transform-based estimation methods are not reliable to estimate breathing rate, when only one channel is used in the hardware of the radar. Quadrature receivers for vital sign monitoring have been well studied. However, single-channel receivers have not been well researched. Our study has demonstrated how single-channel radar can be used for monitoring in realistic situations and has provided estimates reasonably well. In case of a two-channel radar, the phase extracted from quadrature demodulation is a linear combination of breathing-related harmonic and those originated from noise and random body movements and can be processed by Fourier transform. However, in a single-channel CW radar, cosine of phase is received which is the output of a nonlinear system. In view of this, using time-frequency analysis has been proposed in order to extract the derivative of phase (or Doppler frequency) of the received signal over time. Using the proposed method, the received signal has been decomposed to the main harmonics originated from breathing and residuals, which are the sum of unwanted harmonics. Although the frequency of the main harmonic has been shown to be an estimate of breathing, our results have shown that this estimation can significantly be affected by unwanted harmonics. Therefore, bootstrap resampling has been used to support the estimations with a 95% confidence interval. Surrogates of unwanted harmonics have been generated by randomizing the phase of residuals, knowing that information of random body movements and unwanted intermodulations is hidden in the phase of the residuals. The results have also shown that the proposed method is able to compensate for lack of quadrature channel and can be used to estimate breathing using single-channel CW radar with an average absolute error of estimation equal to 1.88 breaths per minute.

Data Availability

The data used in the experiments will be made available online.

Conflicts of Interest

The authors declare that there are no conflicts of interest regarding the publication of this paper.

Acknowledgments

We would like to thank NSERC for funding this research through IDEA to Innovation and Discovery program. We would also like to thank Mr. Andre Gagnon from K&G Spectrum Inc. for providing the radar prototype and Mr. Sylvio Bisson from Correctional Service Canada for his support of this research.

References

[1] L. Anitori, A. de Jong, and F. Nennie, "FMCW radar for life-sign detection," in *Proceedings of the IEEE Radar Conference*, pp. 1–6, Pasadena, CA, USA, May 2009.

[2] O. Postolache, P. S. Girão, R. N. Madeira, and G. Postolache, "Microwave FMCW Doppler radar implementation for in-house pervasive health care system," in *Proceedings of the IEEE International Workshop onMedical Measurements and Applications (MeMeA)*, pp. 47–52, Ottawa, ON, Canada, April 2010.

[3] I. Nejadgholi, H. Sadreazami, S. Rajan, and M. Bolic, "Classification of Doppler radar reflections as preprocessing for breathing rate monitoring," *IET Signal Processing*, vol. 13, no. 1, pp. 21–28, 2019.

[4] J. Paton and R. Jenkins, "Suicide and suicide attempts in prisons," in *Prevention and Treatment of Suicidal Behavior: From Science to Practice*, pp. 307–334, Oxford University Press, Oxford, UK, 2005.

[5] P. B. Patil, S. Chapalkar, N. D. Dhamne, and N. M. Patel, "Monitoring system for prisoner with GPS using wireless sensor network (WSN)," *International Journal of Computer Applications*, vol. 91, no. 13, pp. 28–31, 2014.

[6] C. Li, V. M. Lubecke, O. Boric-Lubecke, and J. Lin, "A review on recent advances in Doppler radar sensors for noncontact healthcare monitoring," *IEEE Transactions on Microwave Theory and Techniques*, vol. 61, no. 5, pp. 2046–2060, 2013.

[7] F. Adib, H. Mao, Z. Kabelac, and D. Katabi, "Smart homes that monitor breathing and heart rate," in *Proceedings of the 33rd Annual ACM Conference on Human Factors in Computing Systems (CHI'15)*, pp. 837–846, Seoul, Republic of Korea, April 2015.

[8] F. Adib, C.-Y. Hsu, H. Mao, D. Katabi, and F. Durand, "Capturing the human figure through a wall," *ACM Transactions on Graphics*, vol. 34, no. 6, pp. 1–13, 2015.

[9] F. Adib, Z. Kabelac, and K. Dina, "Multi-person localization via RF body reflections," in *Proceedings of the 12th USENIX*

Conference on Networked Systems Design and Implementation (NSDI 15), pp. 279–292, Oakland, CA, USA, May 2015.

[10] A. D. Droitcour, O. Boric-Lubecke, V. M. Lubecke, J. Lin, and G. T. A. Kovacs, "Range correlation and I/Q performance benefits in single-chip silicon Doppler radars for noncontact cardiopulmonary monitoring," *IEEE Transactions on Microwave Theory and Techniques*, vol. 52, no. 3, pp. 838–848, 2004.

[11] C. Li, Y. Xiao, and J. Lin, "Experiment and spectral analysis of a low-power Ka-band heartbeat detector measuring from four sides of a human body," *IEEE Transactions on Microwave Theory and Techniques*, vol. 54, no. 12, pp. 4464–4471, 2006.

[12] C. Li and J. Lin, "Random body movement cancellation in Doppler radar vital sign detection," *IEEE Transactions on Microwave Theory and Techniques*, vol. 56, no. 12, pp. 3143–3152, 2008.

[13] B.-K. Park, O. Boric-Lubecke, and V. M. Lubecke, "Arctangent demodulation with dc offset compensation in quadrature Doppler radar receiver systems," *IEEE Transactions on Microwave Theory and Techniques*, vol. 55, no. 5, pp. 1073–1079, 2007.

[14] C. Gu, C. Li, J. Lin, J. Long, J. Huangfu, and L. Ran, "Instrument-based non-contact Doppler radar vital sign detection system using heterodyne digital quadrature demodulation architecture," *IEEE Transactions on Instrumentation and Measurement*, vol. 59, no. 6, pp. 1580–1588, 2010.

[15] A. M. Vergara and V. M. Lubecke, "Data acquisition system for Doppler radar vital-sign monitor," in *Proceedings of the 29th Annual International Conference of the IEEE Engineering in Medicine and Biology Society*, pp. 2269–2272, Lyon, France, August 2007.

[16] T. Hall, D. Lie, T. Nguyen et al., "Non-contact sensor for long-term continuous vital signs monitoring: a review on intelligent phased-array Doppler sensor design," *Sensors*, vol. 17, no. 11, p. 2632, 2017.

[17] C. Li, J. Cummings, J. Lam, E. Graves, and W. Wu, "Radar remote monitoring of vital signs," *IEEE Microwave Magazine*, vol. 10, no. 1, pp. 47–56, 2009.

[18] T.-Y. Chin, K.-Y. Lin, S.-F. Chang, and C.-C. Chang, "A fast clutter cancellation method in quadrature Doppler radar for non-contact vital signal detection," in *Proceedings of the IEEE MTT-S International Microwave Symposium Digest (MTT)*, pp. 764–767, Anaheim, CA, USA, May 2010.

[19] J. E. Kiriazi, O. Boric-Lubecke, and V. M. Lubecke, "Considerations in measuring vital signs cross section with Doppler radar," in *Proceedings of the IEEE Radio and Wireless Symposium*, pp. 426–429, Phoenix, AZ, USA, January 2011.

[20] F.-K. Wang, T.-S. Horng, K.-C. Peng, J.-K. Jau, J.-Y. Li, and C.-C. Chen, "Single-antenna Doppler radars using self and mutual injection locking for vital sign detection with random body movement cancellation," *IEEE Transactions on Microwave Theory and Techniques*, vol. 59, no. 12, pp. 3577–3587, 2011.

[21] I. Mostafanezhad, E. Yavari, O. Boric-Lubecke, V. M. Lubecke, and D. P. Mandic, "Cancellation of unwanted Doppler radar sensor motion using empirical mode decomposition," *IEEE Sensors Journal*, vol. 13, no. 5, pp. 1897–1904, 2013.

[22] V. C. Chen, F. Fayin Li, S.-S. Shen-Shyang Ho, and H. Wechsler, "Micro-Doppler effect in radar: phenomenon, model, and simulation study," *IEEE Transactions on Aerospace and Electronic Systems*, vol. 42, no. 1, pp. 2–21, 2006.

[23] G. E. Smith, K. Woodbridge, and C. J. Baker, "Radar micro-Doppler signature classification using dynamic time warping," *IEEE Transactions on Aerospace and Electronic Systems*, vol. 46, no. 3, pp. 1078–1096, 2010.

[24] P. Molchanov, J. Astola, K. Egiazarian, and A. Totsky, "Classification of ground moving radar targets by using joint time-frequency analysis," in *Proceedings of the IEEE Radar Conference (RADAR)*, pp. 0366–0371, Atlanta, GA, USA, May 2012.

[25] I. Nejadgholi, S. Rajan, and M. Bolic, "Time-frequency based contactless estimation of vital signs of human while walking using pmcw radar," in *Proceedings of the IEEE 18th International Conference on e-Health Networking, Applications and Services (Healthcom)*, pp. 1–6, Munich, Germany, September 2016.

[26] C. Gu and C. Li, "Assessment of human respiration patterns via noncontact sensing using Doppler multi-radar system," *Sensors*, vol. 15, no. 3, pp. 6383–6398, 2015.

[27] H. Kaneko and J. Horie, "Breathing movements of the chest and abdominal wall in healthy subjects," *Respiratory Care*, vol. 57, no. 9, pp. 1442–1451, 2012.

[28] D. Iatsenko, P. V. McClintock, and A. Stefanovska, "Nonlinear mode decomposition: a noise-robust, adaptive decomposition method," *Physical Review E*, vol. 92, no. 3, pp. 03–29, 2015.

[29] B. Efron and R. J. Tibshirani, *An Introduction to the Bootstrap*, CRC Press, Boca Raton, FL, USA, 1994.

[30] A. M. Zoubir and B. Boashash, "The bootstrap and its application in signal processing," *IEEE Signal Processing Magazine*, vol. 15, no. 1, pp. 56–76, 1998.

[31] S. Kazemi, A. Ghorbani, H. Amindavar, and D. R. Morgan, "Vital-sign extraction using bootstrap-based generalized warblet transform in heart and respiration monitoring radar system," *IEEE Transactions on Instrumentation and Measurement*, vol. 65, no. 2, pp. 255–263, 2016.

[32] C. Z. Mooney, R. D. Duval, and R. Duval, *Bootstrapping: A Nonparametric Approach to Statistical Inference*, Sage, Thousand Oaks, CA, USA, 1993.

[33] A. M. Zoubir and D. R. Iskander, *Bootstrap Techniques for Signal Processing*, Cambridge University Press, Cambridge, UK, 2004.

[34] T. Schreiber and A. Schmitz, "Surrogate time series," *Physica D: Nonlinear Phenomena*, vol. 142, no. 3-4, pp. 346–382, 2000.

[35] D. N. Politis, "The impact of bootstrap methods on time series analysis," *Statistical Science*, vol. 18, no. 2, pp. 219–230, 2003.

[36] D. N. Politis and H. White, "Automatic block-length selection for the dependent bootstrap," *Econometric Reviews*, vol. 23, no. 1, pp. 53–70, 2004.

[37] E. Paparoditis and D. N. Politis, "Tapered block bootstrap," *Biometrika*, vol. 88, no. 4, pp. 1105–1119, 2001.

[38] S. N. Lahiri, "Theoretical comparisons of block bootstrap methods," *Annals of Statistics*, vol. 27, no. 1, pp. 386–404, 1999.

[39] J. Chang and P. Hall, "Double-bootstrap methods that use a single double-bootstrap simulation," *Biometrika*, vol. 102, no. 1, pp. 203–214, 2015.

[40] M. Aiello, A. Cataliotti, and S. Nuccio, "A comparison of spectrum estimation techniques for periodic not stationary signals," in *Proceedings of the 18th IEEE Instrumentation and Measurement Technology Conference (IMTC)*, pp. 1130–1134, Budapest, Hungary, May 2001.

[41] L. Rabiner, R. Schafer, and C. Rader, "The chirp z-transform algorithm," *IEEE Transactions on Audio and Electroacoustics*, vol. 17, no. 2, pp. 86–92, 1969.

[42] J. P. McFadden, R. C. Price, H. D. Eastwood, and R. S. Briggs, "Raised respiratory rate in elderly patients: a valuable physical sign," *BMJ*, vol. 284, no. 6316, pp. 626-627, 1982.

[43] G. Yuan, N. A. Drost, and R. A. McIvor, "Respiratory rate and breathing pattern," *McMaster University Medical Journal*, vol. 10, no. 1, pp. 23–25, 2013.

[44] H. I. Chen and C. S. Kuo, "Relationship between respiratory muscle function and age, sex, and other factors," *Journal of Applied Physiology*, vol. 66, no. 2, pp. 943–948, 1989.

[45] A. W. Sheel, J. C. Richards, G. E. Foster, and J. A. Guenette, "Sex differences in respiratory exercise physiology," *Sports Medicine*, vol. 34, no. 9, pp. 567–579, 2004.

[46] B.-K. Park, S. Yamada, O. Boric-Lubecke, and V. Lubecke, "Single-channel receiver limitations in Doppler radar measurements of periodic motion," in *Proceedings of the IEEE Radio and Wireless Symposium*, pp. 99–102, San Diego, CA, USA, January 2006.

[47] F. Lurz, S. Mann, S. Linz et al., "A low power 24 GHz radar system for occupancy monitoring," in *Proceedings of the IEEE Radio and Wireless Symposium (RWS)*, pp. 111–113, San Diego, CA, USA, January 2015.

[48] A. W. Doerry, "Balancing I/Q data in radar range-Doppler images," in *Proceedings of the Radar Sensor Technology XIX; and Active and Passive Signatures VI*, vol. 9461, article 94611Y, International Society for Optics and Photonics, Baltimore, MD, USA, April 2015.

Hindawi
Journal of Healthcare Engineering
Volume 2019, Article ID 4180949, 7 pages
https://doi.org/10.1155/2019/4180949

Research Article

An Efficient Deep Learning Approach to Pneumonia Classification in Healthcare

Okeke Stephen,[1] **Mangal Sain**,[2] **Uchenna Joseph Maduh**,[3] **and Do-Un Jeong**[2]

[1] *Department of Computer Engineering, Dongseo University, Busan, Republic of Korea*
[2] *Division of Computer Engineering, Dongseo University, Busan, Republic of Korea*
[3] *Department of Civil Engineering, Yeungnam University, Gyeongsan, Republic of Korea*

Correspondence should be addressed to Mangal Sain; mangalsain1@gmail.com and Do-Un Jeong; dujeong@dongseo.ac.kr

Received 19 December 2018; Accepted 24 February 2019; Published 27 March 2019

Guest Editor: Ahyoung Choi

This study proposes a convolutional neural network model trained from scratch to classify and detect the presence of pneumonia from a collection of chest X-ray image samples. Unlike other methods that rely solely on transfer learning approaches or traditional handcrafted techniques to achieve a remarkable classification performance, we constructed a convolutional neural network model from scratch to extract features from a given chest X-ray image and classify it to determine if a person is infected with pneumonia. This model could help mitigate the reliability and interpretability challenges often faced when dealing with medical imagery. Unlike other deep learning classification tasks with sufficient image repository, it is difficult to obtain a large amount of pneumonia dataset for this classification task; therefore, we deployed several data augmentation algorithms to improve the validation and classification accuracy of the CNN model and achieved remarkable validation accuracy.

1. Introduction

The risk of pneumonia is immense for many, especially in developing nations where billions face energy poverty and rely on polluting forms of energy. The WHO estimates that over 4 million premature deaths occur annually from household air pollution-related diseases including pneumonia [1]. Over 150 million people get infected with pneumonia on an annual basis especially children under 5 years old [2]. In such regions, the problem can be further aggravated due to the dearth of medical resources and personnel. For example, in Africa's 57 nations, a gap of 2.3 million doctors and nurses exists [3, 4]. For these populations, accurate and fast diagnosis means everything. It can guarantee timely access to treatment and save much needed time and money for those already experiencing poverty.

Deep neural network models have conventionally been designed, and experiments were performed upon them by human experts in a continuing trial-and-error method. This process demands enormous time, know-how, and resources. To overcome this problem, a novel but simple model is introduced to automatically perform optimal classification tasks with deep neural network architecture. The neural network architecture was specifically designed for pneumonia image classification tasks. The proposed technique is based on the convolutional neural network algorithm, utilizing a set of neurons to convolve on a given image and extract relevant features from them. Demonstration of the efficacy of the proposed method with the minimization of the computational cost as the focal point was conducted and compared with the exiting state-of-the-art pneumonia classification networks.

In recent times, CNN-motivated deep learning algorithms have become the standard choice for medical image classifications although the state-of-the-art CNN-based classification techniques pose similar fixated network architectures of the trial-and-error system which have been their designing principle. U-Net [5], SegNet [6], and CardiacNet [7] are some of the prominent architectures for medical image examination. To design these models, specialists often have a large number of choices to make design decisions, and intuition significantly guides manual search process. Models like evolutionary-based algorithms [8] and reinforcement learning (RL) [9] have been introduced to locate optimum network hyperparameters during training. However, these techniques are computationally expensive, gulping a ton of processing power. As an alternative, our study proposes a conceptually simple yet efficient network model to handle the pneumonia classification problem as shown in Figures 1 and 2.

CNNs have an edge over DNNs by possessing a visual processing scheme that is equivalent to that of humans and extremely optimized structure for handling images and 2D and 3D shapes, as well as ability to extract abstract 2D features through learning. The max-pooling layer of the convolutional neural network is effective in variant shape absorptions and comprises sparse connections in conjunction with tied weights. When compared with fully connected (FC) networks of equivalent size, CNNs have a considerably smaller amount of parameters. Most importantly, gradient-based learning algorithms are employed in training CNNs and they are less prone to diminishing gradient problem. Since the gradient-based algorithm is responsible for training the whole network in order to directly diminish an error criterion, highly optimized weights can be produced by CNNs.

2. Related Works

Latest improvements in deep learning models and the availability of huge datasets have assisted algorithms to outperform medical personnel in numerous medical imaging tasks such as skin cancer classification [11], hemorrhage identification [12], arrhythmia detection [13], and diabetic retinopathy detection [14]. Automated diagnoses enabled by chest radiographs have received growing interests. These algorithms are increasingly being used for conducting lung nodule detection [15] and pulmonary tuberculosis classification [16]. The performance of several convolutional models on diverse abnormalities relying on the publicly available OpenI dataset [17] found that the same deep convolutional network architecture does not perform well across all abnormalities [18], ensemble models significantly improved classification accuracy when compared with single model, and finally, deep learning method improved accuracy when compared to rule-based methods.

Statistical dependency between labels [19] was studied to arrive at more precise predictions, thereby outperforming other techniques on given 13 images selected from 14 classes [20]. Algorithms for mining and predicting labels emanating from radiology images as well as reports have been studied [21–23], but the image labels were generally constrained to disease tags, thus lacking contextual information. Detection of diseases from X-ray images was examined in [24–26], classifications on image views from chest X-ray were carried out in [27], and body parts segmentation from chest X-ray images and computed tomography was performed in [23, 28]. Conversely, learning image features from text and creating image descriptions relative to what a human would describe are yet to be exploited.

3. Materials and Methods

We present the detailed experiments and evaluation steps undertaken to test the effectiveness of the proposed model. Our experiments were based on a chest X-ray image dataset proposed in [29]. We deployed Keras open-source deep learning framework with tensorflow backend [10] to build and train the convolutional neural network model. All experiments were run on a standard PC with an Nvidia GeForce GTX TITAN Xp GPU card of 12 GB, cuDNN v7.0 library, and CUDA Toolkit 9.0.

3.1. Dataset. The original dataset [25] consists of three main folders (i.e., training, testing, and validation folders) and two subfolders containing pneumonia (P) and normal (N) chest X-ray images, respectively. A total of 5,856 X-ray images of anterior-posterior chests were carefully chosen from retrospective pediatric patients between 1 and 5 years old. The entire chest X-ray imaging was conducted as part of patients' routine medical care. To balance the proportion of data assigned to the training and validation set, the original data category was modified. We rearranged the entire data into training and validation set only. A total of 3,722 images were allocated to the training set and 2,134 images were assigned to the validation set to improve validation accuracy.

3.2. Preprocessing and Augmentation. We employed several data augmentation methods to artificially increase the size and quality of the dataset. This process helps in solving overfitting problems and enhances the model's generalization ability during training. The settings deployed in image augmentation are shown below in Table 1.

The rescale operation represents image reduction or magnification during the augmentation process. The rotation range denotes the range in which the images were randomly rotated during training, i.e., 40 degrees. Width shift is the horizontal translation of the images by 0.2 percent, and height shift is the vertical translation of the images by 0.2 percent. In addition, a shear range of 0.2 percent clips the image angles in a counterclockwise direction. The zoom range randomly zooms the images to the ratio of 0.2 percent, and finally, the images were flipped horizontally.

3.3. Model. Figure 3 shows the overall architecture of the proposed CNN model which consists of two major parts: the feature extractors and a classifier (sigmoid activation function). Each layer in the feature extraction layer takes its immediate preceding layer's output as input, and its output is passed as an input to the succeeding layers. The proposed architecture in Figure 3 consists of the convolution, max-pooling, and classification layers combined together. The feature extractors comprise conv3×3, 32; conv3×3, 64; conv3×3, 128; conv3×3, 128, max-pooling layer of size 2×2, and a RELU activator between them. The output of the convolution and max-pooling operations are assembled into

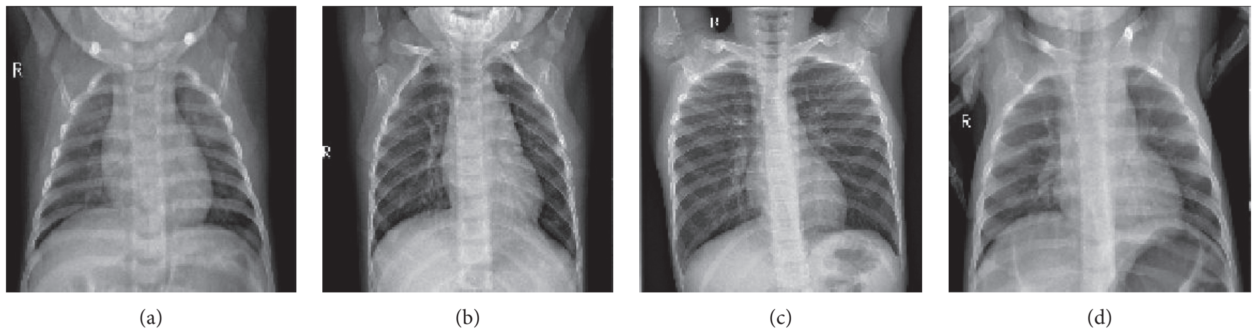

Figure 1: Sample images without pneumonia.

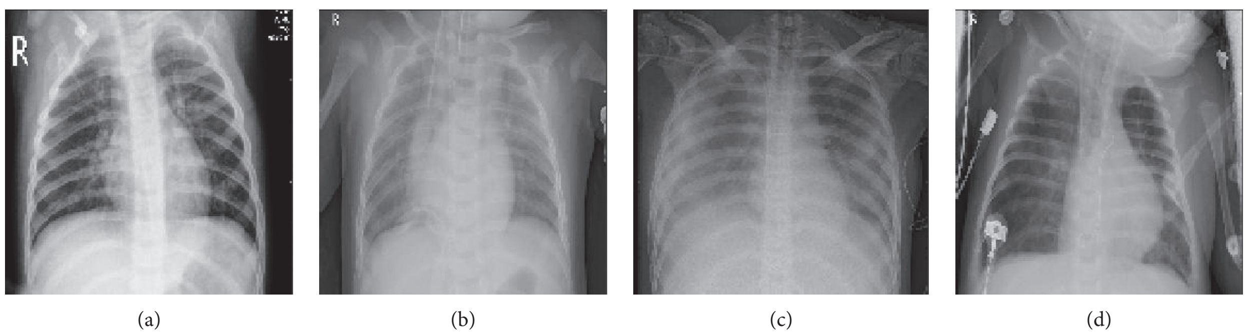

Figure 2: Sample images with pneumonia [10].

Table 1: Settings for the image augmentation.

Method	Setting
Rescale	1/255
Rotation range	40
Width shift	0.2
Height shift	0.2
Shear range	0.2
Zoom range	0.2
Horizontal flip	True

2D planes called feature maps, and we obtained $198 \times 198 \times 32$, $97 \times 97 \times 62$, $46 \times 64 \times 128$, and $21 \times 21 \times 128$ sizes of feature maps, respectively, for the convolution operations and $99 \times 99 \times 32$, $48 \times 48 \times 64$, $23 \times 23 \times 128$, and $10 \times 10 \times 128$ sizes of feature maps from the pooling operations, respectively, with an input of image of size $200 \times 200 \times 3$ as shown in Table 2. It is worthy to note that each plane of a layer in the network was obtained by combining one or more planes of previous layers.

The classifier is placed at the far end of the proposed convolutional neural network (CNN) model. It is simply an artificial neural network (ANN) often referred to as a dense layer. This classifier requires individual features (vectors) to perform computations like any other classifier. Therefore, the output of the feature extractor (CNN part) is converted into a 1D feature vector for the classifiers. This process is known as flattening where the output of the convolution operation is flattened to generate one lengthy feature vector for the dense layer to utilize in its final classification process. The classification layer contains a flattened layer, a dropout of size 0.5, two dense layers of size 512 and 1, respectively, a RELU between the two dense layers and a sigmoid activation function that performs the classification tasks.

4. Results

To evaluate and validate the effectiveness of the proposed approach, we conducted the experiments 10 times each for three hours, respectively. Parameter and hyperparameters were heavily turned to increase the performance of the model. Different results were obtained, but this study reports only the most valid.

As explained above, methods such as data augmentation, learning rate variation, and annealing were deployed to assist in fitting the small dataset into deep convolutional neural network architecture. This was in order to obtain substantial results as shown in Figure 4. The final results obtained are training loss = 0.1288, training accuracy = 0.9531, validation loss: 0.1835, and validation accuracy of 0.9373.

CNN frameworks always require images of fixed sizes during training. Thus, to demonstrate the validation performance of our model on variant input data, we reshaped the X-ray images into $100 \times 100 \times 3$, $150 \times 150 \times 3$, $200 \times 200 \times 3$, $250 \times 250 \times 3$, and $300 \times 300 \times 3$ sizes, respectively, trained them three hours each, and obtained their overall average performance as shown in Figure 4 and Table 3.

The larger the size of the transformed images, the lesser the validation accuracy obtained. In contrast, smaller-sized

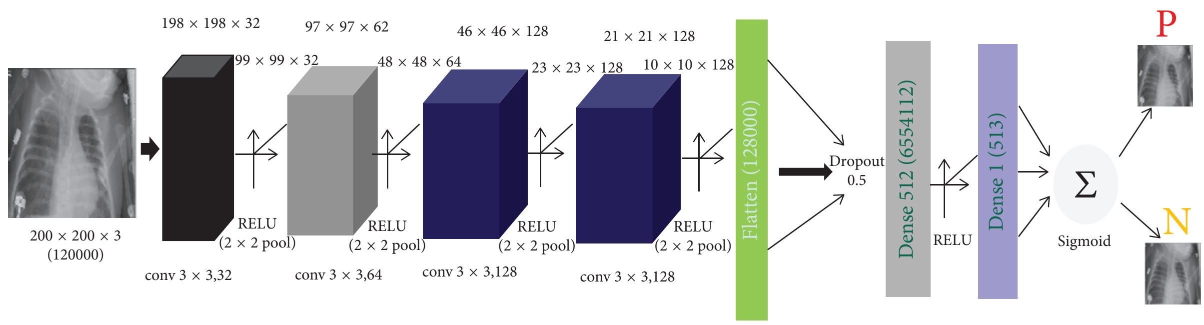

Figure 3: The proposed architecture.

Table 2: The output of the proposed network architecture.

Layer (type)	Output shape	Turtles
conv2d_9 (conv2D)	(None, 198, 198, 32)	896
max_Pooling2d_9 (MaxPooling2)	(None, 99, 99, 32)	0
conv2d_10 (conv2D)	(None, 97, 97, 64)	18496
max_Pooling2d_10 (MaxPooling2)	(None, 48, 48, 64)	0
conv2d_11 (conv2D)	(None, 46, 46, 128)	73856
max_Pooling2d_11 (MaxPooling2)	(None, 23, 23, 128)	0
conv2d_12 (conv2D)	(None, 21, 21, 128)	147584
max_Pooling2d_12 (MaxPooling2)	(None, 10, 10, 128)	0
flatten_3 (Flatten)	(None, 12800)	0
dropout_3 (Dropout)	(None, 12800)	0
dense_5 (Dense)	(None, 512)	6554112
dense_6 (Dense)	(None, 1)	513

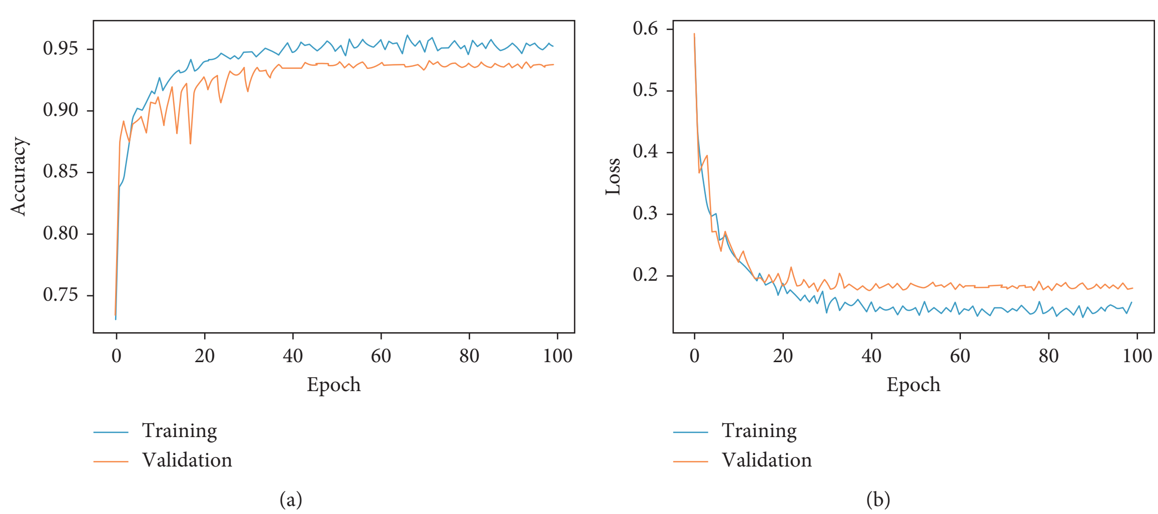

Figure 4: Performance of the classification model on $200 \times 200 \times 3$ data size.

training images induced a slight improvement in validation accuracy as shown in Figure 5. However, the little slips in the validation accuracy do not register substantial impact on the overall classification performance of the proposed model. Larger images also required more training time and computation cost, and the performances of $150 \times 150 \times 3$ and $200 \times 200 \times 3$ image sizes were similar, as shown in Table 3 and Figure 5, respectively. Finally, we propose the $200 \times 200 \times 3$ model since it produced better validation accuracy of approximately 94 percent with a minimal training loss of 0.1835.

5. Discussion

We developed a model to detect and classify pneumonia from chest X-ray images taken from frontal views at high validation accuracy. The algorithm begins by transforming chest X-ray images into sizes smaller than the original. The next step involves the identification and classification of images by the convolutional neural network framework, which extracts features from the images and classifies them. Due to the effectiveness of the trained CNN model for identifying pneumonia from chest X-ray images, the

Table 3: Performance of the classification model on different data sizes.

Data size	Training accuracy	Validation accuracy
100	0.9375	0.9226
150	0.9422	0.9343
200	**0.9531**	**0.9373**
250	0.9513	0.9297
300	0.9566	0.9267
Average	0.94814	0.93012

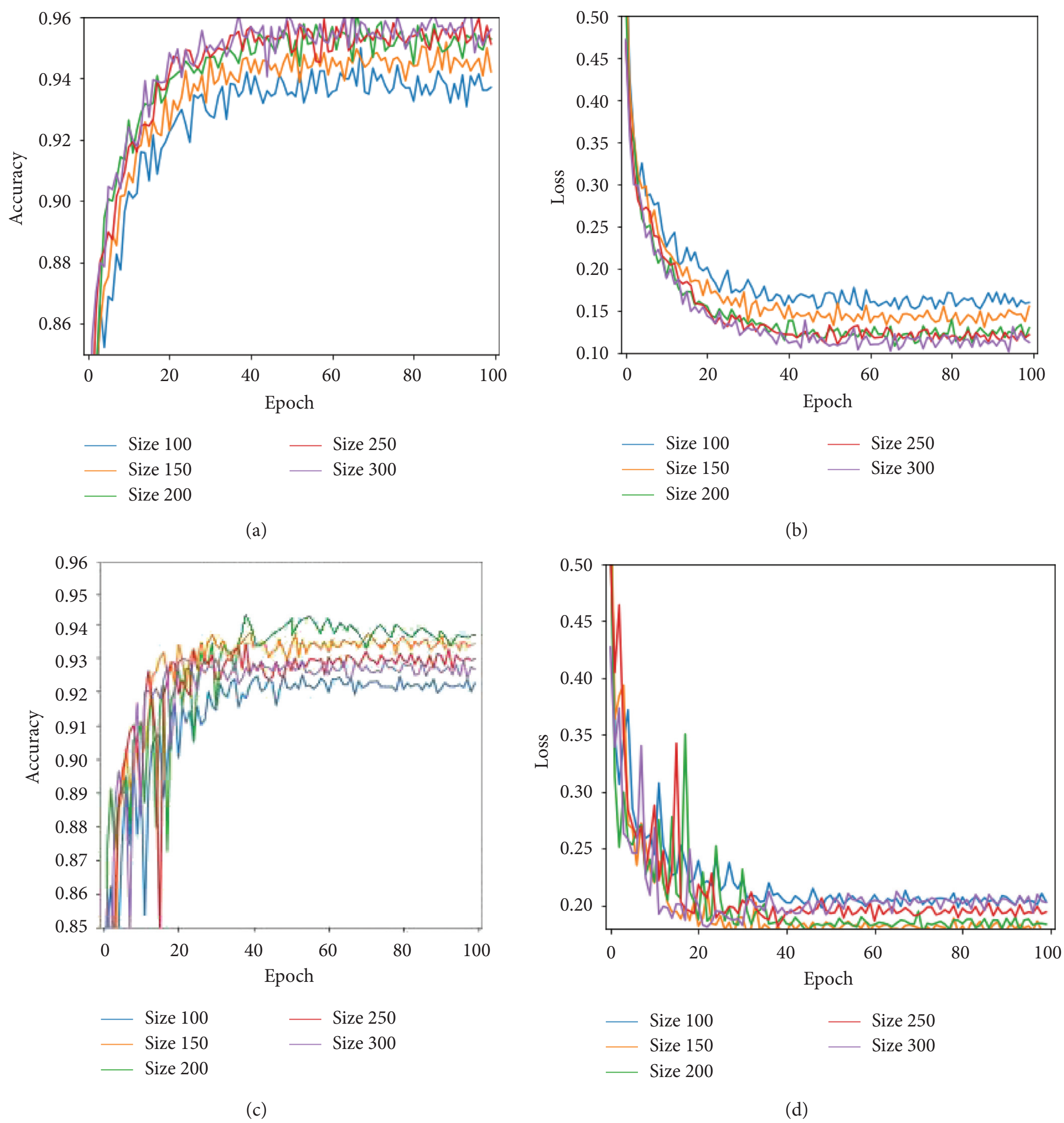

Figure 5: Performance of the classification model on varied data sizes.

validation accuracy of our model was significantly higher when compared with other approaches. To affirm the performance of the model, we repeated the training process of the model several times, each time obtaining the same results. To validate the performance of the trained model on different chest X-ray image sizes, we varied the sizes of the training and validation dataset and still obtained relatively similar results. This will go a long way in improving the health of at-risk children in energy-poor environments. The study was limited by depth of data. With increased access to data and training of the model with radiological data from patients and nonpatients in different parts of the world, significant improvements can be made.

6. Conclusions

We have demonstrated how to classify positive and negative pneumonia data from a collection of X-ray images. We build our model from scratch, which separates it from other methods that rely heavily on transfer learning approach. In the future, this work will be extended to detect and classify X-ray images consisting of lung cancer and pneumonia. Distinguishing X-ray images that contain lung cancer and pneumonia has been a big issue in recent times, and our next approach will tackle this problem.

Data Availability

The data used to support the findings of this study are included within the article.

Conflicts of Interest

The authors declare that there are no conflicts of interest regarding the publication of this paper.

Acknowledgments

This research was supported by the Basic Science Research Program through the National Research Foundation of Korea (NRF) funded by the Ministry of Education (No. 2018R1D1A1B07045337).

References

[1] World Health Organization, *Household Air Pollution and Health [Fact Sheet]*, WHO, Geneva, Switzerland, 2018, http://www.who.int/newa-room/fact-sheets/detail/household-air-pollution-and-health.

[2] I. Rudan, L. Tomaskovic, C. Boschi-Pinto, and H. Campbell, "Global estimate of the incidence of clinical pneumonia among children under five years of age," *Bulletin of the World Health Organization*, vol. 82, pp. 85–903, 2004.

[3] V. Narasimhan, H. Brown, A. Pablos-Mendez et al., "Responding to the global human resources crisis," *The Lancet*, vol. 363, no. 9419, pp. 1469–1472, 2004.

[4] S. Naicker, J. Plange-Rhule, R. C. Tutt, and J. B. Eastwood, "Shortage of healthcare workers in developing countries," *Africa, Ethnicity & Disease*, vol. 19, p. 60, 2009.

[5] R. Olaf, F. Philipp, and B. Thomas, *U-Net: Convolutional Networks for Biomedical Image Segmentation*, MICCAI Springer, New York, NY, USA, 2015.

[6] B. Vijay, K. Alex, and C. Roberto, "Segnet: Deep convolutional encoder-decoder architecture for image segmentation," 2015, http://arxiv.org/abs/1511.00561.

[7] M. Aliasghar, K. Rashed, R. Kawal, B. Jeremy, and B. Ulas, *Cardiacnet, Segmentation of Left Atrium and Proximal Pulmonary Veins from MRI using Multi-View CNN*, MICCAI, Springer, New York, NY, USA, 2017.

[8] O. S. Kenneth, B. D' A. David, and G. A. Jason, "Hypercube-based encoding for evolving large-scale neural networks," *Artificial Life*, vol. 15, no. 2, pp. 185–212, 2009.

[9] Z. Barret and V. L. Quoc, "Neural architecture search with reinforcement learning," 2016, http://arxiv.org/abs/1611.01578.

[10] F. Chollet, "Keras," 2015, https://github.com/fchollet/keras.

[11] E. Andre, K. Brett, A Roberto et al., "Dermatologist-level classification of skin cancer with deep neural networks," *Nature*, vol. 542, no. 7639, pp. 115–118, 2017.

[12] M. Grewal, M. M. Srivastava, P. Kumar, and S. Varadarajan, "Radiologist level accuracy using deep learning for hemorrhage detection in CT scans," 2017, http://arxiv.org/abs/1710.04934.

[13] R. Pranav, Y. H. Awni, H. Masoumeh, B. Codie, and Y. N. Andrew, "Cardiologist-level arrhythmia detection with convolutional neural networks," 2017, http://arxiv.org/abs/1707.01836.

[14] G. Varun, P. Lily, C. Marc et al., "Development and validation of a deep learning algorithm for detection of diabetic retinopathy in retinal fundus photographs," *JAMA*, 2017, vol. 316, no. 22, pp. 2402–2410.

[15] P. Huang, S. Park, R. Yan et al., "Added value of computer-aided CT image features for early lung cancer diagnosis with small pulmonary nodules: a matched case-control study," *Radiology*, vol. 286, no. 1, pp. 286–295, 2017.

[16] P. Lakhani and B. Sundaram, "Deep learning at chest radiography: automated classification of pulmonary tuberculosis by using convolutional neural networks," *Radiology*, vol. 284, no. 2, pp. 574–582, 2017.

[17] F. D. Demner, M. D. Kohli, M. B. Rosenman et al., "Preparing a collection of radiology examinations for distribution and retrieval," *Journal of the American Medical Informatics Association*, vol. 23, no. 2, pp. 304–310, 2015.

[18] T. I. Mohammad, A. A. Md, T. M. Ahmed, and A. Khalid, "Abnormality detection and localization in chest x-rays using deep convolutional neural networks," 2017, http://arxiv.org/abs/1705.09850.

[19] Li. Yao, E. Poblenz, D. Dagunts, B. Covington, D. Bernard, and K. Lyman, "Learning to diagnose from scratch by exploiting dependencies among labels," 2017, http://arxiv.org/abs/1710.10501.

[20] W. Xiaosong, P. Yifan, L. Le, L. Zhiyong, B. Mohammadhadi, and M. S. Ronald, "Chest X-ray8: Hospital-scale chest X-ray database and benchmarks on weakly-supervised classification and localization of common thorax diseases," 2017, http://arxiv.org/abs/1705.02315.

[21] H. C. Shin, L. Lu, L. Kim, A. Seff, J. Yao, and R. M. Summers, "Interleaved text/image deep mining on a very large- scale radiology database," in *Proceedings of the Conference on Computer Vision and Pattern Recognition (CVPR)*, Boston, MA, USA, June 2015.

[22] H. C. Shin, L. Lu, L. Kim, A. Seff, J. Yao, and R. M. Summers, "Interleaved text/image deep mining on a large-scale radiology database for automated image interpretation," *Journal of Machine Learning Research*, vol. 17, no. 107, pp. 1–31, 2016.

[23] H. Boussaid and I. Kokkinos, "Fast and exact: ADMM-based discriminative shape segmentation with loopy part models," in *Proceedings of Conference on Computer Vision and Pattern Recognition (CVPR)*, Columbus, OH, USA, June 2014.

[24] U. Avni, H. Greenspan, E. Konen, M. Sharon, and J. Goldberger, "X-ray categorization and retrieval on the organ and pathology level, using patch-based visual words," *Med Imaging, IEEE Transactions*, vol. 30, no. 3, 2011.

[25] J. Melendez, G. B. Van, P. Maduskar et al., "A novel multiple-instance learning-based approach to computer-aided

detection of tuberculosis on chest x-ray," *IEEE Transactions on Medical Imaging*, vol. 34, no. 1, pp. 179–192, 2015.

[26] S. Jaeger, A. Karargyris, S. Candemir et al., "Automatic tuberculosis screening using chest radio-graphs," *IEEE Transactions on Medical Imaging*, vol. 33, no. 2, pp. 233–245, 2014.

[27] Z. Xue, D. You, S. Candemir et al., "Chest x-ray image view classification," in *Proceedings of the Computer-Based Medical Systems IEEE 28th International Symposium*, São Paulo, Brazil, June 2015.

[28] S. Hermann, "Evaluation of scan-line optimization for 3d medical image registration," in *Proceedings of Conference on Computer Vision and Pattern Recognition (CVPR)*, Columbus, OH, USA, June 2014.

[29] D. K. Kermany and M. Goldbaum, *Labeled Optical Coherence Tomography (OCT) and Chest X-Ray Images for Classification*, Mendeley Data, London, UK, 2018.

Hindawi
Journal of Healthcare Engineering
Volume 2019, Article ID 3845462, 8 pages
https://doi.org/10.1155/2019/3845462

Research Article

Using Kinect v2 to Control a Laser Visual Cue System to Improve the Mobility during Freezing of Gait in Parkinson's Disease

Amin Amini and Konstantinos Banitsas

College of Engineering Design and Physical Sciences, Department of Electronics and Computer Engineering, Brunel University London, London, UK

Correspondence should be addressed to Amin Amini; amin.amini@brunel.ac.uk

Received 19 November 2018; Revised 3 January 2019; Accepted 22 January 2019; Published 20 February 2019

Guest Editor: Heenam Yoon

Different auditory and visual cues have been proven to be very effective in improving the mobility of people with Parkinson's (PwP). Nonetheless, many of the available methods require user intervention and so on to activate the cues. Moreover, once activated, these systems would provide cues continuously regardless of the patient's needs. This research proposes a new indoor method for casting dynamic/automatic visual cues for PwP based on their head direction and location in a room. The proposed system controls the behavior of a set of pan/tilt servo motors and laser pointers, based on the real-time skeletal information acquired from a Kinect v2 sensor. This produces an automatically adjusting set of laser lines that can always be in front of the patient as a guideline for where the next footstep would be placed. A user interface was also created that enables users to control and adjust the settings based on the preferences. The aim of this research was to provide PwP with an unobtrusive/automatic indoor system for improving their mobility during a Freezing of gait (FOG) incident. The results showed the possibility of employing such system, which does not rely on the subject's input nor does it introduce any additional complexities to operate.

1. Introduction

Freezing of gait (FOG) is one of the most disabling symptoms in Parkinson's disease (PD) that affects its sufferers by impacting their gait performance and locomotion. FOG is an episodic phenomenon that introduces irregularities in the initiation or continuation of a patient's locomotion and usually occurs in later stages of PD where patients' muscles cannot function normally and appear to be still when they are trying to walk [1–4]. This makes FOG one of the most intolerable symptoms that not only affects PD sufferers physically but also psychologically, as it makes them almost completely dependent on others for their basic and daily tasks. Consequently, the patient's quality of life decreases, and the healthcare and treatment expenditures increase, as does the cost of the injuries caused [1]. It has been estimated that about 50% of PwP experience FOG incidents [5]. Moreover, it has been proven that visual and auditory cues can have a positive impact on the subject's gait performance during a FOG incident [6–8]. Visual cues such as laser lines can act as a sensory guidance trick that provides an external trigger, which, in turn, can initiate movement [7].

There has been much research conducted towards implementing apparatus and systems that can provide visual and auditory cues for PwP. In work done by Zhao et al. [9], a wearable system based on modified shoes was developed in order to cast a laser-based visual cue in front of PwP. The system consisted of a 3D printed add-on that included a red laser line projector and pressure sensors that detect the stance phase of a gait cycle and turn the laser pointer on. The unit provided the option to adjust the distance between the laser light strip and the subject's foot for the optimal effectiveness, depending on the user's preferences. The research provided a simple, yet effective approach towards providing visual cues for PwP with locomotion issues. Nonetheless, like any other approaches, this too has some limitations, such as the constant need to carry the shoe add-on, the batteries needed for the device, charging the batteries, and remembering to switch them on.

In another attempt [10], researchers evaluated the effect of visual cues using two different methods, including a subject-mounted light device (SMLD) and taped step length markers. It was concluded that using laser projections based on SMLD have promising effects on the PwP's locomotion and gait performance. The method required patients to wear a SMLD that some patients might find inconvenient to have or even impractical in some situations. Moreover, SMLD systems have stability issues and steadiness difficulties due to the subjects' torso movements during a gait cycle. As expected, the visual cues must be constantly enabled during a gait cycle, regardless whether they are needed or not.

In [11], although the SMLD method was employed, researchers added the 10 seconds on-demand option to the "constantly on" visual cue casting. This system was more sophisticated, consisting of a backpack having a remotely controllable laptop that made the subjects' mobility even more troublesome.

In other attempts [12, 13], a different approach was implemented by using virtual cues projected on a pair of goggles that is only visible to the patient. In [14], the effect of real and virtual visual cueing was compared, and it was concluded that real transverse lines casted on the floor are more impactful than the virtual counterparts. Nonetheless, using virtual cueing spectacles (VCS) eliminates the shortcomings in other techniques such as limitations in mobility, steadiness, and symmetry. VCS have also the advantage of being used in an external environment when the patient is out and about.

Moreover, several research studies have been conducted using virtual reality (VR) to assess the possibility of VR integration for Parkinson's related studies [15–20]. Nonetheless, as the VR technology blocks patients' view and makes them unable to see their surroundings, the usage of this is limited to either rehabilitation by implementing exercise-based games, FOG provoking scenarios, or the assessment of patients' locomotion rather than real-time mobility improvement using cues.

Although they are effective to some extent, these attempts tend to restrict the user either by forcing them to carry backpacks or wear vests containing electronics, or making them rely on conventional approaches such as attaching laser pointers to a cane [21], or laser add-on for shoes.

The hypothesis of this study, on the other hand, is to propose a different technique: casting parallel laser lines as a dynamic and automatic visual cuing system for PwP based on Kinect v2 and a set of servo motors suitable for indoor environments. As Kinect has been proven to be a reliable data feed source for controlling servo motors [22, 23], the Kinect camera was chosen for real-time depth data feed for this study. This paper also examines the possibility of using the Kinect v2 sensor for such purposes in terms of accuracy and response time.

This research uses subject's 3D Cartesian location and head direction as an input for servo motors to cast visual cues accordingly. This eliminates the need of the user intervention or trigger, and at the same time, the need to carry or wear any special equipment. Despite this approach being limited to environments equipped with the proposed apparatus, it does not require any attachments or reliance on PwP themselves, something that can be beneficial in many scenarios. The system comprises a Microsoft Kinect v2, a set of pant/tilt servo motors alongside a microcontroller based on Arduino Uno and two laser line laser pointers. A two-line projection was chosen so that the second traversed laser line could be used to indicate a set area for which the next step has to land. The system was tested in different conditions, including a partially occluded scene by furniture to simulate a living room.

2. Methods

During the initial testing phase, 11 healthy subjects were invited, consisting of both males and females ranging from ages 24–31, with the age mean of 27 and SD of 2.34, a mean height of 174.45 cm (68.68 inch) and SD of 8.31 cm (3.27 inch) ranging from 163 to 187 cm (64.17 to 73.62 inch). They were asked to walk in predefined paths: 12 paths per subject, walking towards the camera and triggering a simulated FOG incident by imitating the symptom while having the Kinect camera positioned at a fixed location. The subjects' skeletal data were captured and analyzed by the Kinect camera in real-time. The software was written in C# using the Kinect for Windows SDK version 2.0.1410.19000. The room that was used for conducting the experiments consisted of different pieces of living room furniture to mimic a practical-use case of the device. This not only yields more realistic results but also tests the system in real-life scenarios where the subject is partially visible to the camera and not all the skeletal joints are being tracked. To test and compare the Kinect v2's accuracy in determining both vertical and horizontal angles according to the subject's foot distance to the Kinect camera and body orientation, eight Vicon T10 cameras (considered as the gold standard) were also used to capture the subject's movements and compare those with the movements determined by the Kinect. The Vicon cameras and the Kinect v2 captured each session simultaneously while the frame rate of the recorded data from the Vicon cameras was down-sampled to match the Kinect v2 at approximately 30 frames per second.

At a later stage and following an ethical approval, there was a recruitment of 15 PwP (with the collaboration of Parkinson's UK) to test the system and provide feedback. This research was published separately in [22]. The more in-depth analysis and information with regard to this focus group can also be checked via [24].

2.1. Kinect RGB-D Sensor

2.1. Kinect RGB-D Sensor. Microsoft Kinect v2 is a time-of-flight (TOF) camera that functions by emitting infrared (IR) lights on objects, and upon reflection of the lights back to the IR receiver, it constructs a 3D map of the environment where the Z-axis is calculated via the delay of receiving IR light [25]. Kinect v2 introduced many features and improvements compared to its predecessor such as 1080p and 424p resolution at approximately 30 frames per seconds for its RGB and depth/IR streams, respectively, as well as a wider field of view [26]. The ability to track 25 joints of six subjects simultaneously enables researchers to employ Kinect v2 as an unobtrusive human motion tracking device in different disciplines, including rehabilitation and biomedical engineering.

2.2. Angle Determination. The Kinect v2 was used to determine the subjects' location in a 3D environment and localize the subject's feet joints to calculate the correct horizontal and vertical angles for servo motors. To determine the subject's location, Kinect skeletal data were used for joints' 3D coordinate acquisition. A surface floor can be determined by using the vector equation of planes. This is necessary to automate the process of calculating the Kinect's height to the floor that is one of the parameters in determining vertical servo angle:

$$Ax + By + Cz + D = 0, \tag{1}$$

where A, B, and C are the components of a normal vector that is perpendicular to any vector in a given plane and D is the height of the Kinect from the levelled floor. x, y, and z are the coordinates of the given plane that locates the floor of the viewable area and are provided by the Kinect SDK. Ax, By, Cz, and D are also provided by the Kinect SDK once a flat floor is detected by the camera.

For vertical angle determination, a subject's 3D feet coordinates were determined, and depending on which foot was closer to the Kinect in the Z-axis, the system selects that foot for further calculations. Once the distance of the selected foot to the camera was calculated, the vertical angle for the servo motor is determined using the Pythagorean theorem, as depicted in Figure 1. The subject's skeletal joints' distance to the Kinect on the Z-axis is defined in a right-handed coordinate system, where the Kinect v2 is assumed to be at origin with a positive Z-axis value increasing in the direction of Kinect's point of view.

In Figure 1, a is the Kinect's camera height to the floor that is the same as variable D from equation (1) and c is the hypotenuse of the right triangle, which is the subject's selected foot distance to the Kinect camera in the Z-axis. θ is the calculated vertical angle for the servo motor. Note that we have considered the position offsets in the X and Y axes between the Kinect v2 camera and the laser pointers/servo motors in order to have the most accurate visual cue projection.

Our experiments showed that the Kinect v2 determines a joint's Z-axis distance to the camera by considering its Y-axis value; i.e., the higher the value of a joint's Y-axis is to the camera's optical center, the further the distance it has to the camera in the Z-axis. This indicates that unlike the Kinect's depth space, the Kinect skeletal coordinate system does not calculate Z-axis distance (Figure 1, variable c) in a perpendicular plane to the floor, and as a result, the height of the points, that in this case are joints, are also taken into consideration.

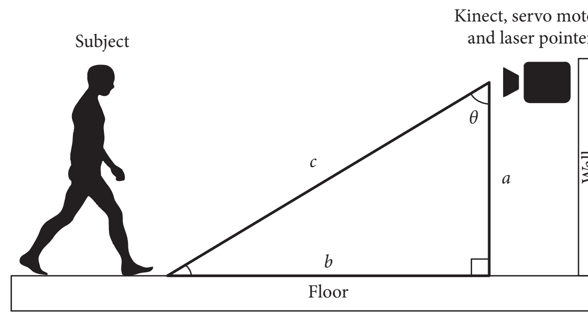

FIGURE 1: Vertical angle determination.

In case of a joint being obstructed by an object, for example, a piece of furniture, the obstructed joints' 3D Cartesian coordinate location tracking was compensated and predicted using "inferred" state enumerate, a built-in feature in the Kinect SDK. By implementing the "inferred" joint state, a joint data was calculated, and its location was estimated based on other tracked joints and its previously known location.

Figure 2 shows the Kinect v2 accuracy in determining a subject's joint (left foot) distance to the camera in Z-axis compared to a gold standard motion capture device (Vicon T10). It was concluded that Kinect v2 skeletal data acquisition accuracy was very close (98.09%) to the industry standard counterpart. The random noise artifacts in the signal were not statistically significant and did not affect the vertical angle determination.

The subject's body direction that determines the required angle for the horizontal servo motor can be yielded through the calculation of rotational changes of two subject's joints including left and right shoulders. The subject's left and right shoulder joints' coordinates were determined using skeletal data and then fed to an algorithm to determine the body orientation as follows:

$$\text{servo angle} = \left|90 \pm \left(\sin^{-1}\left|\text{shoulder}A - \text{shoulder}B\right|\right)\right|. \tag{2}$$

In Figure 3, d is the Z-axis distance difference to the camera between the subject's left and right shoulders.

Once d based in the equation (2) was calculated, the angle for the horizontal servo motor can be determined by calculating the inverse sine of θ. Depending on whether the subject is rotating to the left or right, the result would be subtracted or added from/to 90, respectively, as the horizontal servo motor should rotate in reverse in order to cast laser lines in front of the subject accordingly.

2.3. FOG Detection. In previous studies, the authors have implemented the process of FOG detection in [27] using the gait cycle and walking pattern detection techniques [26, 28]. Once the developed system detects a FOG incident, it will turn the laser pointers on and start determining the appropriate angles for both vertical and horizontal servo motors. After passing a user-defined waiting threshold or disappearance of the FOG incident characteristics, the system returns to its monitoring phase by turning off the

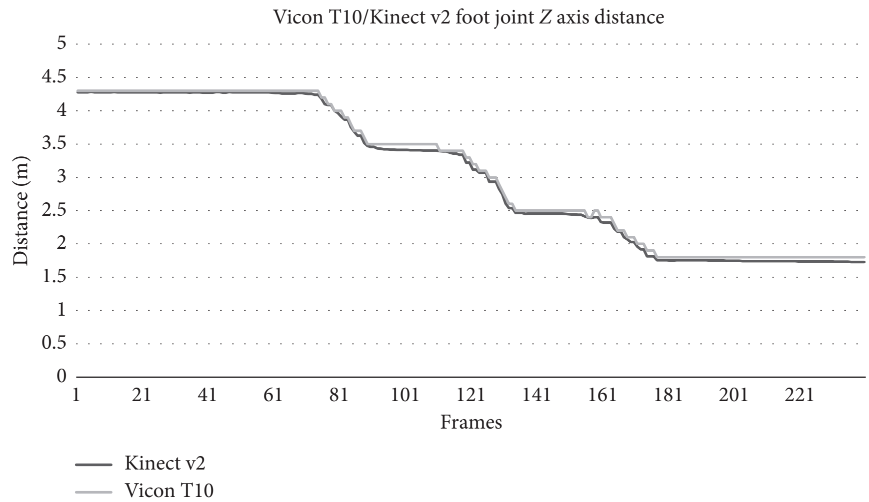

Figure 2: Subject's left foot distance to the camera in Z-axis using Kinect v2 and Vicon T10.

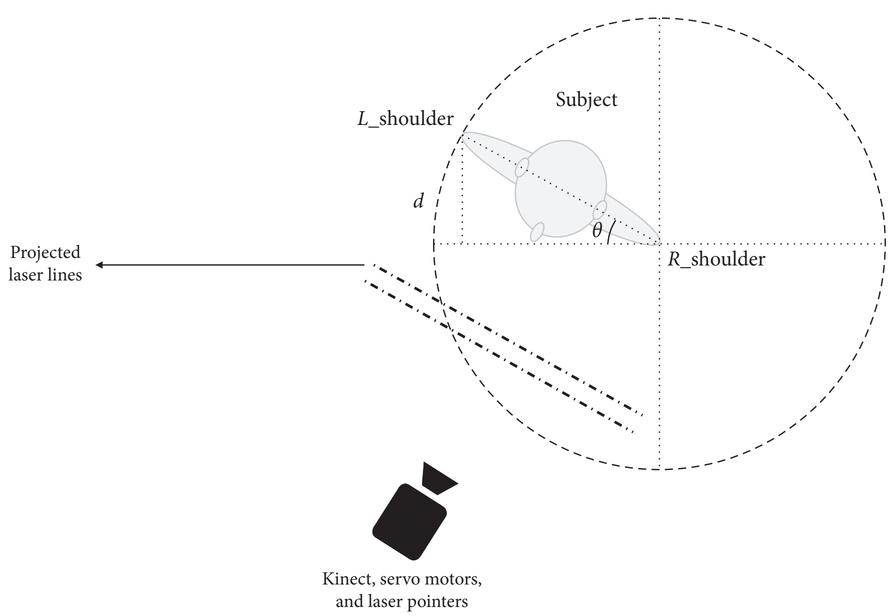

Figure 3: Horizontal angle determination (note that Kinect sees a mirrored image thus shoulders are reversed).

laser project and servo motors movements. Figure 4 shows the GUI for the developed system application.

The left image shows a Parkinson's disease patient imitator during his FOG incident. The right window shows that the subject is being monitored, and his gait information is being displayed to healthcare providers and doctors. As it can be seen in the "FOG Status" section displayed in the bottom rectangle, the system has detected a FOG incident and activated the laser projection system to be used as a visual cue stimulus. The circled area shows the projection of laser lines in front of the subjects (according to the distance from their feet to the camera) and their body direction. The developed system also allows further customization, including visual cue distance adjustments in front of the patient.

2.4. Serial Connection. A serial connection was needed to communicate with the servo motors controlled by the Arduino Uno microcontroller. The transmitted signal by the developed application needed to be distinguished at the receiving point (the Arduino microcontroller), so each servo motor can act according to its intended angle and signal provided. We have developed a multipacket serial data transmission technique similar to [29]. The data was labeled at the transmitter side, so the microcontroller can distinguish and categorize the received packet and send appropriate signals to each servo motor. The system loops through this cycle of horizontal angle determination every 150 ms. This time delay was chosen as the horizontal servo motor does not need to be updated in real-time due to the fact that a subject is less likely to change his/her direction in very short

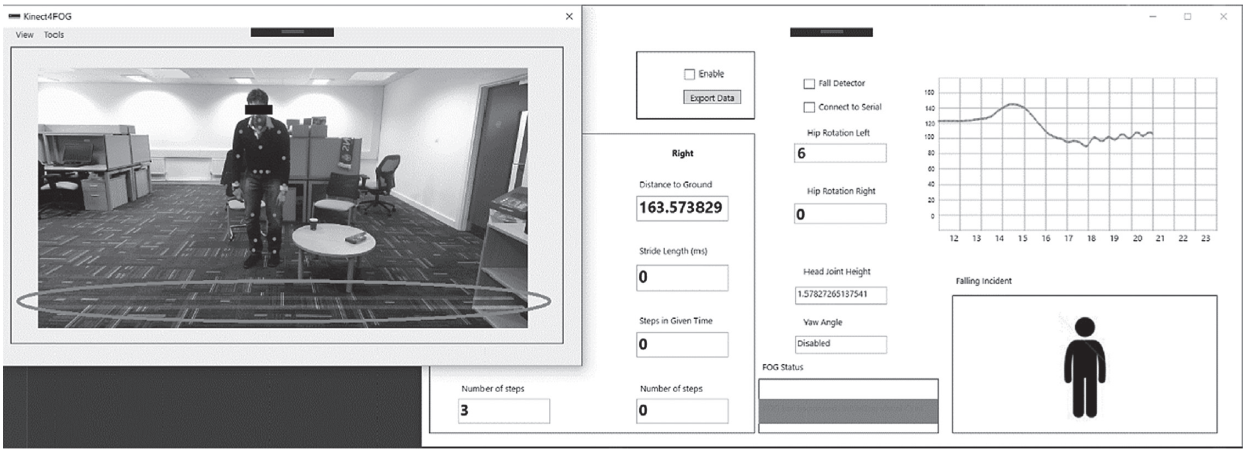

Figure 4: Graphical user interface for the developed software.

intervals. This ensures less jittery and smoother movements of horizontal laser projection. The vertical servo motor movement was less prone to the jitters as the subject's feet are always visible to the camera as long as they are not obstructed by an object.

2.5. Design of the Prototype System. A two-servo system was developed using an Arduino Uno microcontroller and two class-3B 10 mW 532 nm wavelength green line laser projectors as shown in Figure 5(a); green laser lines have been proven to be most visible amongst other laser colors used as visual cues [30]. A LCD display has also been added to the design that shows all the information with regard to vertical and horizontal angles to the user. Figure 5(a) shows the laser line projection system attached to the tilt/pan servo motors. Figure 5(b) shows the top view of the prototype system including the wiring and voltage regulators. Figure 5(c) shows the developed prototype system used in the experiment at different angles including the Kinect v2 sensor, pan/tilt servo motors, laser pointers, and the microcontroller.

3. Results

Figure 6 demonstrates the calculated vertical angle based on the subjects' feet/joint distance to the Kinect camera in Z-axis. The right foot has been omitted in the graph for simplicity.

As Figure 6 demonstrates, the system provided highly accurate responses based on the subject's foot distance to the camera in Z-axis and the vertical servo motor angle.

Subjects were also asked to rotate their body in front of the Kinect camera to test the horizontal angle determination algorithm, and as a result, the horizontal servo motor functionality. Figure 7 shows the result of the calculated horizontal angle using equation (2) for the left and right directions.

Figure 7 shows how the system reacts to the subject's body orientation. Each subject was asked to face the camera in a stand-still position while rotating their torso to the left and to the right in turns. As mentioned before, the horizontal angle determination proved to be more susceptible to noise compared to the vertical angle calculation. This is due to the fact that as the angle increases to more than 65 degrees, the shoulder farthest away would be obstructed by the nearer shoulder, and as a result, the Kinect should compensate by approximating the position of that joint. Nonetheless, this did not have any impact on the performance of the system.

Overall, the entire setup including the Kinect v2 sensor, tilt/pan servo motors, laser projectors, microcontroller, and LCD except the controlling PC will cost about £137.00, making it much more affordable than other less capable alternatives available on the market.

4. Discussion

A series of pan/tilt servo motors have been used alongside laser line projectors to create a visual cuing system, which can be used to improve the mobility of PwP. The use of the system eliminates the need to carry devices, helping patients to improve their mobility by providing visual cues. The implemented system has the ability to detect FOG using only the Kinect camera, i.e., fully unobtrusive, and provide dynamic and automatic visual cues projection based on the subject's location without the patient's intervention as opposed to other methods mentioned. It was observed that this system can provide an accurate estimation of the subject's location and direction in a room and cast visual cues in front of the subject accordingly. The Kinect's effective coverage distance was observed to be between 1.5 and 4 meters (59 and 157.48 inch) form the camera, which is within the range of the area of most living rooms, making it an ideal device for indoor rehabilitation and monitoring purposes. To evaluate the Kinect v2's accuracy in calculating the vertical and horizontal angles, a series of eight Vicon T10 cameras were also used as a golden standard. Overall, the system proved to be a viable solution for automatic and unobtrusive visual cues' apparatus. Nonetheless, there are some limitations to this approach including the indoor aspect of it and the fact that it requires the whole setup including the Kinect, servos, and laser projectors to be included in the most communed areas of a house such as the living room and the kitchen.

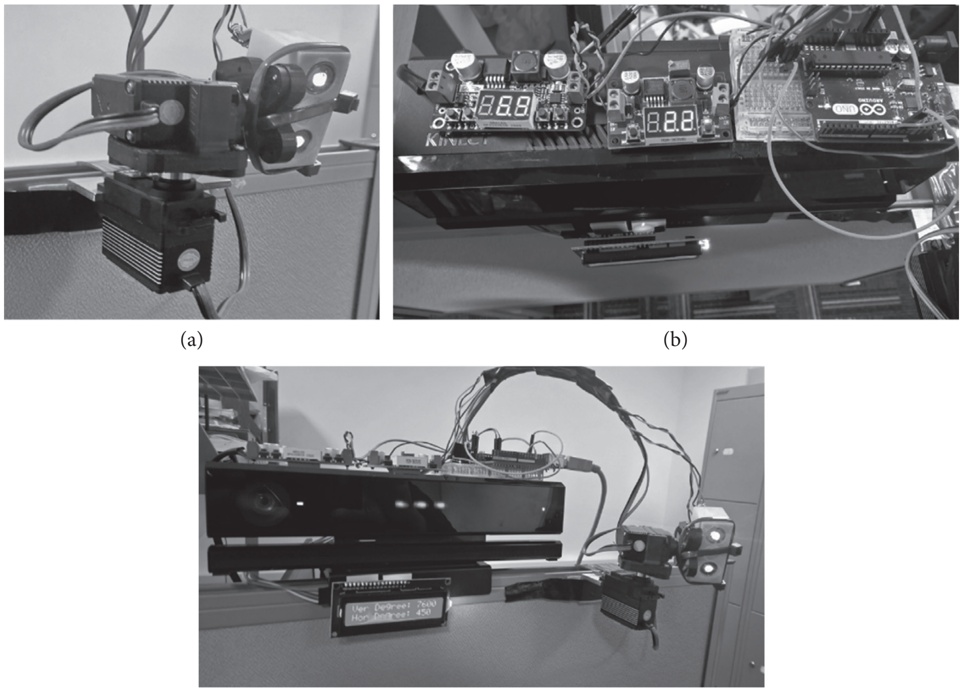

(a) (b) (c)

Figure 5: The developed prototype of the automatic visual cue system. (a) The two step motors controlling the horizontal and vertical alignment of the system. (b) A top view of the Kinect v2 combined with the microcontroller and voltage regulators. (c) A view of the prototype system in action.

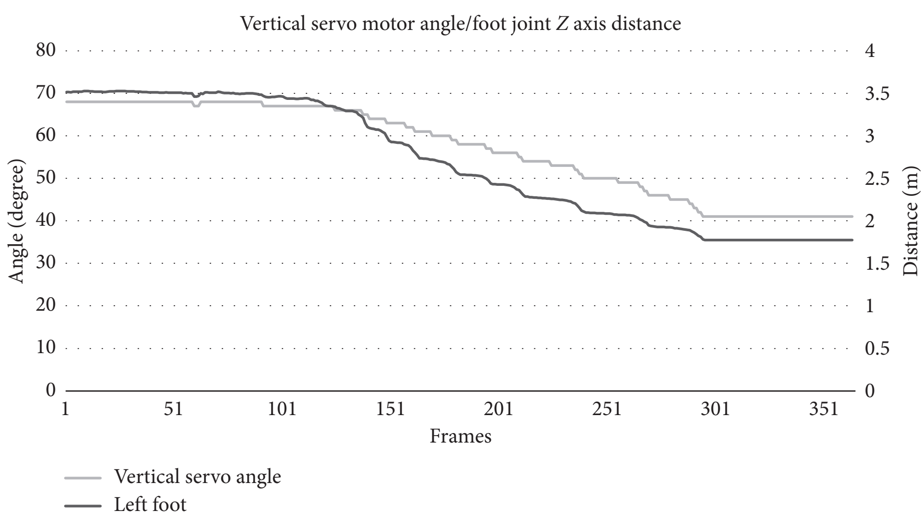

Figure 6: Vertical servo motor angle in relation to the subject's foot joint distance to the Kinect camera in Z-axis.

Additionally, during the experimentation, the Kinect's simultaneous subject detection was limited to only one person. Nevertheless, Kinect v2 is capable to detect six simultaneous subjects in a scene. However, the laser projection system, in order to work properly, should only aim at one person at a time. The developed system has the ability to either lock on the first person that comes into the coverage area or distinguish the real patient based on the locomotion patterns and ignore other people. Despite that, the affordability and ease of installation of the system would still make it a desirable solution should more than one setup need to be placed in a house. Moreover, the use of a single Kinect would limit the system's visibility and visual cue projection as well.

5. Conclusion

The results of this research showed a possibility of implementing an automatic and unobtrusive FOG monitoring and mobility improvement system, while being reliable and accurate at the same time. The system's main advantages such as real-time patient's monitoring, improved locomotion and patient's mobility, and unobtrusive

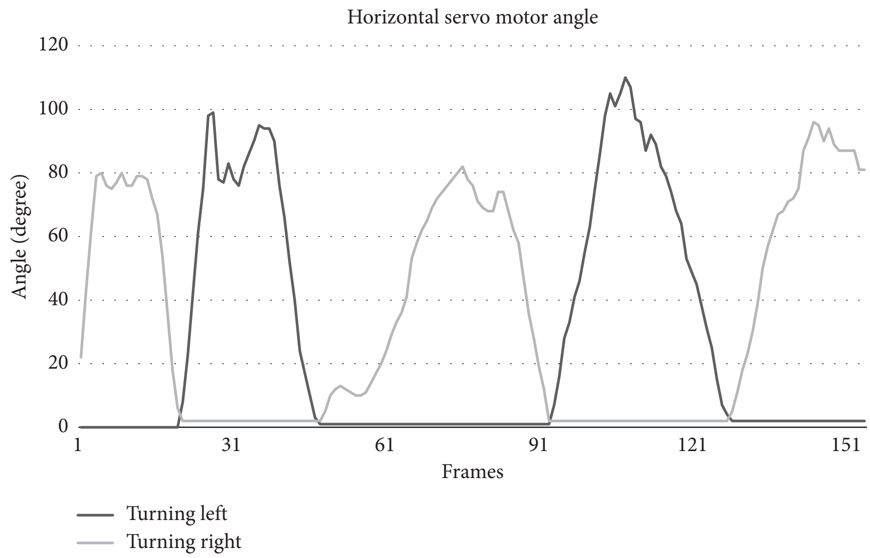

FIGURE 7: Horizontal servo motor angle changes according to the subject's body orientation and direction during a test.

and dynamic visual cue projection make it, in overall, a desirable solution that can be further enhanced for future implementations.

As a next step, one could improve the system's coverage with a series of this implemented system to be installed in PwP's houses to cover most of the communal areas, or areas where a patient experiences the FOG the most (i.e., narrow corridors). One could also investigate the possibility of using such systems attached to a circular rail on a ceiling that can rotate and move according to the patient's location; this removes the need for extra setup in each room as the system can cover some additional areas. Moreover, by coupling the system with other available solutions such as laser-mounted canes or shoes, patients can use the implemented system when they are at home, while using other methods for outdoor purposes. This requires integration at different levels such as a smartphone application and visual cues in order for these systems to work as intended. Finally, the system's form factor can be made smaller to some extent by removing the Kinect's original casing and embedding all the equipment in a customized 3D printed enclosure, which makes it more suitable for a commercial production.

Data Availability

The gait analysis data used to support the findings of this study are restricted by the Brunel University London Ethics Committee in order to protect patient privacy. Data are available from CEDPS-Research@brunel.ac.uk for researchers who meet the criteria for access to confidential data.

Conflicts of Interest

The authors claim no conflicts of interest in the subject matter or materials discussed in this manuscript.

References

[1] B. R. Bloem, J. M. Hausdorff, J. E. Visser, and N. Giladi, "Falls and freezing of gait in Parkinson's disease: a review of two interconnected, episodic phenomena," *Movement Disorders*, vol. 19, no. 8, pp. 871–884, 2004.

[2] S. Donovan, C. Lim, N. Diaz et al., "Laserlight cues for gait freezing in Parkinson's disease: an open-label study," *Parkinsonism & Related Disorders*, vol. 17, no. 4, pp. 240–245, 2011.

[3] Y. Okuma, "Freezing of gait in Parkinson's disease," *Journal of Neurology*, vol. 253, no. S7, pp. vii27–vii32, 2006.

[4] L. V. Kalia and A. E. Lang, "Parkinson's disease," *The Lancet*, vol. 386, no. 9996, pp. 896–912, 2015.

[5] S. Choi, H. Jung, G. Yoon, and B. C. Kim, "Factors associated with freezing of gait in patients with Parkinson's disease," *Neurological Sciences*, vol. 40, no. 2, pp. 293–298, 2018.

[6] P. Ginis, E. Nackaerts, A. Nieuwboer, and E. Heremans, "Cueing for people with Parkinson's disease with freezing of gait: a narrative review of the state-of-the-art and novel perspectives," *Annals of Physical and Rehabilitation Medicine*, vol. 61, no. 6, pp. 407–413, 2018.

[7] A. Nieuwboer, "Cueing for freezing of gait in patients with Parkinson's disease: a rehabilitation perspective," *Movement Disorders*, vol. 23, no. S2, pp. S475–S481, 2008.

[8] P. A. Rocha, G. M. Porfírio, H. B. Ferraz, and V. F. M. Trevisani, "Effects of external cues on gait parameters of Parkinson's disease patients: a systematic review," *Clinical Neurology and Neurosurgery*, vol. 124, pp. 127–134, 2014.

[9] Y. Zhao, S. Ramesberger, U. M. Fietzek, L. T. D'Angelo, and T. C. Luth, "A novel wearable laser device to regulate stride length in Parkinson's disease," in *Proceedings of 35th Annual International Conference of the IEEE Engineering in Medicine and Biology Society (EMBC)*, pp. 5895–5898, Osaka, Japan, July 2013.

[10] G. N. Lewis, W. D. Byblow, and S. E. Walt, "Stride length regulation in Parkinson's disease: the use of extrinsic, visual cues," *Brain*, vol. 123, no. 10, pp. 2077–2090, 2000.

[11] R. Velik, U. Hoffmann, H. Zabaleta, J. Félix, M. Massó, and T. Keller, "The effect of visual cues on the number and

duration of freezing episodes in Parkinson's patients," in *Proceedings of 2012 Annual International Conference of the IEEE Engineering in Medicine and Biology Society*, pp. 4656–4659, San Diego, CA, USA, September 2012.

[12] T. A. Kaminsky, B. J. Dudgeon, F. F. Billingsley, P. H. Mitchell, and S. J. Weghorst, "Virtual cues and functional mobility of people with Parkinson's disease: a single-subject pilot study," *Journal of Rehabilitation Research and Development*, vol. 44, no. 3, pp. 437–448, 2007.

[13] J. McAuley, P. Daly, and C. Curtis, "A preliminary investigation of a novel design of visual cue glasses that aid gait in Parkinson's disease," *Clinical Rehabilitation*, vol. 23, no. 8, pp. 687–695, 2009.

[14] H. J. Griffin, R. Greenlaw, P. Limousin, K. Bhatia, N. P. Quinn, and M. Jahanshahi, "The effect of real and virtual visual cues on walking in Parkinson's disease," *Journal of Neurology*, vol. 258, no. 6, pp. 991–1000, 2011.

[15] M. Gilat, J. M. Shine, S. J. Bolitho et al., "Variability of stepping during a virtual reality paradigm in Parkinson's disease patients with and without freezing of gait," *PLoS One*, vol. 8, no. 6, Article ID e66718, 2013.

[16] A. C. Lo, V. C. Chang, M. A. Gianfrancesco, J. H. Friedman, T. S. Patterson, and D. F. Benedicto, "Reduction of freezing of gait in Parkinson's disease by repetitive robot-assisted treadmill training: a pilot study," *Journal of Neuro-Engineering and Rehabilitation*, vol. 7, no. 1, p. 51, 2010.

[17] A. Mirelman, I. Maidan, and J. E. Deutsch, "Virtual reality and motor imagery: promising tools for assessment and therapy in Parkinson's disease," *Movement Disorders*, vol. 28, no. 11, pp. 1597–1608, 2013.

[18] V. Robles-García, Y. Corral-Bergantiños, N. Espinosa et al., "Effects of movement imitation training in Parkinson's disease: a virtual reality pilot study," *Parkinsonism & Related Disorders*, vol. 26, pp. 17–23, 2016.

[19] M. I. R. Severiano, B. S. Zeigelboim, H. A. G. Teive, G. J. B. Santos, and V. R. Fonseca, "Effect of virtual reality in Parkinson's disease: a prospective observational study," *Arquivos de Neuro-Psiquiatria*, vol. 76, no. 2, pp. 78–84, 2018.

[20] D. Yelshyna, M. F. Gago, E. Bicho et al., "Compensatory postural adjustments in Parkinson's disease assessed via a virtual reality environment," *Behavioural Brain Research*, vol. 296, pp. 384–392, 2016.

[21] K. Swim, *The Effect of a Laser Guided Cane on Stride Length in Patients with Parkinson's Disease*, University of Toledo, Toledo, OH, USA, 2010.

[22] A. Amini, K. Banitsas, and W. R. Young, "Kinect4FOG: monitoring and improving mobility in people with Parkinson's using a novel system incorporating the Microsoft Kinect v2," *Disability and Rehabilitation: Assistive Technology*, pp. 1–8, 2018.

[23] F. Foroughi and P. Zong, "Controlling servo motor angle by exploiting Kinect SDK," *International Journal of Computer Applications*, vol. 116, no. 18, pp. 1–6, 2015.

[24] A. Amini, *Using 3D sensing and projecting technology to improve the mobility of Parkinson's disease patients*, Ph.D. thesis, Brunel University London, London, UK, 2018.

[25] A. Corti, S. Giancola, G. Mainetti, and R. Sala, "A metrological characterization of the Kinect v2 time-of-flight camera," *Robotics and Autonomous Systems*, vol. 75, pp. 584–594, 2016.

[26] A. Amini, K. Banitsas, and J. Cosmas, "A comparison between heuristic and machine learning techniques in fall detection using Kinect v2," in *Proceedings of 2016 IEEE International Symposium on Medical Measurements and Applications (MeMeA)*, pp. 1–6, Benevento, Italy, May 2016.

[27] A. A. M. Bigy, K. Banitsas, A. Badii, and J. Cosmas, "Recognition of postures and freezing of gait in Parkinson's disease patients using Microsoft Kinect sensor," in *Proceedings of 7th International IEEE/EMBS Conference on Neural Engineering (NER)*, pp. 731–734, Montpellier, France, April 2015.

[28] A. Amini, K. Banitsas, and S. Hosseinzadeh, "A new technique for foot-off and foot contact detection in a gait cycle based on the knee joint angle using Microsoft Kinect v2," in *Proccedings of 2017 IEEE EMBS International Conference on Biomedical & Health Informatics (BHI)*, pp. 153–156, Orland, FL, USA, February 2017.

[29] B. Evans, *Beginning Arduino Programming*, Apress, Berkeley, CA, USA, 2011.

[30] L. Bunting-Perry, M. Spindler, K. M. Robinson, J. Noorigian, H. J. Cianci, and J. E. Duda, "Laser light visual cueing for freezing of gait in Parkinson disease: a pilot study with male participants," *Journal of Rehabilitation Research and Development*, vol. 50, no. 2, pp. 223–230, 2013.

Hindawi
Journal of Healthcare Engineering
Volume 2019, Article ID 8936121, 8 pages
https://doi.org/10.1155/2019/8936121

Research Article

Development of a Wireless Health Monitoring System for Measuring Core Body Temperature from the Back of the Body

Qun Wei[1], **Hee-Joon Park**[1] **and Jyung Hyun Lee**[2]

[1]*Department of Biomedical Engineering, School of Medicine, Keimyung University, Daegu, Republic of Korea*
[2]*Department of Biomedical Engineering, School of Medicine, Kyungpook National University, Kyungpook National University Hospital, Daegu, Republic of Korea*

Correspondence should be addressed to Jyung Hyun Lee; pung@knu.ac.kr

Received 16 August 2018; Revised 26 November 2018; Accepted 27 December 2018; Published 17 February 2019

Guest Editor: Hyun Jae Baek

In this paper, a user-friendly and low-cost wireless health monitoring system that measures skin temperature from the back of the body for monitoring the core body temperature is proposed. To measure skin temperature accurately, a semiconductor-based microtemperature sensor with a maximum accuracy of ±0.3°C was chosen and controlled by a high-performance/low-power consumption Acorn-Reduced Instruction Set Computing Machine (ARM) architecture microcontroller to build the temperature measuring device. Relying on a 2.4 GHz multichannel Gaussian frequency shift keying (GFSK) RF communication technology, up to 100 proposed temperature measuring devices can transmit the data to one receiver at the same time. The shell of the proposed wireless temperature-measuring device was manufactured via a 3D printer, and the device was assembled to conduct the performance tests and *in vivo* experiments. The performance test was conducted with a K-type temperature sensor in a temperature chamber to observe temperature measurement performance. The results showed an error value between two devices was less than 0.1°C from 25 to 40°C. For the *in vivo* experiments, the device was attached on the back of 10 younger male subjects to measure skin temperature to investigate the relationship with ear temperature. According to the experimental results, an algorithm based on the curve-fitting method was implemented in the proposed device to estimate the core body temperature by the measured skin temperature value. The algorithm was established as a linear model and set as a quadratic formula with an interpolant and with each coefficient for the equation set with 95% confidence bounds. For evaluating the goodness of fit, the sum of squares due to error (SSE), R-square, adjusted R-square, and root mean square error (RMSE) values were 33.0874, 0.0212, 0.0117, and 0.3998, respectively. As the experimental results have shown, the mean value for an error between ear temperature and estimated core body temperature is about ±0.19°C, and the mean bias is 0.05 ± 0.14°C when the subjects are in steady status.

1. Introduction

Health monitoring has always been an important topic in biomedical-engineering research. Body temperature is one of the important numerical values to indicate human health status. The normal body temperature range is typically stated as 36.5 to 37.5°C [1]. The individual body temperature depends on age, exertion, infection, sex, and the place of the body at which the measurement is made [2]. Rectal measurement, oral measurement, and axillary measurement are the well-known methods for human body temperature measurements [3]. However, each method has disadvantages when performing the measurements. The thermometers can break if bitten when doing oral measurement, the rectum could be injured when doing rectal measurements, and the thermometer may need to be left in a place for a long time in order to obtain an accurate measurement. Therefore, the ear thermometer, which measures the temperature of the eardrum, and forehead thermometer, placed on the forehead of the subject to measure the body temperature, were developed. Both methods use infrared sensors to measure temperature, which is different from the mercurial thermometers and standard platinum resistance thermometers used in oral, rectal, and axillary measurements. The infrared thermometer is good for surface temperature measurement and is compact, lightweight, and easy to use. However, the environment needs to be clean, be without dust, and has high humidity. Also, the sensor is expensive, which will raise costs [4, 5].

Recently, because electronic engineering technology is developing rapidly, studies using various electrical devices focused on measuring skin properties objectively, such as measuring and analysis of skin electrical impedance and observing the effects of current, ionic strength, and temperature on the electrical properties of skin [6–11]. However, none of these researches have focused on skin temperature measurement; also, no studies have been conducted to find a relationship with core body temperature. Meanwhile, many medical researchers try to find the relationship between skin temperature and core body temperature for developing a new approach to measure core body temperature by noninvasive methods [12–14]. Researches such as Niedermann et al. have developed an algorithm to predict the core body temperature using the skin temperature measured from the chest. However, the study only used highly professional equipment that is not suitable for longer-term continuous monitoring of subjects in natural habitats or daily environment, so the limited resource is not suitable to develop a complete algorithm to predict the core body temperature.

Lately, Woo et al. proposed a patch-type device that attaches to the skin over the clavicle for measuring skin temperature and humidity and thus to predict the body temperature [15]. The researchers studied the relationship between perspiration rate and skin temperature and used the data to estimate the body temperature. However, the position for affixing the device was not suitable for long-term use, and the study reported the temperature error between the commercial device, and the proposed patch was larger than 15%.

In this study, a semiconductor sensor-based wireless health monitoring system for measuring core body temperature is proposed. Unlike past measuring approaches, the proposed wireless temperature-measuring device is attached on the skin surface of the back under the neck, as this part of the body has thin layers of fat and muscle and so the skin temperature here is more approximate to the core body temperature. Also, the location is suitable for comfortably attaching the device to the body for longer durations. A highly accurate temperature sensor and a high-performance/low-power consumption ARM architecture microcontroller were used to develop the wireless temperature-measuring device for the skin temperature measurements. The measured data were transmitted to the receiver using a multichannel Industrial, Scientific, and Medical (ISM) band 2.4 GHz GFSK RF communication method. An algorithm was developed based on the curve-fitting method to estimate the core body temperature according to the skin temperature value. The proposed system was manufactured, and performance tests and *in vivo* experiments were conducted to confirm system performance.

2. Methods

Figure 1 shows the basic idea for the proposed wireless health monitoring system composed of two parts: a wireless temperature-measuring device that is attached to the back of the body for measuring skin temperature and a receiver device for acquiring the data from the transmitter and sending the data to a computer for display and recording. In developing the wireless temperature-measuring device, a semiconductor-based microtemperature sensor, Si7021 (Silicon Labs, USA), was chosen as the sensing device for skin temperature measurement. This sensor has a small measurement error of approximately ±0.4°C at 1 Hz sampling rate in temperature measurement; this contributes to measuring skin temperature accurately with low power consumption. The EFM32WG 32-bit microprocessor (Silicon Labs, USA) was designed as the main controller for the device. This microcontroller unit (MCU) family, based on the ARM Cortex-M4 core, provides a full digital signal processing (DSP) instruction set and includes a hardware floating point unit (FPU) for faster computational performance. Also, it features up to 256 kB of flash memory, 32 kB of RAM, and CPU speeds up to 48 MHz, which are suitable to estimate the core body temperature in real time by embedding the algorithm. In addition, to minimize energy consumption, intelligent peripherals enable this MCU to control the device with high efficiency and longer battery life. In this research, the nRF24L01 (Nordic Semiconductor, Norway) transceiver was chosen to achieve wireless communication between transmitter and receiver. The transceiver is an ultralow-power 2 Mbps transceiver IC for the 2.4 GHz ISM band. The multireceiver technology that enables the receiver can communicate with a maximum of 128 transmitters simultaneously.

In designing the receiver, C8051F996 (Silicon Labs, USA), an ultralow-power MCU, was chosen to control the receiver. A highly integrated USB-to-UART bridge controller CP2102 (Silicon Labs, USA) was used inside the receiver for connecting the receiver to a computer easily. CP2102 has a simple solution for updating UART designs to USB using a minimal of components, and the printed circuit board (PCB) is an important reason to use this chip for connecting the receiver to a computer by a USB connection. The data are displayed and recorded on the computer by a developed LabVIEW program.

3. Experiments

3.1. System Manufacture. Figure 2 shows the manufactured PCBs of the proposed wireless temperature-measuring device: one is the main board (front and back views) for mounting the MCU and the wireless communication components and the other is the sensor board with temperature sensor components. The wireless temperature-measuring device had to be designed as small as possible to make it easy to attach to the back of the body. Therefore, all the PCBs were manufactured with four-layer structures, and all the components were chosen with surface-mounted device- (SMD-) type size 2012 mounted on both sides of the PCB to minimize the PCB size. A mini-USB port was fixed on the top of the PCB for connecting to the USB adapter for battery recharging. In addition, a chip shape 2.4 GHz antenna was fixed on the top of the main PCB and kept away

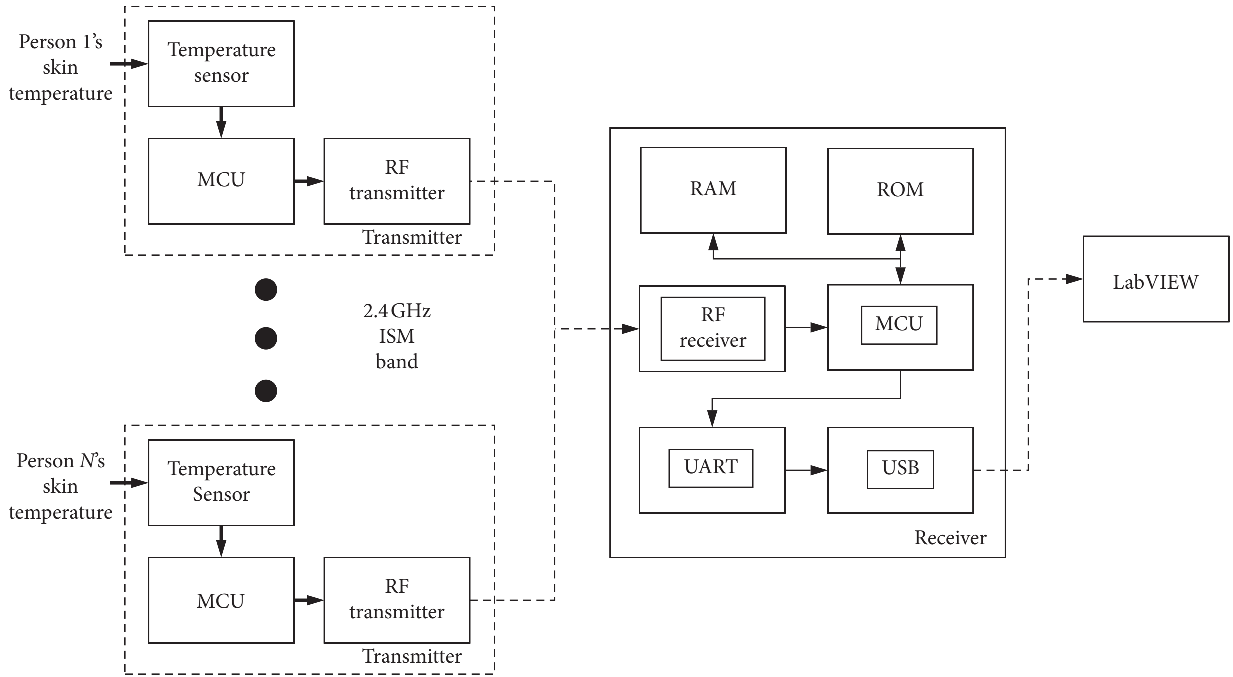

Figure 1: Block diagram showing the basic idea of the proposed wireless health monitoring system.

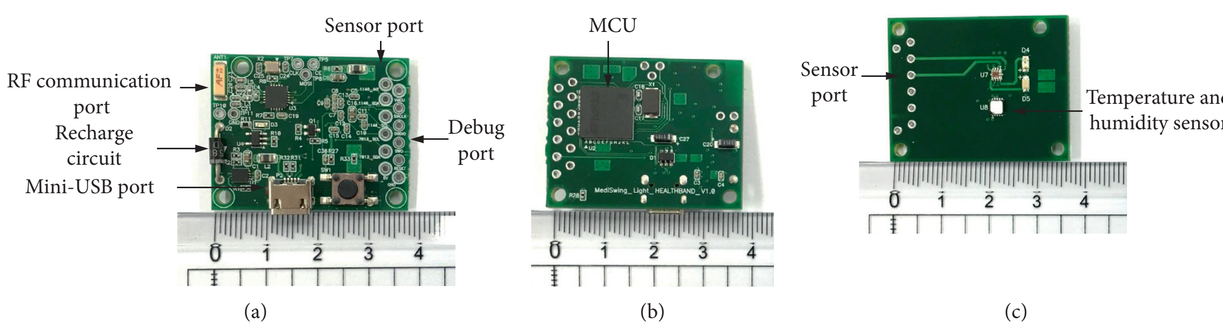

Figure 2: Manufactured PCBs for the wireless temperature-measuring device: (a) front view of the main board; (b) back view of the main board; (c) sensor board.

from the MCU to prevent the electrical effect from the electronic components, which would reduce the performance of the wireless communication. The temperature sensor was designed on the other PCBs for attaching securely to the back of the body. Guide holes were designed on the same side of the two PCBs for connecting the sensor board to the main board easily. The dimensions of each PCB are 38 mm × 30 mm × 10 mm.

Figure 3 shows the shell design in the 3D mode for the proposed wireless temperature-measuring device, and the device assembly with the manufactured shell. The shell dimensions are 40 mm × 30 mm × 17 mm and separated into two storage spaces: the upper space for attaching the main PCB and the bottom space designed as storage for a rechargeable battery and sensor PCB. The upper shell was designed with a power switch hole and USB porthole. Also, a porthole was designed on the bottom cover, which enabled the sensor to contact the skin of the back directly and completely. In addition, a 450 mAh size with 40 mm × 40 mm × 2 mm size rechargeable battery was chosen for the power supply. The shell was manufactured by 3D printer with polylactic acid (PLA) material that is known to be harmless to humans.

3.2. Experiments for the System Performance Test

3.2.1. Temperature Measurement Performance Test for the Wireless Temperature-Measuring Device. The manufactured wireless temperature-measuring device was situated in a temperature and humidity chamber (T2, YMRTC) for testing the performance of the measuring temperature as shown in Figure 4(a). The temperature in the chamber was set at an initial state of 25°C and increased by 5°C every 30 minutes, up to 40°C, a range similar to human skin temperature. Because of the temperature sensor for the chamber was at the top of the chamber, the temperature value on the chamber display was not suitable for comparing

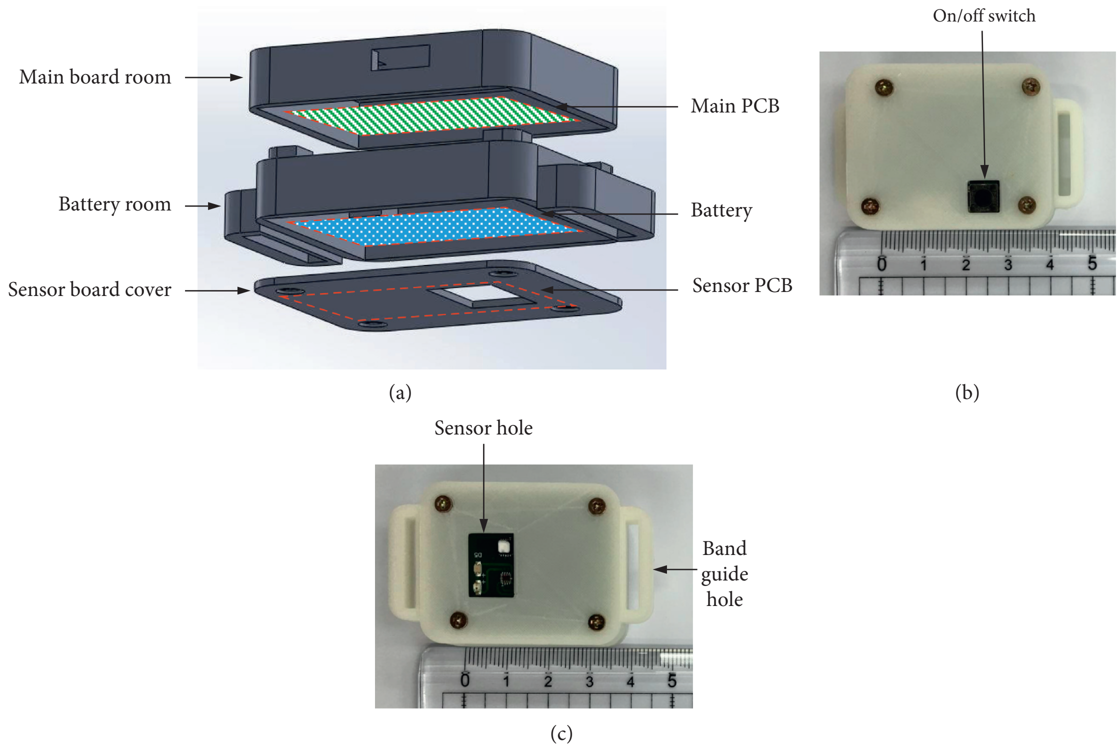

Figure 3: Photos of the shell for the proposed wireless temperature-measuring device: (a) 3D model of the shell structure; (b) top view of the assembled wireless temperature-measuring device; (c) bottom view of the assembled device.

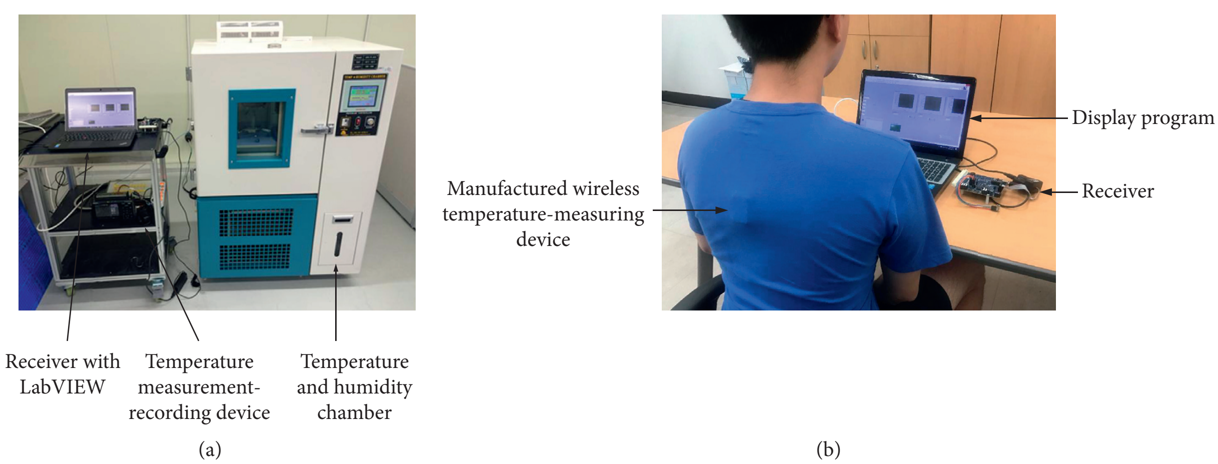

Figure 4: Photos of the manufactured system in the performance test: (a) temperature measurement performance test in the temperature and humidity chamber; (b) manufactured system in the *in vivo* experiment for measuring body temperature from the back of the body.

measured values from the proposed device. Therefore, a K-type thermocouple sensor was attached near the sensor hole of the manufactured wireless temperature-measuring device and connected with a midi logger GL820 (GRAPHTEC, USA) for observing temperature variation in the chamber. The data measured by the wireless temperature-measuring device were transmitted to a laptop connected to the receiver. The received temperature value was simultaneously processed and displayed with the developed LabVIEW program. In addition, a wireless communication performance test of the proposed device was conducted for observing the data rate, communication rate, and power consumption. A mixed-domain oscilloscope, MDO4104C (Tektronix, USA), was connected to the Master-In-Slave-Out (MISO) port of the MCU to monitor the wireless communication data rate. An experimental table had a receiver that connected to a laptop and could be moved far away from the wireless temperature-measuring device to find the maximum distance for wireless communication. Also, the power consumption was evaluated by a digital multimeter, Fluke 289 (Fluke, USA), connected to the power line of the wireless temperature-measuring device.

3.2.2. In Vivo Experiment. Ten subjects (gender: male, age: 25 ± 1 years old) were invited to participate in the *in vivo* experiment. Before the experiment began, the subjects were required to stay in the rest state with a comfortable posture to maintain a normal body temperature [13]. As Figure 4(b) shows, the manufactured wireless temperature-measuring device was attached on the middle of the back under the neck of the subject by Micropore Surgical Tape (3M, USA). Meanwhile, an infrared thermometer, Fluke VT04 (Fluke, USA) with a measurement range from −10°C to 250°C and accuracy of ±2°C at 25°C was used to measure the temperature of the surrounding skin for comparison with the value measured by the proposed device. Ear temperature is the most popular noninvasive approach to measure the core body temperature. Therefore, ear temperature was measured by an ear thermometer (Braun, Germany) for observing the relationship between ear temperature and skin temperature. The experiment was conducted for 10 minutes, and measurement data were recorded every 30 seconds. The temperature and humidity for the experimental environment were maintained at 25°C and 50%, respectively. A consumer indoor thermometer MOG-HTC1 (B. S. Basic, Korea), with temperature measurement range from −50°C~70°C, accuracy of 0.1°C, and the error value of ±1°C was used to monitor the environmental variation.

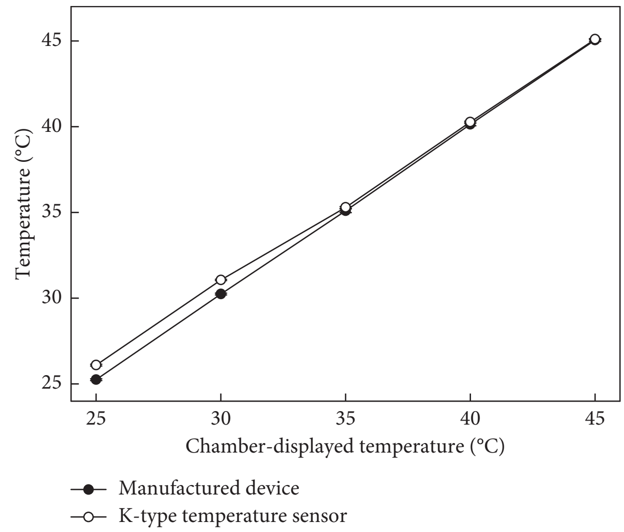

Figure 5: Comparison of the proposed manufactured wireless temperature-measuring device and a highly professional device in the temperature measurement performance test with a chamber temperature controlled from 25 to 45°C.

4. Results and Discussion

Experimental results for comparison of the manufactured wireless temperature-measuring device with the highly professional temperature-measuring device in the temperature-measurement performance test are shown in Figure 5. The temperature value measured by the proposed device was lower than the k-type sensor by 0.8°C at 25°C. The gap of the two measured values closed gradually with the increasing temperature in the chamber. At 35°C, the error value was only approximately 0.1°C. The measured temperature of the manufactured device was a little bit higher than the controlled temperature of the chamber, so it is assumed that the position of the designed sensor was close to the regulator elements of the power supply, and all the elements were packaged in the designed shell, which means the heat cannot be dissipated quickly.

Skin temperature measurement comparison results of the proposed wireless temperature-measuring device and IR thermometer for ten subjects in 10 minutes are shown in Figure 6(a). All of the subject results show that the temperature measured by the proposed device was lower than the IR thermometer by about 1°C for each subject. It was assumed that the IR thermometer has ±2°C error value and the position of the device is in front of the IR thermometer; therefore, the IR thermometer measured both the skin temperature and the proposed device's temperature. Also, as Figure 6(b) shows, the skin temperature was compared with the ear temperature measured by the proposed device and ear thermometer individually in the same condition for ten subjects. The ear temperatures for all of the subjects were close to 36.5°C, which means every subject had normothermia in these experiments. All of the experimental results show that the ear temperature was higher than the skin temperature by approximately 4°C. Other researchers such as Thomas et al., also reported these phenomena: such as a 9% variation between axillary skin temperature and rectal temperature and 16% variance between thoracic skin and rectal temperatures [14]. In this research, a 4°C error value between the back skin temperature and ear temperature means an approximately 11% variation, which is lower than the 16% variance found in comparing thoracic skin temperatures to rectal temperatures.

According to the *in vivo* experimental results, an algorithm based on the curve-fitting method for estimating the core body temperature by skin temperature was designed in this research. The algorithm was found with a linear model and set as a quadratic formula with an interpolant, as equation (1) shows. Each coefficient for the equation was set with 95% confidence bounds. For evaluating the goodness of fit, the sum of squares due to error (SSE), R-square, adjusted R-square, and root mean square error (RMSE) values were observed, and the values were 33.0874, 0.0212, 0.0117, and 0.3998, respectively. An example of using the developed algorithm to estimate the core body temperature by the measured skin temperature of one subject is shown in Figure 7. As mentioned before, ear temperature is larger than the skin temperature of about 4°C in the actual measurement. Through the developed algorithm, the measured skin temperature was converted to the estimated core body temperature that closely approximates the ear temperature. In addition, the algorithm can compensate the initial value occurring when the temperature sensor is in an initial status, so the measured value is lower than the actual value. All of the experimental results processed by the developed algorithm to compare the core body temperature are shown in Figure 8. As the results show, the mean value for the error between ear temperature and estimated core body temperature is about ±0.19°C and mean bias is 0.05 ± 0.14°C; this

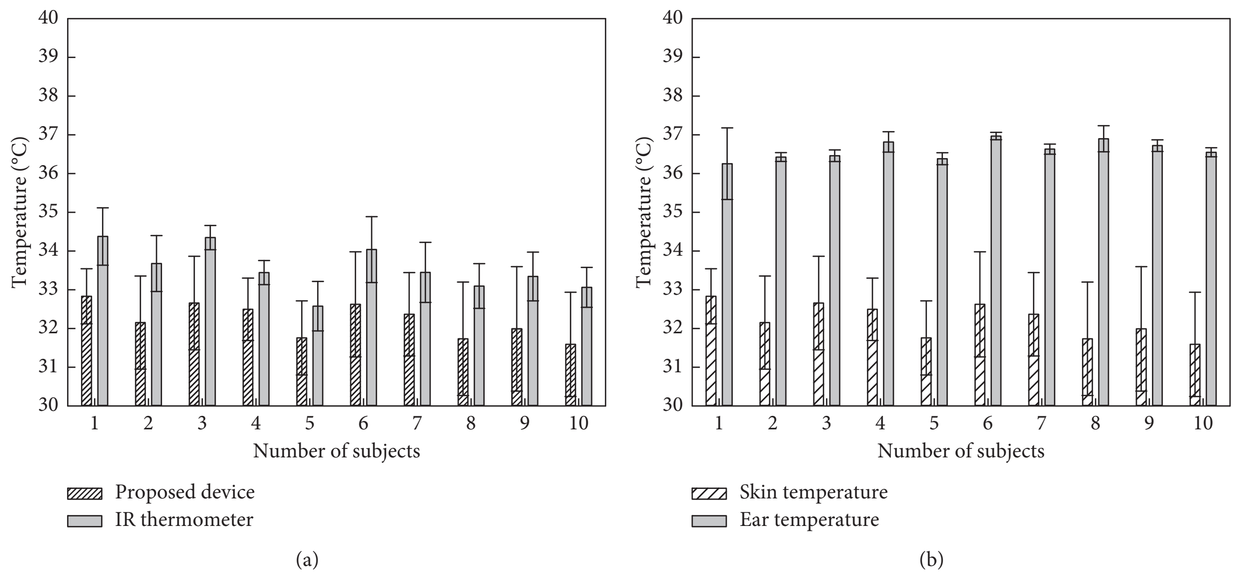

Figure 6: *In vivo* experimental results for observing the relationship between skin temperature and ear temperature: (a) skin temperatures were measured by the proposed device and IR thermometer for each subject; (b) comparison of the measured skin temperature and ear temperature.

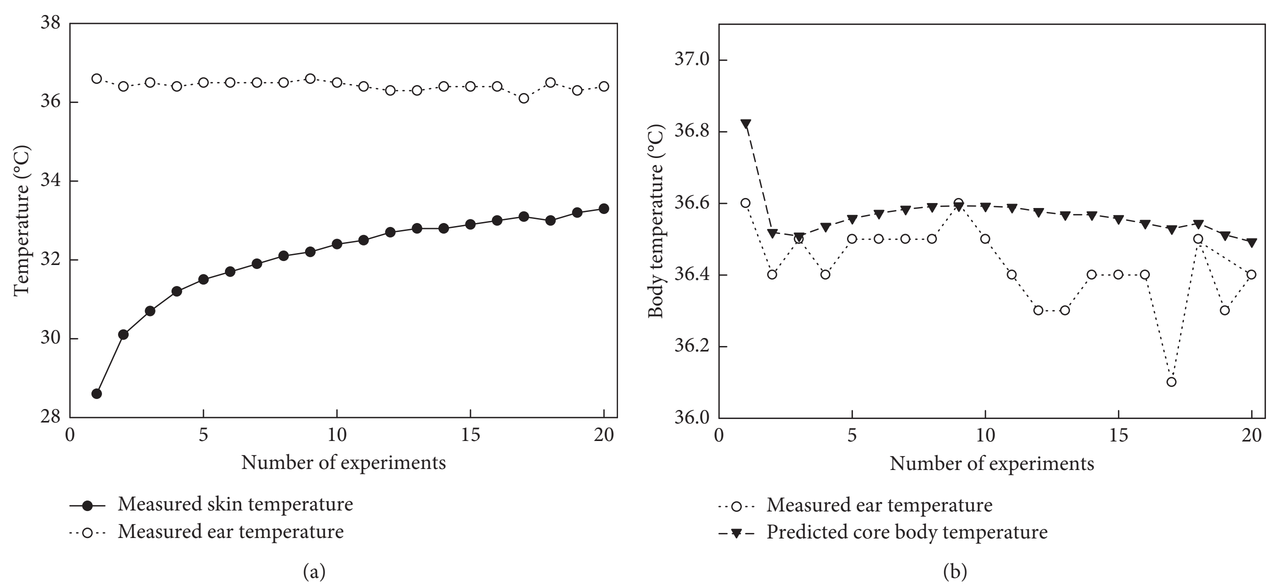

Figure 7: Using the developed algorithm to estimate core body temperature by skin temperature: (a) skin temperature vs. body temperature; (b) estimated body temperature vs. core body temperature.

can be explained by the accuracy of the developed algorithm, which is in the same range as the small core body temperature changes in the 10 subjects (maximum decrease of core body temperature of 0.4°C in subjects 6 and 8). However, in this paper, only the ear temperature was regarded as the reference value for the core body temperature, and the *in vivo* test was evaluated in a limited environment [16]. On the contrary, the wireless temperature-measuring device has shown a good performance when transmitting measuring data to the receiver in the operation performance test. The data transmission rate of the developed wireless communication method is about 600 kbps. And the power consumption of the wireless sensing device in operating was about 5.99 mA, and the proposed device can work without interruption about 40 hours:

$$\text{Core}_{\text{BodyTemp}} = 0.04615 \times \sin\left(\text{Skin}_{\text{Temp}} - pi\right) - 0.0006727 \times \left(\text{Skin}_{\text{Temp}} - 10\right)^2 + 36.97. \quad (1)$$

5. Conclusion

In this research, a wireless health monitoring system for measuring skin temperature from the back of the body to estimate the core body temperature was developed. The

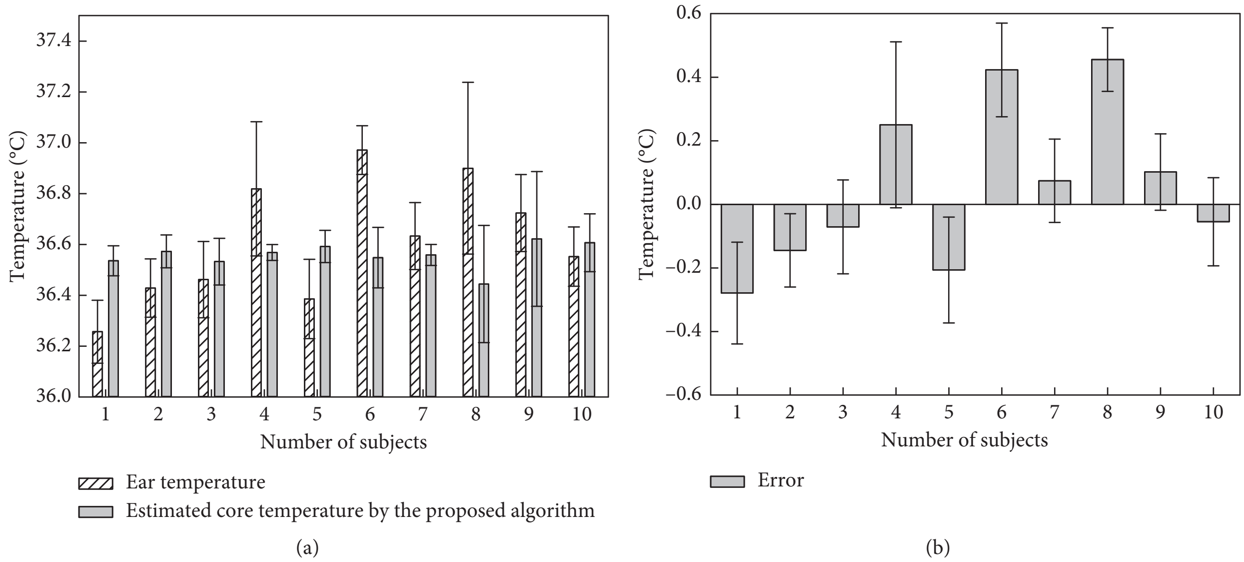

Figure 8: Comparison of the core body temperature and body temperature estimates for all subjects: (a) body temperature vs. estimated temperature; (b) error value between body temperature and estimated temperature.

system was manufactured with a highly accurate temperature sensor, low-power consumption MCU, and multi-channel ISM band RF method. According to the performance test results, the device performed well in measuring temperatures in a temperature chamber. Also, power consumption of the device during operation was approximately 5.99 mA, and the proposed device can work without interruption for approximately 40 hours. Therefore, the proposed device can be securely attached to the back of the body in order to measure skin temperature accurately for a long time. Experiment with 10 subjects in the rest status showed the measured skin temperature is lower than the ear temperature. Through the developed algorithm, this gap was compensated for, and the core body temperature that was estimated by the skin temperature approximated the ear temperature closely. However, in this paper, only the ear temperature was regarded as the reference value for the core temperature, and the *in vivo* test was evaluated in limited environment. In future work, the esophageal temperature will be considered as a gold standard for the core temperature, and some protocols such as exercise and bathing will be included for thermometer performance testing.

Data Availability

No additional unpublished data are available.

Conflicts of Interest

The authors declare that they have no conflicts of interest.

Acknowledgments

This research was supported by the Basic Science Research Program through the National Research Foundation of Korea (NRF) funded by the Ministry of Science, ICT & Future Planning (no. 2017R1C1B5017950).

References

[1] D. Karakitsos and A. Karabinis, "Hypothermia therapy after traumatic brain injury in children," *New England Journal of Medicine*, vol. 359, no. 11, pp. 1179-1180, 2008.

[2] G. S. Kelly, "Body temperature variability (Part 2): masking influences of body temperature variability and a review of body temperature variability in disease," *Alternative Medicine Review*, vol. 12, no. 1, pp. 49–62, 2007.

[3] M. Sund-Levander, C. Forsberg, and L. K. Wahren, "Normal oral, rectal, tympanic and axillary body temperature in adult men and women: a systematic literature review," *Scandinavian Journal of Caring Sciences*, vol. 16, no. 2, pp. 122–128, 2002.

[4] C. Morena, S. Brandissou, and M. Laruet, "Advantages and disadvantages of the different sites of body temperature taking," *Journal de Pharmacie Clinique*, vol. 17, no. 4, pp. 201–210, 1999.

[5] S. Asadian, A. Khatony, G. Moradi, A. Abdi, and M. Rezaei, "Accuracy and precision of four common peripheral temperature measurement methods in intensive care patients," *Medical Devices (Auckland, N.Z.)*, vol. 9, pp. 301–308, 2016.

[6] J. Rosell, J. Colominas, P. Riu, R. Pallas-Areny, and J. G. Webster, "Skin impedance from 1 Hz to 1 MHz," *IEEE Transactions on Biomedical Engineering*, vol. 35, no. 8, pp. 649–651, 1988.

[7] H. Benjamin, S. Bhansali, S. B. Hoath, W. L. Pickens, and R. Smallwood, "A planar micro-sensor for bio-impedance measurements," *Sensors and Actuators B: Chemical*, vol. 111-112, pp. 430–435, 2005.

[8] K. S. Wu, W. W. van Osdol, and R. H. Dauskardt, "Mechanical properties of human stratum corneum: effects of temperature, hydration, and chemical treatment," *Biomaterials*, vol. 27, no. 5, pp. 785–795, 2006.

[9] B.-W. Chang, C.-H. Chen, S.-J. Ding, D. C.-H. Chen, and H.-C. Chang, "Impedimetric monitoring of cell attachment on interdigitated microelectrodes," *Sensors and Actuators B: Chemical*, vol. 105, no. 2, pp. 159–163, 2005.

[10] R. Ivanic, I. Novotny, V. Rehacek, V. Tvarozek, and M. Weis, "Thin film non-symmetric microelectrode array for impedance monitoring of human skin," *Thin Solid Films*, vol. 433, no. 1-2, pp. 332–336, 2003.

[11] S. Y. Oh, L. Leung, D. Bommannan, R. H. Guy, and R. O. Potts, "Effect of current, ionic strength and temperature on the electrical properties of skin," *Journal of Controlled Release*, vol. 27, no. 2, pp. 115–125, 1993.

[12] N. A. S. Taylor, B. R. Wilsmore, D. Amos et al., "Indirect measurement of core temperature during work: clothing and environmental influences," in *Proceedings of 8th International Conference on Environmental Ergonomics*, vol. 8, pp. 325–328, San Diego, CA, USA, 1999.

[13] R. Niedermann, E. Wyss, S. Annaheim, A. Psikuta, S. Davey, and R. M. Rossi, "Prediction of human core body temperature using non-invasive measurement methods," *International Journal of Biometeorology*, vol. 58, no. 1, pp. 7–15, 2013.

[14] K. A. Thomas, R. Burr, S.-Y. Wang, M. J. Lentz, and J. Shaver, "Axillary and thoracic skin temperatures poorly comparable to core body temperature circadian rhythm: results from 2 adult populations," *Biological Research for Nursing*, vol. 5, no. 3, pp. 187–194, 2004.

[15] S. H. Woo, Z. M. U. Din, J. W. Lee et al., "Body temperature predicting patch-type telemedicine system," *IEICE Electronics Express*, vol. 6, no. 16, pp. 1161–1167, 2009.

[16] L. McCallum and D. Higgins, "Measuring body temperature," *Nursing Times*, vol. 108, no. 45, pp. 20–22, 2012.